Cranfield University

Nicholas Mark Davis

Mid-infrared spectroscopic instrumentation for airborne monitoring of atmospheric gas species

Centre for Engineering Photonics
School of Aerospace, Transport and Manufacturing

PhD Thesis

Academic Years:	2013 to 2018
Supervisors:	Dr. Jane Hodgkinson
	Prof. Ralph P Tatam
Submission:	February 2018

This thesis is submitted in partial fulfilment of the requirements for the degree of Doctor of Philosophy

Abstract

Methane is a colourless, odourless gas that can be found extensively in nature. The average global concentration of methane is currently approximately 1.8ppm, the highest concentration for over 800,000 years. Although this concentration is significantly lower than that of CO_2 (391ppm), methane has a global warming potential up to 34 times greater over a hundred year period. As a result, trace detection of atmospheric methane has gained increased attention as a form of environmental protection. The purpose of this thesis is to undertake investigations into the development of instrumentation to make observations of background levels of atmospheric methane. Newly available wavelength sources along with alternative gas cells are investigated for potential use in this instrument.

Laboratory analysis of a new external cavity Bragg-stabilised laser (ECBSL) operating at 1651nm was performed, with comparisons made against against a fibre-coupled distributed feedback (DFB) laser diode. The ECBSL showed promise for use in the detection of methane in the laboratory, with a limit of detection of 8ppm using a 25cm pathlength single-pass gas cell being comparable to that of the DFB laser diode. Issues with alignment stability were however observed with this laser, limiting the measurements that could be made and restricting its use outside of laboratory conditions, with utilisation on light aircraft deemed to be impossible in its current configuration.

Investigations were then performed into the performance of a newly available interband cascade laser (ICL), with emission at 3311nm. A full characterisation of the ICL was performed, alongside measurements of methane using both a 25cm pathlength single-pass cell and an integrating sphere with effective pathlength of 54.5cm, with single-point limits of detection of 2.2ppm and 1.0ppm being determined respectively. A combination of an Allan variance and absorption line-fitting techniques were utilised to improve the limit of detection using the integrating sphere, resulting in a 0.3ppm limit of detection for a 25 second average.

The design and development of instrumentation to perform measurements of background concentrations of atmospheric methane utilising the combination of ICL and integrating sphere is then described. The reasoning behind the selection of components and progression of the instrument design is described. Once assembled, laboratory testing of the instrument showed a single-point limit of detection of 1.6ppm, higher than that seen with the previous set-up, however this was still below the background methane concentration. An initial shakedown flight was carried out once the instrument had been certified and installed in the aircraft. Due to failures of two electrical components, further flight testing was postponed until improvements to component isolation have been made. This flight demonstrated, however, that the instrument has the potential to provide measurements of atmospheric methane, as the majority of components operated as expected, including both the laser and the cell optics.

Acknowledgements

I would first and foremost like to thank my supervisor Jane Hodgkinson, whose enthusiasm, support and advice throughout this project has been invaluable. She always found the time to provide any help or guidance when it was needed, especially during the more difficult periods of the PhD. Thank you as well to Ralph Tatam for providing the constructive feedback required to improve my work as much as possible.

I am especially grateful to Steve Staines for his continued help with my project build as well as deciphering my vague descriptions to design and produce items that were used in many of my experiments. I would also like to thank Dan Francis who was always available to offer advice and assistance throughout my project.

Thank you to all of the members of Engineering Photonics, both past and present, who have not only provided help and created an enjoyable working environment, but also some greatly needed distractions at times and lasting friendships.

Finally, and most importantly, I would like to thank my Mum, Dad, Brother Simon, and Grandma, along with the rest of my family, for their continued support, understanding and encouragement throughout the length of the PhD. I would especially like to thank my Mum and Dad, without whose constant support I would not have been able to get as far as I have.

"I may not have gone where I intended to go, but I think I have ended up where I needed to be."

— Douglas Adams

Table of contents

List of Figures

xi

List of Tables

List of Acronyms

ADC   Analogue to digital converter.

AU   Absorbance units.

CAD   Computer aided design.

CRDS   Cavity ring-down spectroscopy.

DAC   Digital to analogue converter.

DFB   Distributed feedback.

ECBSL   External cavity Bragg-stabilised laser.

ECDL   External cavity diode laser.

EOPL   Effective optical pathlength.

FMS   Frequency modulation spectroscopy.

HCW   Hollow core waveguide.

ICL   Interband cascade laser.

ICOS   Integrated cavity output spectroscopy.

LOD   Limit of detection.

NDIR   Non-dispersive infrared.

NEA   Noise equivalent absorbance.

NEBW   Noise equivalent bandwidth.

OSA   Optical spectrum analyser.

PAS   Photo-acoustic spectroscopy.

PLA   Polylactic acid.

PLC   Planar lightwave circuit.

QCL   Quantum cascade laser.

SCC   Standard cubic centimetre.

STFMS   Single-tone frequency modulation spectroscopy.

TDLS   Tunable diode laser spectroscopy.

TTFMS   Two-tone frequency modulation spectroscopy.

VCSEL   Vertical cavity surface-emitting laser.

WMS   Wavelength modulation spectroscopy.

List of Symbols

$\mathbf{a}$	Initial guess for parameter vector
A_{cell}	Absorption measurement for an arbitrary gas cell
A_{sphere}	Absorption measurement for an integrating sphere
α	Absorption coefficient
b_c	Pressure broadening coefficient
β	Temperature lapse rate (6.5K/km)
c	Speed of light in a vacuum (3×10^8 ms^{-1})
δ	Iterative step value
ΔI	Intensity of absorbed light
$\Delta\nu_L$	Lorentzian absorption line width
Δv	Free spectral range
f	Port fraction
$\mathbf{f}$	Vector of iterations of a model curve
$f(x_i, \mathbf{a})$	Model curve
g_0	Acceleration due to gravity (9.81 ms^{-2})
h	Altitude
I_0	Light incident on a gas cell
I	Transmitted light through a gas cell
$\mathbf{J}$	Jacobian matrix
$\mathbf{J}^T$	Transposed Jacobian matrix
ℓ	Optical pathlength
L	Fabry-Perot etalon length
L_{cell}	Pathlength of a gas cell

ℓ_{eff}	Effective optical pathlength
$L(\nu)$	Lorentzian absorption line shape
L_{ave}	Single-pass average pathlength
L_{sphere}	Integrating sphere pathlength
λ	Wavelength
λ_d	Non-negative damping factor
M	Reflection multiplier
m	Molar mass (28.96 g mol^{-1})
n	Refractive index
N_S	Number of averaged signals
ν	Wavenumber
ν_0	Absorption line centre wavenumber
$\nu_{\frac{1}{2}}$	Half-width of an absorption line
ν_m	Modulation frequency
P_0	Atmospheric pressure at sea level (1013.25 mBar)
P	Atmospheric pressure
p	Gas pressure
π	Pi (≈ 3.14)
R	Universal gas constant (8.31 J mol^{-1} K^{-1})
ρ	Reflectivity
S	Absorption line strength
σ_0	Pressure broadened absorption cross section
σ_A	Allan deviation
σ_A^2	Allan variance
$\sigma(\nu)$	Absorption cross section
T_0	Temperature at sea level (288.15K)
T	Time interval between measurements in an Allan variance
τ	Integration time for an Allan variance
τ_B	Data point time period
τ_R	Detector rise time

Chapter 1

Introduction

This chapter provides background information for the research undertaken, with an outline of the aims and objectives of the project displayed. Finally a description of the structure of the Thesis is provided.

1.1   Background

Average global concentrations of greenhouse gases increased at a rate of 2.2% per year between 2000 and 2010 [1], with current concentrations of CO_2, CH_4 and N_2O exceeding any level for the past 800,000 years, the period of measurement covered by ice cores [2].

The second of these gases, methane, is a colourless, odourless gas that can be found extensively in nature, being the most abundant organic trace gas in the atmosphere [3]. Although the concentration for methane is significantly lower than that of carbon dioxide (1.8ppm compared with 391ppm in 2011 [2]) it has a global warming potential up to 34 times greater than that of CO_2 over a hundred year period and much more (86 times greater) over its lifetime in the atmosphere of 20 years [4].

As a result, trace gas detection has attracted significant attention as a form of environmental protection, with methane detection systems gaining increased focus amongst these techniques.

1.1.1   Airborne atmospheric sensing

With the atmospheric concentration of methane at such a high level, the need for systematic measurements of its concentration, at both a global and local scale, is crucial. Measurements taken aboard an airborne platform or laboratory therefore offer an enticing method in the monitoring of atmospheric methane [5]. As a result of this demand for airborne measurements, numerous studies have already been undertaken, with the aim of exploring possibilities for aircraft atmospheric monitoring [5–13].

Light aircraft offer a number of advantages over alternative airborne platforms, including increased manoeuvrability and lower flight speeds. This allows the aircraft to more accurately target a specific location, such as a methane emission plume, and to remain within this location for a longer time period. This in turn allows any measurement instrumentation on the aircraft to take more accurate and a greater number of measurements compared with larger aircraft. As the instrumentation can be moved closer to any emission sources, demands on the specification of the instrument (such as the required limit of detection) can be relaxed.

Airborne platforms, including light aircraft, are however considered to be relatively harsh environments, presenting a number of performance issues when taking measurements that would otherwise not be present in laboratory conditions. Airborne instruments must not only have high sensitivity and selectivity, but also have a fast response time and be insensitive to vibrations caused by the aircraft or turbulence.

The weight, size and power requirements of any instrument operating in these environments must also be taken into account when the instrument is being designed. For example, to make sure their instrumentation was insensitive to in-flight vibration (as well as the shock from take-off and landing) on Douglas DC 3 and Lockheed L-188 aircraft, Schiff *et al.* (1990) [8] had to reduce the weight and power requirements of their instrument by approximately 140kg and 2kW respectively in comparison with the ground-based instrument.

The instrument must also be resistant to any changes in the ambient conditions within the aircraft, such as temperature, pressure and humidity. The standard temperature lapse rate with respect to altitude is 6.5K/km. This means that solely within the atmospheric boundary layer of Earth (between 2-3km above sea level [14]) the temperature could vary by as much as 19.5K. The ambient atmospheric pressure is also affected. Equation 1.1 shows the non-isothermal version of the barometric formula, which states how pressure changes with altitude within the troposphere (between sea level and an altitude of approximately 11km)[15]:

$$P(h) = P_0 \left(1 - \frac{\beta h}{T_0} \right)^{\frac{mg_0}{R\beta}} \tag{1.1}$$

where P is the pressure at a given altitude h, P_0 is defined as the pressure at sea level (1013.25 mBar), β is the temperature lapse rate, T_0 is the mean temperature at sea level (288.15 K), m is the molar mass of standard air (28.96 g mol^{-1}), g_0 is the acceleration due to gravity (9.81 ms^{-2}) and R is the universal gas constant (8.31 J mol^{-1} K^{-1}).

Figure 1.1 shows how the atmospheric pressure changes with altitude, following the barometric formula laid out in Equation 1.1. The central line shows the mean pressure at a given altitude, with the shaded blue region showing variation caused by changes in temperature and in the pressure at sea level. The graph shows that at an altitude of 11km, the pressure drops to approximately 230mBar, but only drops to around 700mBar at the top of the atmospheric boundary layer. The altitude that measurements are made at therefore will have a direct impact on what pressure regime the analysis will need to take place in. This will be covered further in Chapter 3.
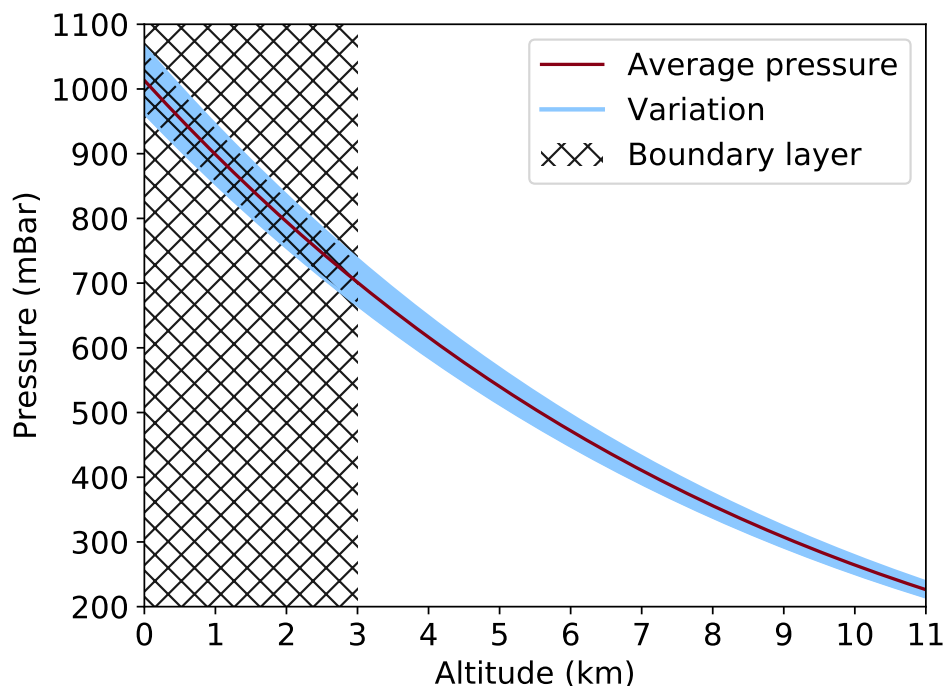
Figure 1.1: *Pressure change with altitude up to 11km, calculated from Equation 1.1. Changes in the mean caused by variations in temperature ($\pm 10^{\circ} C$) and pressure ($\pm 50mBar$) at sea level are highlighted.*

Richter *et al.* (2009) [13] have shown that the difference between laboratory equipment and airborne instruments over shorter averaging times (approximately 30 seconds) is negligible. This is due to the short-term measurements more likely being limited by white noise, therefore making the variance inversely proportional to the averaging time. After the optimum averaging time of the devices have been reached, however, some drift effects can be observed as a rise in variance as the averaging time increases. It was shown that the limit of detection (LOD) between an instrument optimised in the laboratory and an airborne instrument in flight can differ by up to a factor of 5 [13] for averaging periods of approximately 5 minutes.

1.2 Project aims & objectives

The aim of this PhD was to develop instrumentation utilising newly available wavelength sources and alternative gas cells, such as integrating spheres, that could make detections of background levels of atmospheric methane. The project was a collaboration between Cranfield University and the Facility for Airborne Atmospheric

Measurements (FAAM). The instrument was to be mounted on a lightweight aerial platform (light aircraft, unmanned aerial vehicle (UAV), etc.) so that in-flight measurements could be made.

The specific objectives of this project were as follows:

• Perform laboratory analysis into newly available wavelength sources and their ability to detect methane;

• Investigate the suitability of integrating spheres for use as optical gas cells in atmospheric measurements of methane;

• Develop instrumentation to perform in-flight measurements of methane at the background atmospheric concentration of 2ppm. This includes meeting flight certification requirements;

• Characterise the performance of the instrumentation developed at known concentrations in the laboratory;

• Perform in-flight testing of the instrumentation.

1.3   Thesis structure and content

Chapter 2 discusses the most commonly used gas detection techniques, both optical and non-optical, describing the advantages and limitations of each. An overview of the gas cells more frequently utilised in spectroscopic gas detection is provided.

Chapter 3 discusses the principles and theory behind tunable diode laser spectroscopy along with an analysis of the line fitting algorithms that are implemented in later chapters. A discussion of how the gas absorption lines behave under different atmospheric conditions and to what extent this will have an effect on the measurements taken is also provided. The theory behind integrating spheres is covered along with the advantages and disadvantages that they provide.

Chapter 4 describes the work undertaken making methane detections in the near infrared with a new external cavity Bragg grating-stabilised laser and making

comparisons with a conventional diode laser at the same wavelength.

Chapter 5 outlines work performed in the mid-infrared. A characterisation of an interband cascade laser is described alongside a full analysis of the noise in the laboratory set-up. Experimental results of the methane detection performed using both a single-pass gas cell and an integrating sphere are shown along with an analysis of the limit of detection and line fitting techniques.

Chapter 6 covers the development of the instrument built for airborne measurements of atmospheric methane. The evolution of the design is discussed along with the selection of the internal components. Analysis of laboratory and field testing of the instrument is then described.

Chapter 7 summarises the project, providing the conclusions that were drawn throughout and reviews the extent to which the objectives were met. The limitations of the current system are described and suggestions for future work are detailed.

Appendix A contains the datasheets for the interband cascade laser used in Chapters 5 and 6. Appendix B showcases the Labview data acquisition code utilised in the same chapters. Appendix C shows the designs of the 3D printed mounts used in the construction of the instrument, while Appendix D presents the aeroplane modification and certification documents.

References

[1] IPCC (2014), "Summary for Policymakers," in: Edenhofer, O., Pichs-Madruga, R., Sokona, Y., Farahani, E., Kadner, S., Seyboth, K., Adler, A., Baum, I., Brunner, S., Eickemeier, P., Kriemann, B., Savolainen, J., Schlömer, S., von Stechow, C., Zwickel, T. and Minx, J. (editors), "Climate Change 2014: Mitigation of Climate Change. Contribution of Working Group III to the Fifth Assessment Report of the Intergovernmental Panel on Climate Change," Cambridge University Press, Cambridge, United Kingdom and New York, NY, USA, pp. 1–33.

[2] IPCC (2013), "Summary for Policymakers," in: Stocker, T., Qin, D., Plattner, G.-K., Tignor, M., Allen, S., Boschung, J., Nauels, A., Xia, Y., Bex, V. and Midgley, P. (editors), "Climate Change 2013: The Physical Science Basis. Contribution of Working Group I to the Fifth Assessment Report of the Intergovernmental Panel on Climate Change," Cambridge University Press, Cambridge, United Kingdom and New York, NY, USA.

[3] Wuebbles, D. and Hayhoe, K. (2002), "Atmospheric methane and global change," *Earth-Science Reviews*, vol. 57, no. 3-4, pp. 177–210.

[4] Myhre, G., Shindell, D., Bréon, F.-M., Collins, W., Fuglestvedt, J., Huang, J., Koch, D., Lamarque, J.-F., Lee, D., Mendoza, B., Nakajima, T., Robock, A., Stephens, G., Takemura, T. and Zhang, H. (2013), "Anthropogenic and Natural Radiative Forcing," in: Stocker, T., Qin, D., Plattner, G.-K., Tignor, M., Allen, S., Boschung, J., Nauels, A., Xia, Y., Bex, V. and Midgley, P. (editors), "Climate Change 2013: The Physical Science Basis. Contribution of Working Group I to the Fifth Assessment Report of the Intergovernmental Panel on Climate Change," Cambridge University Press, Cambridge, United Kingdom and New York, NY, USA.

[5] Nadezhdinsky, A. I., Ponurovsky, Y. Y., Shapovalov, Y. P., Popov, I. P., Stavrovsky, D. B., Khattatov, V. U., Galaktionov, V. V. and Kuzmichev,

A. S. (2012), "Preliminary results of an aircraft system based on near-IR diode lasers for continuous measurements of the concentration of methane, carbon dioxide, water and its isotopes," *Applied Physics B*, vol. 109, no. 3, pp. 505–510.

[6] Webster, C. and May, R. (1987), "Simultaneous in situ measurements and diurnal variations of NO, NO_2, O_3, jNO_2, CH_4, H_2O, and CO_2 in the 40 to 26km region using an open path tunable diode laser spectrometer," *Journal of Geophysical Research*, vol. 92, no. D10, pp. 11931–11950.

[7] Adams, K. M., Davis, L. I., Japar, S. M. and Pierson, W. R. (1989), "Real-time, in situ measurements of atmospheric optical absorption in the visible via photoacoustic spectroscopy -II. Validation for atmospheric elemental carbon aerosol," *Atmospheric Environment*, vol. 23, no. 3, pp. 693–700.

[8] Schiff, H. I., Karecki, D. R., Harris, G. W., Hastie, D. R. and Mackay, G. I. (1990), "A tunable diode laser system for aircraft measurements of trace gases," *Journal of Geophysical Research: Atmospheres*, vol. 95, no. D7, pp. 10147–10153.

[9] Webster, C. R., May, R. D., Trimble, C. A., Chave, R. G. and Kendall, J. (1994), "Aircraft (ER-2) laser infrared absorption spectrometer (ALIAS) for in-situ stratospheric measurements of HCl, N_2O, CH_4, NO_2, and HNO_3," *Applied Optics*, vol. 33, no. 3, pp. 454–472.

[10] Fried, A., Wert, B. P., Henry, B. E. and Drummond, J. R. (1998), "Airborne tunable diode laser measurements of trace atmospheric gases," in: "Proceedings of SPIE," vol. 3285, pp. 154–162.

[11] Scott, D. C., Herman, R. L., Webster, C. R., May, R. D., Flesch, G. J. and Moyer, E. J. (1999), "Airborne laser infrared absorption spectrometer (ALIAS-II) for in situ atmospheric measurements of N_2O, CH_4, CO, HCl, and NO_2 from balloon or remotely piloted aircraft platforms," *Applied Optics*, vol. 38, no. 21, pp. 4609–4622.

[12] Rieker, G. B., Jeffries, J. B. and Hanson, R. K. (2009), "Calibration-free wavelength-modulation spectroscopy for measurements of gas temperature and concentration in harsh environments," *Applied Optics*, vol. 48, no. 29, pp. 5546–5560.

[13] Richter, D., Fried, A. and Weibring, P. (2009), "Difference frequency generation laser based spectrometers," *Laser and Photonics Review*, vol. 3, no. 4, pp. 343–354.

[14] Garratt, J. R. (1994), "Review : the atmospheric boundary layer," *Earth Science Reviews*, vol. 37, pp. 89–134.

[15] Berberan-Santos, M. N., Bodunov, E. N. and Pogliani, L. (1997), "On the barometric formula," *American Journal of Physics*, vol. 65, no. 5, pp. 404–412.

Chapter 2

Methane Detection Techniques

This chapter describes the more common optical, and non-optical, techniques used for the detection of methane.

2.1 Non optical techniques

There are a number of non-optical techniques that could be used to detect methane. The techniques that are discussed here are electrochemical sensors, flame ionisation detectors, catalytic sensors, and metal oxide semiconductors.

2.1.1 Electrochemical sensors

Electrochemical sensors are made up of a number of electrodes: working (sensing), counter and reference. These are enclosed in a sensor housing that is in contact with a liquid electrolyte [1], as shown in Figure 2.1. The working electrode is on the inner face of a membrane that is porous to gas but impermeable to the electrolyte. When the target gas reaches the working electrode, either oxidation or reduction occurs (depending on the gas species). The current produced by this reaction can then be measured, with amplitude being proportional to the concentration of the gas.

These sensors are compact, have low power consumption, have good linearity and repeatability, and have a low limit of detection (LOD) (between 0.02 and 50 ppm). However, their average lifetime can be relatively low, typically one to three years [2]. The sensors can also have long response times, ranging from a few seconds to a few minutes in some cases [3]. The detection of methane using these sensors is still in

the development stage, with a prototype device being produced in 2015 that was
shown to detect 100ppm methane [4].
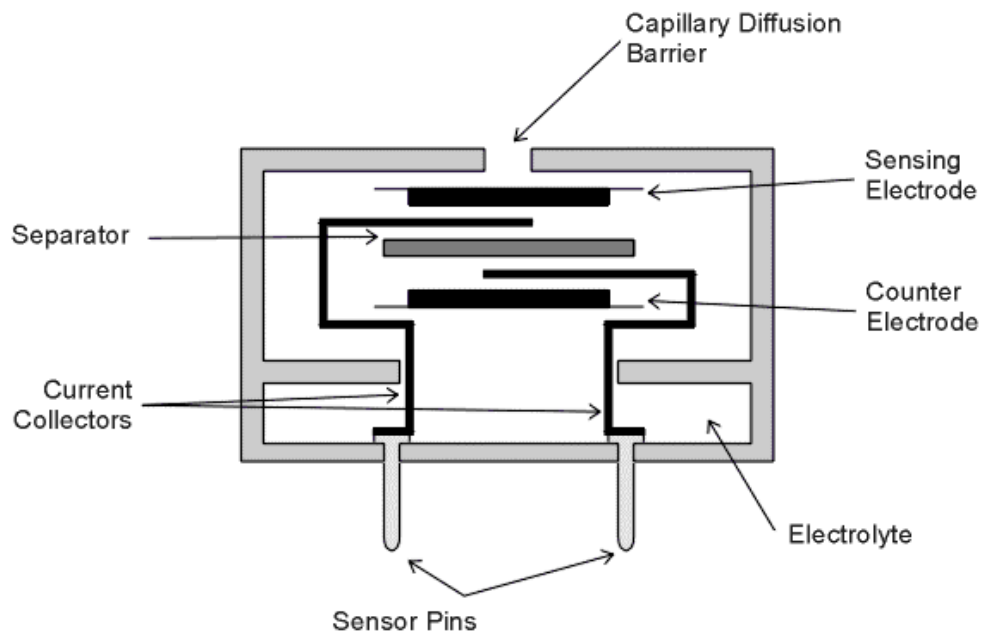
Figure 2.1: *An example of the internal structure of a typical electrochemical sensor,*
taken from [5].

The use of these sensors within this project can therefore be deemed to be impractical,
as significantly lower detection limits are needed for methane detection and a shorter
response time is crucial.

2.1.2   Flame ionisation detectors

Originally demonstrated in 1958 by McWilliam and Dewer [6], flame ionisation
detectors (FIDs) measure the changes in the number of ions generated in a hydrogen
flame caused by the presence of trace quantities of organic compounds. A schematic
diagram of a typical fast response FID is shown in Figure 2.2. The sample gas is
burned in the hydrogen flame, with the organic compounds reduced into carbon
fragments and become ionised. These ions are then collected above the flame on a
high voltage biased electrode.

FIDs are effective detectors of organic molecules, having been shown to detect
concentrations below 1ppm with little influence from inorganic molecules [7]. Unfortunately,

this technique is non-selective between the different organic compounds that interact with the sensor. Strict flight regulations on fuel sources on-board aircraft also limit the potential for this technique to be utilised in this project due to the need to carry a small hydrogen cylinder on-board.
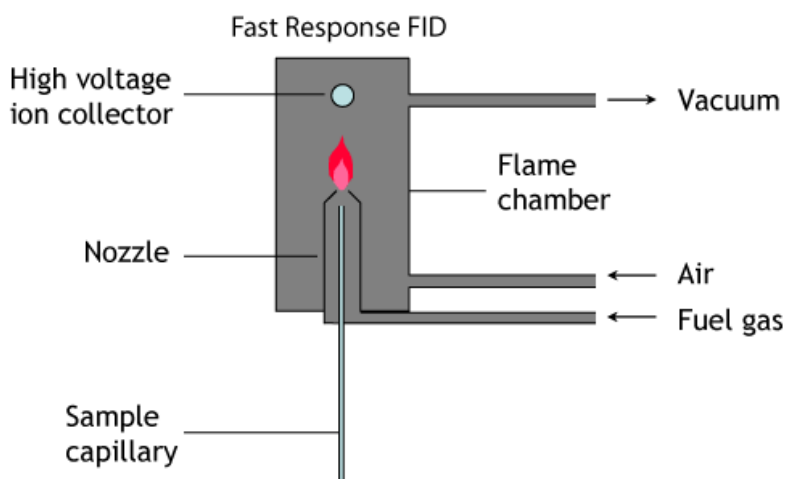
Figure 2.2: *Schematic diagram of a fast response flame ionisation detector, taken from [8].*

2.1.3   Catalytic sensors

Catalytic Sensors usually consist of a pellistor element: an electrically heated platinum coil of wire covered with a catalytic substance, such as palladium [9]. A schematic of a typical catalytic bead sensor is shown in Figure 2.3. When a combustible gas (such as methane) passes over the hot catalyst surface, the gas is ignited, raising the temperature of the pellistor element and as a result altering the resistance of the platinum coil. This resistance change is directly proportional to the target gas concentration. These sensors are a simple, low cost, proven technology with a long lifetime. They are, however, not very sensitive, typically having a LOD of approximately 500ppm, suffer from long response times (20-30 seconds), are non-selective between combustible gases, and can be poisoned or their calibration affected by their exposure to different gases.
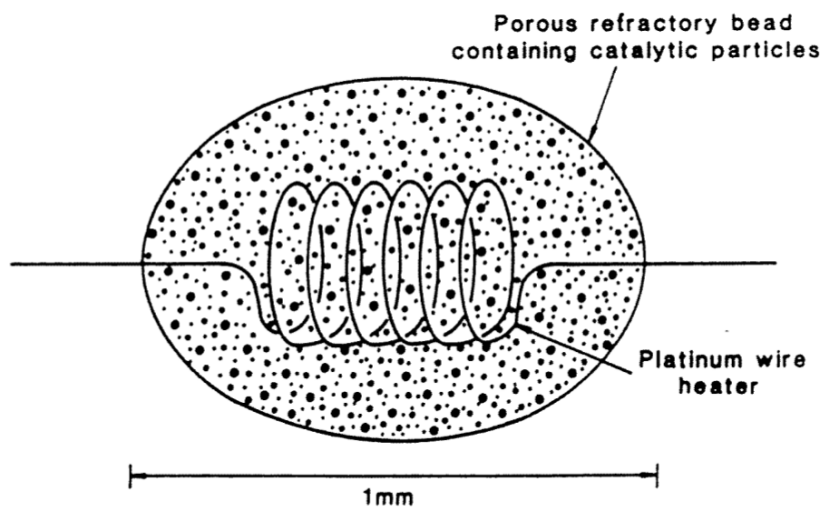
Figure 2.3: *Example schematic of catalytic bead sensor, taken from [9].*

2.1.4 Metal oxide semiconductors

Metal oxide semiconductors operate in a similar manner to catalytic sensors. These sensors consist of a thin metal-oxide film deposited on top of a substrate, as shown in Figure 2.4. When the target gas comes into contact with the surface of the device, a change in the electrical resistance of the oxide material can be observed, with the amplitude of the change directly corresponding to the concentration of the gas being analysed [9].
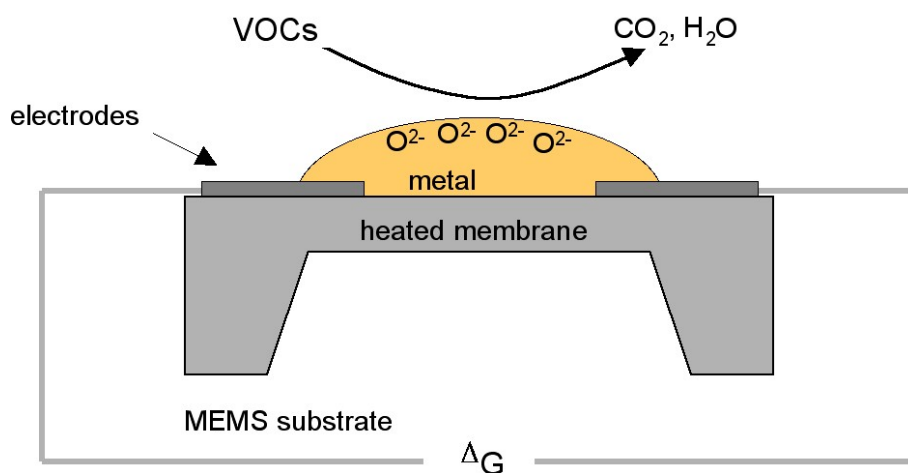
Figure 2.4: *Example schematic of a metal oxide semiconductor gas sensor, taken from [10].*

These sensors are simple, robust, and can be sensitive down to the ppm level for methane. They have been found, however, to be unreliable when used in

13

atmospheric environments as they can be affected by fluctuations in temperature and humidity, producing a drift in the measurements. This therefore makes them an unsuitable option for use within this project, where the main aim is to take accurate measurements in an atmospheric environment.

2.1.5   Summary of non-optical techniques

Table 2.1 displays a comparison of the different available non-optical techniques that can be used to detect methane. As mentioned in the previous sections, each of these techniques has properties that would make them desirable for the airborne measurements in this project (low limits of detection, compact, low cost, etc.). However, each of them also has at least one aspect that would make them impractical for use, e.g. long response times, non-selectivity, sensitivity to fluctuations in ambient conditions. As such, these techniques are not feasible for use in this project. The following sections describe optical methods of detection that provide a more logical footing for airborne usage.

2.2   Optical absorption spectroscopy

Optical absorption spectroscopy is an ideal and often used method of trace gas detection, having fast response times, high specificity and low LOD [11]. These methods measure how different gas species absorb light with respect to their concentrations [12]. The basic principle of optical absorption spectroscopy can be described using the Beer-Lambert law [12]:

$$I = I_0 \exp(-\alpha \ell) \tag{2.1}$$

where I is the light transmitted through the gas cell, I_0 is the light incident on the gas cell, α is the absorption coefficient of the target gas species (typically with units cm^{-1}) and ℓ is the cell's optical pathlength (typically with units cm).

Table 2.1: *Comparison of non-optical gas detection techniques.*

Detection Technique	Principle	Advantages	Disadvantages
Electrochemical sensors	Consist of three electrodes, amplitude of reaction current corresponds to concentration	• Compact • Low power consumption • Good linearity and repeatability	• Short Lifespan • Long response times • High LOD for methane (100ppm)
Flame ionisation detectors	Measure changes in ion count from hydrogen flame caused by organic compounds	• Highly sensitive (<1ppm LOD) • Not influenced by non-organic compounds	• Non-selective between organic compounds • Fuel source required
Catalytic sensors	Measure change in resistance in pellistor when gas interacts with catalyst	• Simple to implement • Low cost • Long lifespan	• High LOD (500ppm) • Long response times (20-30 seconds)
Metal-oxide semiconductors	Measure change in resistance in metal-oxide substrate when in contact with gas	• Simple to implement • Robust • ppm sensitivity for methane	• Influenced by temperature and humidity in atmospheric conditions causing drift

For low $\alpha\ell$, equation 2.1 becomes linear and can be expressed as follows:

$$\frac{\Delta I}{I_0} \approx \alpha\ell \tag{2.2}$$

where $\Delta I = I_0 - I$ and $\Delta I/I_0$ is defined as the absorbance, which is unitless but often expressed in terms of absorbance units (AU). The limit of detection of a target gas species can be quantified as the noise equivalent absorbance (NEA, in units AU) or the minimum detectable absorption coefficient (α_{min} in cm^{-1}), allowing instrumental techniques to be compared without reference to the specific target gas.

For many gas species, the fundamental bands of vibrational transition absorption bands lie in the mid infrared, whilst the overtone and combination bands usually lie within the near infrared. In the case of methane, the strongest vibrational absorbance

bands are in the 3.3μm and 7.7μm regions, with weaker absorption bands being found at 1.65μm and 2.3μm.

A comparison of the absorption bands for methane in the near and mid infrared is shown in Figure 2.5. A commonly targeted absorption line for the analysis of methane is at 1651nm, due to the ease of acquiring light sources and detectors that operate in this wavelength region. Although this line is the strongest in its respective absorption band, it has an absorption coefficient approximately 100 times smaller than those seen at 3.3μm.
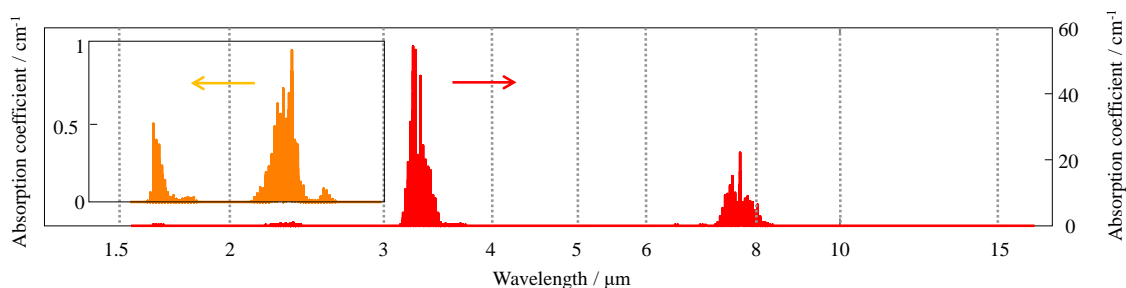
Figure 2.5: *Comparison of methane absorption line strength in the near (inset) and mid infrared,, taken from [13].*

2.3   Non dispersive infrared (NDIR)

NDIR is a specific category of broadband, non-dispersive gas sensing undertaken in the mid-infrared spectral region. These sensors operate by directing the emission of a broadband light source through two filters, one covering the absorption band of the target gas species, the other covering a neighbouring non-absorbed region [11]. An example of an NDIR gas sensor can be seen in the diagram shown in Figure 2.6.

NDIR sensors are simple to implement, compact, lightweight and have a relatively low cost. They do, however, have a number of drawbacks. These include drift in the light source and detector, low spectral sensitivity meaning that other gas species can influence the signal, and that dust or dirt on one of the filters can be interpreted as gas absorption. Sensors are currently commercially available with LODs of <500ppm
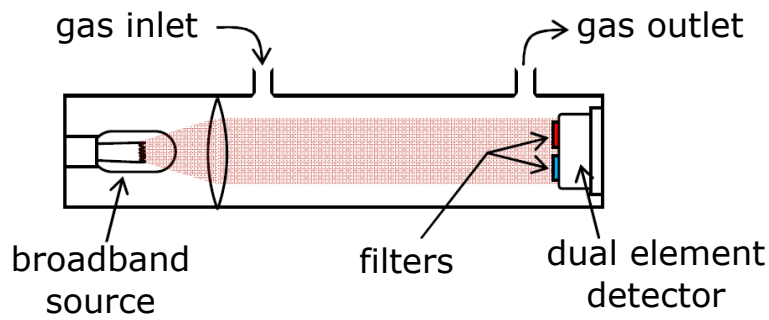
Figure 2.6: *Schematic diagram of a typical NDIR gas sensor, taken from [11].*

for methane that are small and have low power requirements [14]. Although this LOD is lower than other techniques, it would not be suitable for this project where LODs of <2ppm are needed.

2.4 Photo-acoustic spectroscopy (PAS)

PAS is based on a light absorption effect that was first investigated in 1880 by Alexander Graham Bell [15]. When a gas in a closed cell is irradiated with a beam of light at a wavelength that is absorbed by the gas, the absorbed light causes periodic heating of the gas, in turn producing pressure fluctuations within the chamber [16]. If the light is then chopped or modulated at a frequency (typically within the acoustic frequency range (20Hz-20kHz)), the pressure fluctuations can be detected using a sensitive microphone.
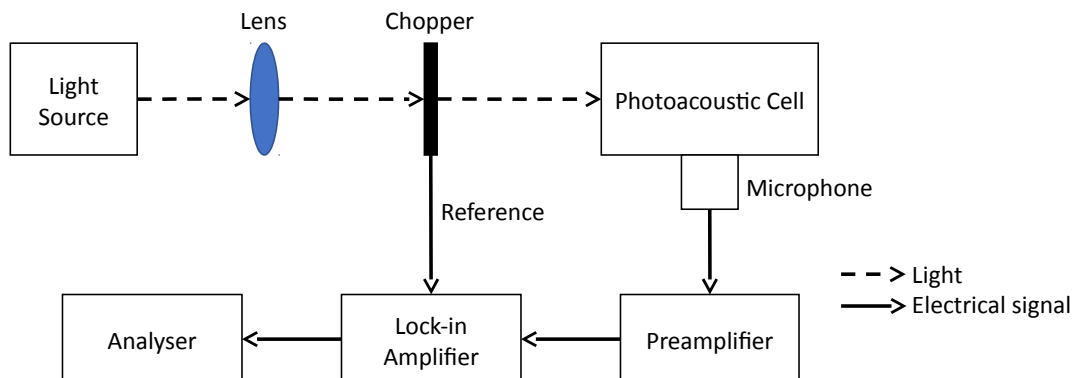
Figure 2.7: *Block diagram of a typical photoacoustic spectroscopic system.*

Figure 2.7 shows a block diagram of the typical set-up used in PAS. In this system, the light source (for example a CO_2 laser [17]) is focused onto a photoacoustic cell through a chopper wheel. An ideal photoacoustic cell will amplify, or resonate with, the generated sound by the molecular absorption whilst also isolating acoustic noise.

There are a number of potential advantages to using this system:

(i) Low LODs can be achieved using this technique, with <1ppm for methane reported by Wolff *et al* in 2013 [18].

(ii) The detected signal is directly proportional to the intensity of the light that is absorbed, ΔI, as opposed to the transmitted light, I. The effects of shot noise, flicker noise and relative intensity noise (associated with the light source) are greatly reduced.

(iii) Scattered light has less of an effect on the photoacoustic signal than it does in conventional spectrophotometry where the effective value of I_0 would be reduced, giving a false absorption measurement.

(iv) The dynamic range of the technique can be large.

(v) No photodetector is required for the main signal, improving performance in the mid-infrared where standard uncooled detectors can have poor detectivity.

There are also, however, a number of disadvantages to using this technique, especially outside of laboratory conditions. The first drawback with this technique is that if the background matrix changes, a subsequent change can be observed in the signal level, produced by changes in the relaxation processes and pathways. PAS is also highly sensitive to background acoustic noise and vibrations. With large vibration and noise signals being present on the aircraft planned for use in this project, PAS therefore becomes an unviable option, even when considering the list of advantages it holds over other spectroscopic techniques.

2.5　Tunable diode laser spectroscopy (TDLS)

TDLS is a technique whereby the concentration of a specific gas species is measured through the use of tunable lasers and laser absorption spectroscopy. In TDLS, the emission wavelength of a laser diode is scanned across one or more gas absorption lines at a high resolution [11]. The use of tunable diode lasers as a potential approach to measure atmospheric pollutants was first investigated by Hinkley and Kelley in 1971 [19].

2.5.1　Direct spectroscopy

Direct Spectroscopy is the most fundamental form of TDLS. The output of a laser diode is modulated so that the emission line is scanned across one or more gas absorption lines in a narrow wavelength range [20]. This is achieved through continuously modulating the injection current of the laser diode with either a sawtooth or triangular waveform produced by a function generator. This action causes the wavelength of the laser diode to be modulated over a specific range. This modulated beam is then directed through a gas cell containing the sample under investigation, before being detected and amplified for analysis. A line diagram of the typical set-up used in direct spectroscopy can be seen in Figure 2.8.
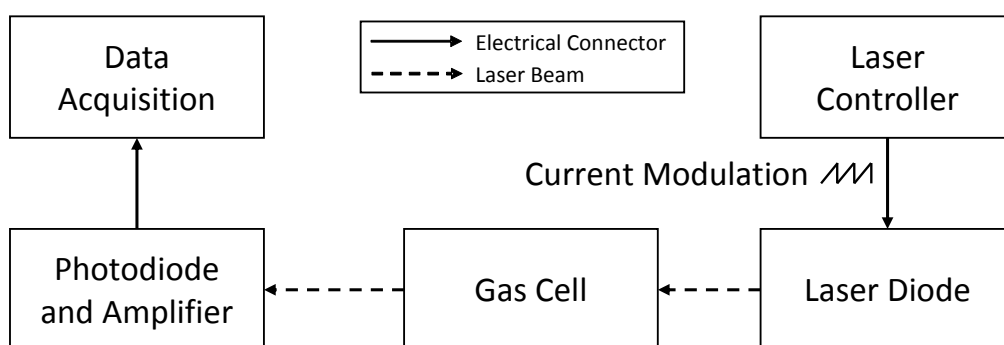
Figure 2.8: *Line diagram of a typical set-up utilised in direct spectroscopy.*

The resultant transmission obtained using this method gives an increasing background (the output intensity of the laser) as it rises with the increase in injection current. A dip in the point corresponding to the wavelength of the gas absorption line is

then observed in this rising background. Figure 2.9 shows an example of a methane absorption line detected using direct spectroscopy compared with the signal obtained when no methane is present in the gas cell. By subtracting a zero reference and taking the ratio of the detected signal to the laser light intensity, a normalised version of the gas absorption line can be produced.
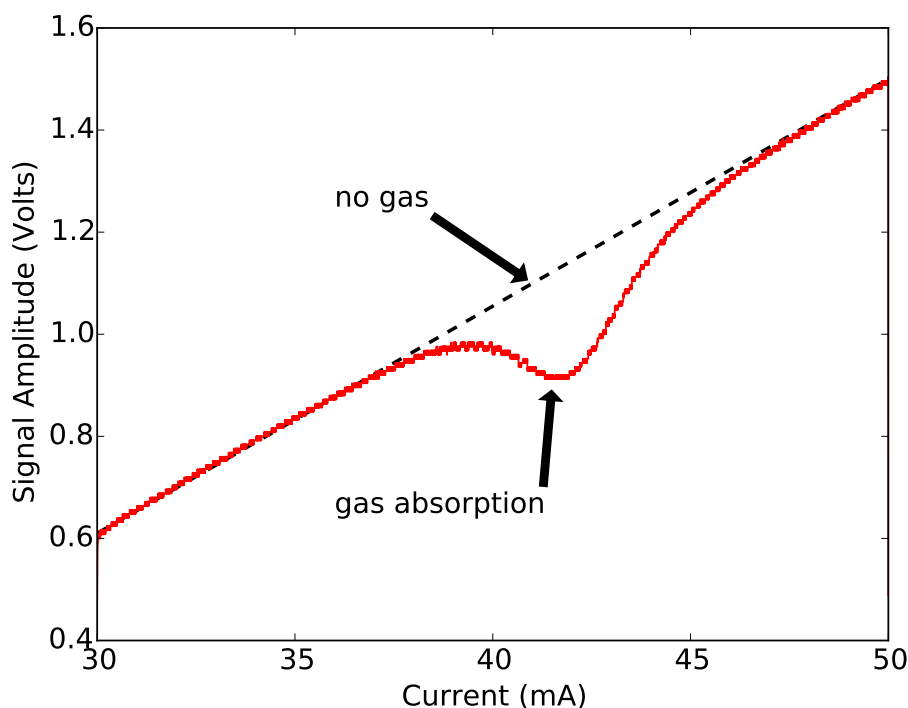
Figure 2.9: *Example of a methane absorption line found using direct spectroscopy compared with the signal obtained when no methane is present. Taken by author using procedure described in section 2.5.1.*

Direct spectroscopy holds a number of advantages over other forms of TDLS. The experimental set-up needed to utilise this technique is simple to implement and maintain. Calibration of this technique is also simpler than other TDLS variations due to it being self-referenced. An absolute value for the absorption observed is provided through this technique, whereas other forms of TDLS only give a relative absorption value. There are, however, disadvantages to direct spectroscopy. The technique has lower sensitivity than others and any fluctuations in the incident light can have an effect on the measured signal.

2.5.2   Wavelength modulation spectroscopy

Wavelength modulation spectroscopy (WMS) is similar to direct spectroscopy, in that the injection current of the diode laser is modulated. In addition to the sawtooth waveform used in direct spectroscopy, WMS induces a higher frequency sinusoidal waveform onto the ramp, generating an additional high-frequency modulation in the emitted laser intensity and wavelength [21]. WMS was first investigated in 1974 by Tang *et al* [22], where they demonstrated the usefulness of a "wavelength-modulated cw dye laser for derivative spectroscopy of solids".

This additional waveform, at the modulation frequency ν_m, is applied at a significantly lower frequency than that of the half-width of the absorption line under investigation, $\nu_{\frac{1}{2}}$. This modulation is typically in the kilohertz to megahertz range and as a result, WMS can be characterised so that $\nu_m/\nu_{\frac{1}{2}} \ll 1$ [23]. With the laser wavelength simultaneously being gradually scanned across the absorption line, the resulting signal can then be demodulated by a phase sensitive detector (such as a lock-in amplifier) at the modulation frequency or harmonics thereof.

(a) *1st harmonic*   **(b)** *2nd harmonic*   **(c)** *3rd harmonic*
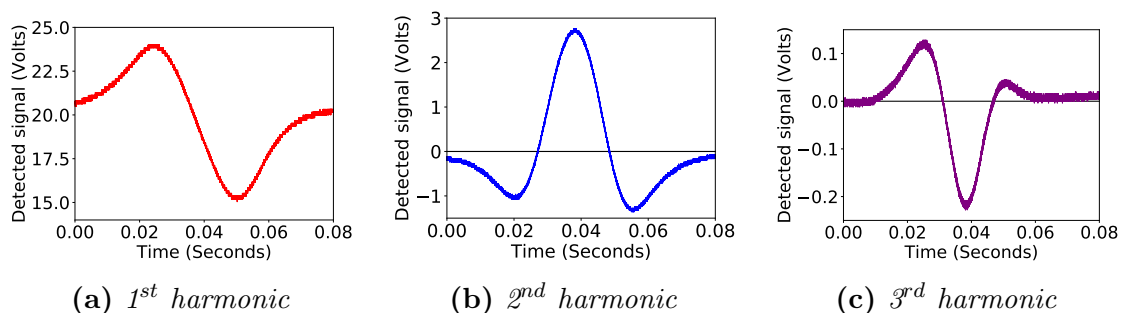
Figure 2.10: *Harmonics of the modulation frequency when detecting a gas absorption line, taken by author.*

The first three harmonics, examples of which can be seen in Figure 2.10, are the more common harmonics used for detection, as most lock-in amplifiers have settings that enable them to pick up these lower harmonics. One of the main reasons that lower modulation frequencies and harmonics are used is to be able to make use of the simple and cheap detection circuits that are readily available in the audio

frequency range (approximately 20Hz to 20kHz). Most WMS applications use the second harmonic (Figure 2.10b) for taking measurements of gas concentrations as there are relatively low noise levels, the signal peaks at the absorption line centre, and the baselines are usually flat [24]. The first and third harmonics, Figures 2.10a and 2.10c respectively, are usually used for subsequent signal processing, either for normalisation [25] or frequency stabilisation [26].

Detection at the second harmonic produces a significantly smaller DC offset than that seen in the first harmonic due to the increase in intensity in the direct absorption signal. This increase produces a significant DC offset in the first derivative, with the magnitude of this offset being proportional to the laser power incident on the detector [20]. This results in the first derivative still being susceptible to any fluctuations in the laser power. Use of the second harmonic further reduces the effect of these laser power fluctuations, however its magnitude is still proportional to the incident laser power.

Standard WMS techniques require regular recalibration of the equipment to be able to acquire reliable and accurate measurements. So-called "calibration-free" WMS has been developed [27], however this requires the use of additional equipment.

2.5.3 Frequency modulation spectroscopy

Frequency modulation spectroscopy (FMS) can be seen as an extension of the WMS technique. FMS extends the modulation used in WMS to significantly higher frequencies, between 100MHz and 10GHz [28]. As a result, FMS operates with a modulation frequency greater than the optical linewidth of the probed absorption feature. At these higher frequencies, the noise developed by the laser source is negligible, meaning that the sensitivity of detection may be limited only through the quantum noise of the detector [29].

FMS was first investigated by Bjorklund in 1980 [30]. A tunable dye laser was modulated by the signal from an external phase modulator driven at radio frequencies.

Using this, measurements of Fabry-Perot resonances, I_2 vapour absorption lines, and saturation holes in Na vapour were produced, with absorptions down to $5\text{x}10^{-5}$ AU detected.

Measurements performed by Werle *et al* in 1989 [31] concluded that the 1/f laser noise decreased by up to 40dB between 2 and 200MHz, showing that noise levels can be substantially reduced by using high frequency modulation techniques. It was also found that the sensitivity of systems modulated at 200MHz improved, with the signal to noise ratio increasing by 2 orders of magnitude compared with modulations below 1MHz.

There are several methods used in the implementation of FMS using diode lasers. The two most common methods are single-tone frequency modulation spectroscopy (STFMS) and two-tone frequency modulation spectroscopy (TTFMS). Each of these techniques are described in more detail in the following sections.

2.5.4   Single-tone frequency modulation spectroscopy

In STFMS, the output of a laser is modulated using a high frequency RF generator operating in the GHz regime, resulting in one or more side-bands separated by the modulation frequency [29, 32]. When the detector photocurrent is combined with a local oscillator at the modulation frequency, with the laser being scanned across the absorption line, the resulting spectrum will contain both positive and negative peaks. The shape of these peaks are proportional to the original absorption line shape.

STFMS is, in essence, a differential absorption technique, therefore in order to produce optimum sensitivity, the modulation frequency must be larger than the width of the probed absorption feature so that only one sideband is absorbed at a time [32]. Investigating broad spectral features also requires that the modulation frequencies must be respectively high. Detectors with bandwidths this high, however, are complex to utilise.

The use of STFMS with multipass cells is also limited due to the attenuation of the laser power on the detector [28]. The signal to noise ratio reaches a maximum at a lower number of passes compared with WMS. The sensitivity of the technique is also limited by water vapour in the optical path, reducing the effectiveness of this method for atmospheric measurements due to relatively high levels of water vapour in the atmosphere (1-2%abs.)[33].

2.5.5 Two-tone frequency modulation spectroscopy

TTFMS was first demonstrated by Janik *et al* in 1986 [34]. TTFMS is similar to STFMS, however it operates with an additional modulation frequency, closely spaced to the first in frequency, with the beat tone between the two monitored as the absorption line is scanned. The processing of the signal then occurs at the beat frequency.

The main advantage of this technique over STFMS is that the detector bandwidth only needs to be in the 1-10MHz range rather than >150MHz, even if the system requires a modulation in the GHz range [29]. As a result, this reduces the need for large bandwidth detectors, meaning that relatively inexpensive detectors may be used instead. The signal originating from TTFMS absorption comes from the variation between the absorption of the laser frequency and the sum of the sideband absorptions, with the signal peaking at the absorption line centre with even symmetry.

Table 2.2: *Comparison of most common TDLS techniques.*

Detection Technique	Principle	Advantages	Disadvantages	Typical Performance	References
Direct Spectroscopy	Laser frequency scanned across absorption line	• Simple to implement • Provides absolute value for absorption • Smaller/less equipment required	• Low sensitivity • Fluctuations in incident light can affect measured signal	4.3 ppm LOD (20cm pathlength)	[11, 35]
Wavelength Modulation Spectroscopy	Modulation at several kHz; detection occurs at harmonics, usually 2f	• High sensitivity • Simple circuitry for modulation and detection	• Extra equipment is needed • Calibration required • Only gives relative absorption	2.0 ppm LOD (10cm pathlength)	[20, 21, 25, 26, 36]
Single-Tone Frequency Modulation Spectroscopy	RF modulation signal, detection occurs at RF frequencies	• Negligible 1/f noise • Increased detection sensitivity	• Complex electronics needed for modulation and detection • Unsuitable for use in atmospheric conditions	$\approx$ppb LOD	[28, 29, 32]
Two-Tone Frequency Modulation Spectroscopy	Modulation at two RF frequencies with detection at beat frequency	• Negligible 1/f noise • Increased detection sensitivity • Reduced detection bandwidth	• Complex electronics needed for modulation	0.4 ppb $Hz^{-1/2}$ LOD (13m pathlength)	[29, 34, 37]

2.5.6   Summary of TDLS detection techniques

A summary of the different TDLS techniques commonly used can be seen in Table 2.2. This comparison shows that WMS, STFMS and TTFMS each have a higher sensitivity than that seen with direct spectroscopy, making them more desirable techniques to use in a laboratory. However, due to the nature of this project where atmospheric measurements are to be taken in less than ideal conditions, these methods become less viable due to the additional size and weight criteria of the equipment required for operation, as well as the added complexity of needing to calibrate the equipment before measurements can be taken.

As such, the technique that will be utilised for this project is direct spectroscopy. This will allow absolute values for absorption to be measured through the use of relatively simple, lightweight equipment and electronics.

2.6   Overview of available gas absorption cells

For all of the optical absorption methods mentioned previously, a gas cell is utilised to perform analysis of the target gas species. There are a number of different varieties of cell that exist. A brief overview of commonly used cells will be covered in this section.

2.6.1   Single-pass cell

The most basic form of gas cell is the single-pass cell, as shown in Figure 2.11. In this cell light passes directly through a tube of arbitrary length with windows at each end, often aligned at the Brewster angle. This is the angle at which light at a particular polarisation state may pass perfectly through the window with no reflection[38]. This is done to prevent interference fringes from developing in the cell. Gas inlets and outlets are often positioned at opposing ends of the tube to encourage mixing along the entire length of the cell. Although these cells are simple to manufacture and utilise, they are extremely susceptible to misalignment, with even small vibrations causing a reduction in the detected signal. To increase the optical pathlength, a

new cell would have to be manufactured at the specified length, with much longer pathlength cells becoming unwieldy and much more difficult to align. To combat this, multipass cells are often utilised, with the more commonly used varieties described in the following sections.
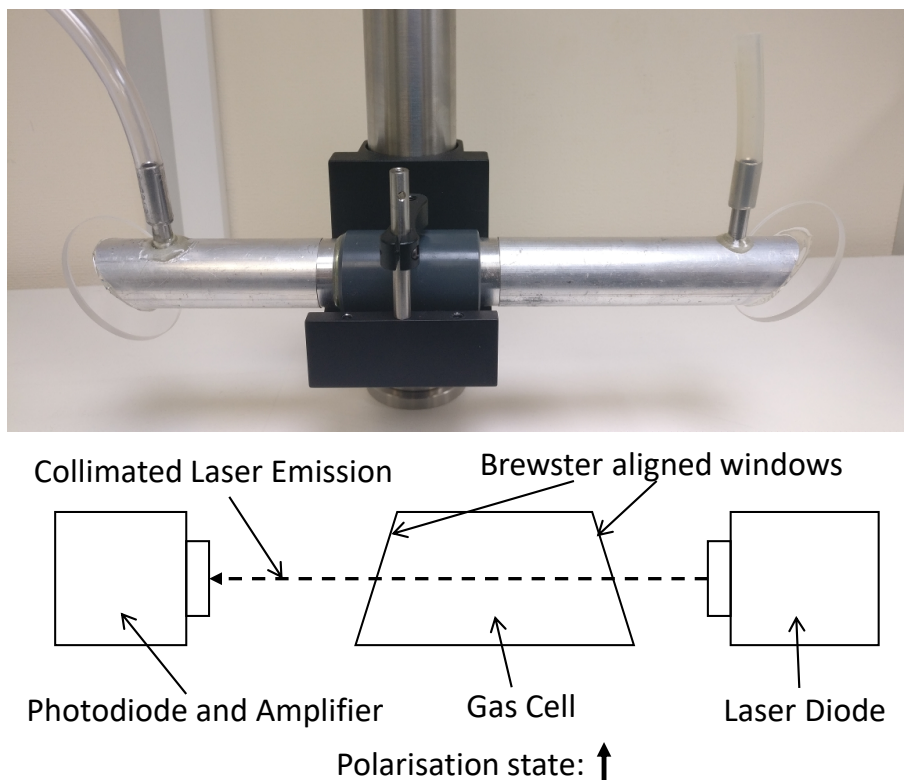
Figure 2.11: *Example of a single-pass gas absorption cell with Brewster aligned windows, as used for this project in Chapter 5, with a line diagram to show typical usage.*

2.6.2   White cell

The first commonly used example of a multipass cell is the White cell, developed by John U. White in 1942 [39]. The cell, which utilises three spherical concave mirrors with the same radius of curvature, can be seen in a schematic diagram in Figure 2.12. Light from a source is reflected between two closely spaced mirrors at one end, A and A', and a third mirror opposite them, B. The centres of curvature of A and A' are on the front surface of B, with B's centre of curvature halfway between A and A'. By adjusting the separation distance between A and A' symmetrically around B and its centre of curvature, the number of traversals can be adjusted. As a result of

the orientation and curvature of the mirrors, the total number of traversals must always occur in multiples of four.
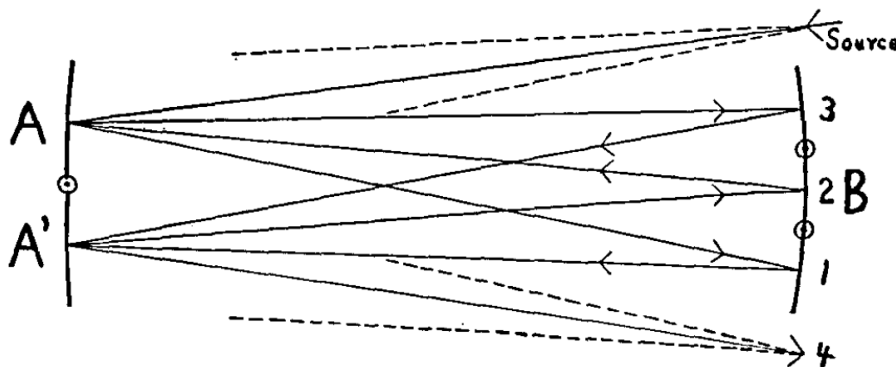
Figure 2.12: *Schematic diagram of the original White cell, taken from [39].*

White cells are still commonly used in absorption spectroscopy for a number of reasons: the number of traversals is easily controlled and consequently so is the optical pathlength, beams of high numerical aperture can be used, and they are relatively stable. Pathlengths of several thousand metres can be achieved with this cell, with Ferguson *et al* achieving a pathlength of 5984m [40]. However, they do require precise alignment of the source and detector, meaning that even small vibrations can cause a misalignment of the system and have an effect on the optical path.

2.6.3   Herriott cell

Herriott cells, as developed by D. R. Herriott and H. J. Schulte in 1965 [41], operate using a similar technique to the White cell, except two spherical mirrors are used instead of three. Light from a source is passed through a hole in one of the mirrors and reflected between the two, as shown in Figure 2.13. The beam can then either output back through the same hole or through a separate hole on the opposite mirror. As a result, the Herriott cell can be used with multiple light sources through the use of multiple input and output apertures.
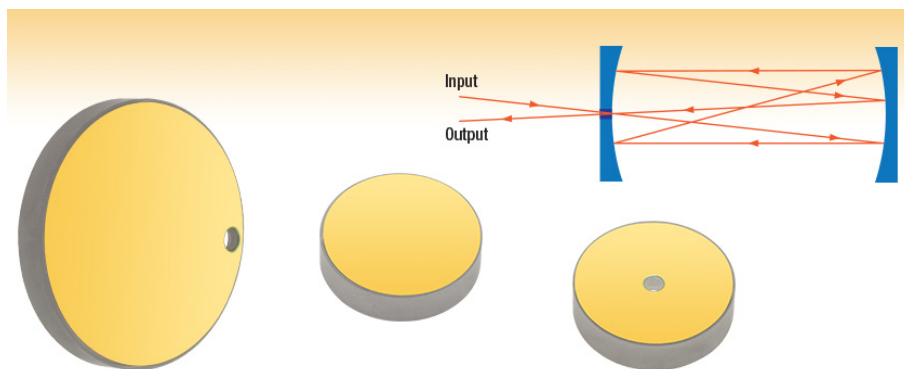
Figure 2.13: *Schematic diagram of a Herriott cell with examples of types of concave mirrors used, taken from [42].*

The optical pathlength of the cell is controlled by changing the separation of the mirrors, making this cell simpler to align and operate than the White cell. The cell is also less susceptible to mechanical disturbance or vibration than the White cell and can be more stable. Pathlengths of 10s of metres are typically achieved with these cells, with Li *et al* utilising a 100m cell in 2016 [43]. However, high numerical aperture beams cannot be utilised and in order to gain longer pathlengths, significantly larger mirrors must be used.

2.6.4 Integrating sphere

Integrating spheres (or cavities) consist of a hollow container with a diffusely reflective internal surface, an example of which can be seen in Figure 2.14a. These cells are more traditionally used for measuring the power output of an incident light source, however they have also been adapted for use as gas absorption cells, first being performed by Venkatesh *et al* in 1980 [44]. Typically, these cells possess two or more ports for light sources and detectors, with an additional two ports for gas inflow and exhaust. A light barrier (or baffle) is often positioned within the sphere to prevent direct illumination of the detector from the light source.
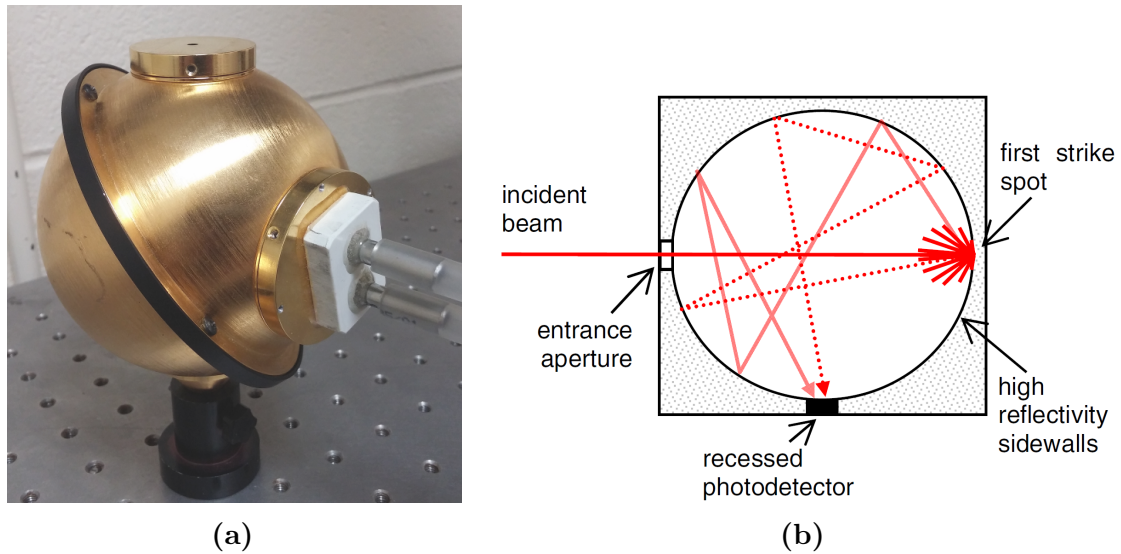
Figure 2.14: *(a) Example of an integrating sphere with gas inlet and outlet, as used by author in Chapter 5. (b) Simplified model of an integrating sphere, showing a collimated beam making a pass across the cell to the first strike spot before scattering (taken from [11]).*

Integrating spheres have been shown to be tolerant to misalignment [11], allowing them to be utilised in conditions where high vibration levels and g-loading are present, such as those found on light aircraft. In contrast with other gas cells, integrating spheres do not produce interference fringes, reducing the amount of optimisation needed in their set-up.

Pathlengths for these cells are typically of the order of a few metres, with Tranchart *et al* utilising a 4 inch diameter, Spectralon coated sphere with and effective pathlength of 4.4m [45]. The achievable pathlength of an integrating sphere, however, is heavily dependent on the reflectivity of the surface, with reflective coatings for the near infrared providing significantly longer pathlengths than those in the mid infrared. Fouling of the reflective surface can therefore also have a significant impact on pathlength, meaning that the surface reflectivity has to be monitored for any changes [46].

2.6.5   Hollow core waveguide

Hollow core waveguides (HCW) consist of a hollow tube with an inner diameter typically between 300μm and 1mm. The inner surface of the waveguide is coated with

a silver mirror finish followed by a silver halide to create an efficient infrared dielectric reflector. An acrylate buffer surrounds the silica tube to provide protection [47]. A schematic diagram of HCWs can be seen in Figure 2.15.
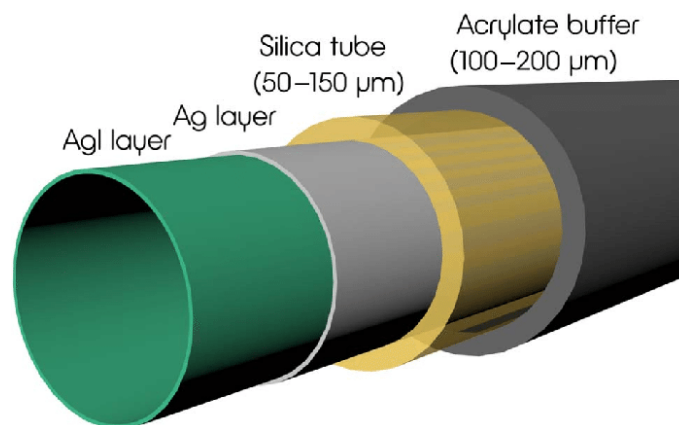
Figure 2.15: *Schematic diagram of a HCW, displaying the individual layers and coatings, taken from [48].*

Due to reflections within the core, the optical pathlength of the HCW needs to be calibrated before use. This is achived by performing a measurement at a known concentration and comparing it to a measurement of the same concentration made with a different cell of a known pathlength. A major advantage of HCWs is that their small size means that a large length of the waveguide can be positioned within a small volume. This is ideal when the size of the gas sample is restricted, or when a fast response is needed. This same small size, however, provides a disadvantage in terms of sensitivity to misalignment caused by vibration. This means that using it for airborne measurements is dependent on securing the waveguide so misalignment cannot occur.

2.6.6 Summary of commonly used gas cells

Table 2.3 summarises and compares the different commonly used gas cells. Although they have shorter optical pathlengths in the mid-infrared than the alternatives, the fact that integrating spheres show tolerance to misalignment and vibration makes them the most viable option for use in this project.

Table 2.3: *Comparison of commonly used gas cells.*

Gas Cell	Principle	Advantages	Disadvantages
Single-pass cell	A tube of arbitrary length with Brewster aligned windows	• Simple to use • Easy to produce	• Difficult to adjust pathlength • Susceptible to misalignment • Longer pathlengths unwieldy
White cell	Three spherical concave mirrors, two closely spaced opposite a third	• Easily controlled pathlength • Relatively stable	• Precise alignment required • Alignment can be influenced by vibration
Herriott cell	Two spherical mirrors, with hole(s) for input and output	• Can be used with multiple light sources • Easily controlled pathlength • Less susceptible to vibration	• High numerical aperture beams cannot be used • Significantly larger mirrors needed for longer pathlengths
Integrating sphere	Diffusely reflective chamber, with ports for input, detection, and gas flow	• Tolerant to misalignment • Insensitive to vibration • Do not produce interference fringes	• Shorter pathlengths in mid infrared • Sensitive to fouling of the reflective surface
Hollow core waveguide	Hollow tube (fibre) with internal surface coated with a mirror finish and silver halide	• Large length of waveguide can fit in small volume	• Sensitive to vibration • Waveguide needs to be secured to prevent misalignment

2.7　Current instrumentation for the detection of methane

As mentioned in Chapter 1, taking measurements of the background methane concentration in the atmosphere has gained increased focus in recent years. As a result, a number of different instruments have been developed to perform this task. This section therefore aims to provide an overview of the techniques that have been used in both laboratory and field based systems.

Several PAS based methane detection systems have been developed for use both in laboratory conditions and in the field [18, 49–51]. Most notably of these is the system developed by Jahjah *et al*, utilising PAS to perform measurements of both the background atmospheric methane concentration and of methane plumes with a sensitivity of 13ppb [50]. Although this system did provide a low LOD, additional infrastructure was required to isolate the system from external vibrations.

Numerous TDLS-based systems have been developed for laboratory measurements of methane [52–56]. Most systems utilising this technique employ the use of a standard multipass cell (such as a Herriott cell), with the long pathlengths these provide allowing for low LODs. For example, Yu *et al* have developed a sensor that employs a multipass gas cell with a pathlength of 57.6m to perform measurements of methane, providing an LOD of 2.2ppb (with an integration time of 129 seconds) [54]. Integrating spheres have also been employed in this technique, with Masiyano *et al* demonstrating an LOD of 0.4ppm using a 100mm sphere with a pathlength of 3.4m [52].

Similarly, a number of TDLS-based systems have been developed for ground and aircraft measurements of methane [57–63]. As with the laboratory TDLS systems, these instruments utilise multipass cells to allow longer pathlengths to be achieved. The ALIAS-II instrument developed by Scott *et al* employs the use of a Herriott cell with a pathlength of up to 120m, allowing a detection precision (limit of detection) for

methane of 10ppb to be achieved [62]. As with the PAS based field instrumentation, however, additional infrastructure is required on all of these devices to prevent any misalignment to occur.

A number of commercial systems are also available for atmospheric detection of trace gases, most notably the technologies developed by Picarro Inc., Aerodyne Research Inc., and Los Gatos Research. The products developed by Picarro utilise a technology known as cavity ring-down spectroscopy (CRDS) , whereby the incident light from the laser is directed into a high finesse optical cavity, usually constructed from two or more highly reflective mirrors (approximately 99.999%) [64]. A short pulse from the laser is sent into the cavity, with the decay rate of the light intensity measured by a photodetector. The rate at which the light intensity decays corresponds to the target gas concentration within the cavity. Using this technique, Picarro have developed sensors that can achieve optical pathlengths of up to 20km, with a precision of 2ppb for methane [65].

Aerodyne Research Ltd. have developed a number of trace gas monitors based on an astigmatic multipass absorption cell. These cells have been developed to be relatively lightweight (1.25kg) whilst providing up to a 76m optical pathlength [66]. When incorporated into their trace gas monitors, these cells can allow methane concentration measurements to occur with a precision of 0.1ppb (for a 60 second measurement).

Los Gatos Research have developed a number of gas analysers for the simultaneous detection of greenhouse gases. These systems allow for the measurement of methane with a precision of 0.3ppb (for a 100 second measurement) [67]. These devices utilise a technique known as integrated cavity output spectroscopy (ICOS) , based on CRDS, where the absorption signal is obtained through the integration of the total signal transmitted through the optical cavity, similar to conventional absorption measurements.

Each of these commercial systems has a potential drawback however. Due to the nature of CRDS, the instruments developed by Picarro and Los Gatos can require longer time periods in order to take a single measurement. The instrument developed by Aerodyne, although it can provide faster measurements, the multipass cells it employs can misalign if not secured correctly. All of them are still relatively large and heavy (up to 40kg).

2.8   Summary

In this chapter, a review of the non-optical and optical techniques commonly used in the detection of methane has been performed. A summary of the different non-optical techniques is provided in Table 2.1. TDLS has been shown to hold a number of advantages over the other optical techniques discussed in this chapter, including fast response times, high sensitivity and selectivity. A comparison of TDLS methods is covered in Table 2.2.

As discussed in section 2.5.6, this project has elected to implement direct spectroscopy. Although direct spectroscopy is less sensitive than WMS or FMS, it still offers relatively high sensitivity and selectivity compared with other optical techniques, whilst only using relatively simple and lightweight equipment and electronics. Due to direct spectroscopy being self-referenced, the calibration of this system is also simpler in comparison with other forms of TDLS.

A discussion of some of the more commonly used gas cells utilised in gas detection was performed in section 2.6 and summarised in Table 2.3. It was determined that, although the White and Herriott cells can provide significantly longer pathlengths than the alternatives (especially single-pass cells), their sensitivity to vibration and misalignment make them impractical for this project. Hollow core waveguides provide a long optical pathlength for a small gas volume, however they also suffer when vibration is present, needing to be secured to prevent misalignment.

Integrating spheres seem to provide the greatest compromise between pathlength and mechanical sensitivity. Although integrating spheres offer shorter pathlengths than those seen with the White and Herriott cells, they are tolerant to misalignment and mechanical vibration and do not produce interference. This makes them an ideal candidate for use in this project.

References

[1] Yoon, J.-Y. (2012), *Introduction to Biosensors: From Electric Circuits to Immunosensors*, Springer, New York.

[2] Delphian Corporation, "Electrochemical Sensors," http://www.delphian.com/ electrochemical%20sensors.htm, Date Accessed: 20/04/2018.

[3] Zosel, J., Oelßner, W., Decker, M., Gerlach, G. and Guth, U. (2011), "The measurement of dissolved and gaseous carbon dioxide concentration," *Measurement Science and Technology*, vol. 22, no. 7, p. 072001 (45 pages).

[4] Sekhar, P. K., Kysar, J., Brosha, E. L. and Kreller, C. R. (2016), "Development and testing of an electrochemical methane sensor," *Sensors and Actuators, B: Chemical*, vol. 228, pp. 162–167.

[5] SGX Sensortech, "Introduction to Electrochemical (EC) Gas Sensors," http://www.sgxsensortech.com/content/uploads/2014/08/ Introduction-to-Electrochemical-EC-Gas-Sensors1.pdf, Date Accessed: 09/02/2016.

[6] McWilliam, I. G. and Dewar, R. A. (1958), "Flame ionization detector for gas chromatography," *Nature*, vol. 181, no. 4611, p. 760.

[7] Calvert, J. G. (1990), "Glossary of atmospheric chemistry terms," *Pure and Applied Chemistry*, vol. 62, no. 11, pp. 2167–2219.

[8] Cambustion Limited, "Fast FID Principles," http://www.cambustion.com/ products/hfr500/fast-fid-principles, Date Accessed: 23/05/2017.

[9] Moseley, P. (1997), "Solid state gas sensors," *Measurement Science and Technology*, vol. 8, no. 3, pp. 223–237.

[10] BIOPRO Baden-Württemberg GmbH, "AppliedSensor GmbH Chemical gas sensors to detect contaminants,"

https://www.gesundheitsindustrie-bw.de/en/article/news/
appliedsensor-gmbh-chemical-gas-sensors-to-detect-contaminants/,   Date
Accessed: 19/07/2017.

[11] Hodgkinson, J. and Tatam, R. P. (2013), "Optical gas sensing: a review,"
Measurement Science and Technology, vol. 24, no. 1, p. 012004 (59 pages).

[12] Ingle, J. D. and Crouch, S. R. (1988), *Spectrochemical Analysis*, Prentice Hall
PTR, New Jersey, USA.

[13] Hodgkinson, J., "Methane detection using optical absorption," Presentation for
Council of Gas Detection and Environmental Monitoring, Oct. 2013.

[14] Alphasense, "NDIR sensors," http://www.alphasense.com/index.php/products/
ndir-air/, Date Accessed: 13/12/2017.

[15] Bell, A. G. (1880), "On the production and reproduction of sound by light,"
American Journal of Science, vol. 20, no. 3, pp. 305–324.

[16] Skoog, D. A., Holler, F. J. and Nieman, T. A. (1998), *Principles of Instrumental
Analysis*, Saunders Golden Sunburst Series, 5th ed., Saunders College Publishing.

[17] Loper, G. L., Calloway, A. R., Stamps, M. A. and Gelbwachs, J. A. (1980),
"Carbon dioxide laser absorption spectra and low ppb photoacoustic detection of
hydrazine fuels," *Applied Optics*, vol. 19, no. 16, pp. 2726–2734.

[18] Wolff, M., Rhein, S., Bruhns, H., Nähle, L., Fischer, M. and Koeth, J. (2013),
"Photoacoustic methane detection using a novel DFB-type diode laser at 3.3 μm,"
Sensors and Actuators B: Chemical, vol. 187, pp. 574–577.

[19] Hinkley, E. D. and Kelley, P. L. (1971), "Detection of Air Pollutants with
Tunable Diode Lasers," *Science*, vol. 171, no. 3972, pp. 635–639.

[20] Reid, J., Shewchun, J., Garside, B. K. and Ballik, E. A. (1978), "High sensitivity
pollution detection employing tunable diode lasers," *Applied Optics*, vol. 17,
no. 2, pp. 300–307.

[21] Rieker, G. B., Jeffries, J. B. and Hanson, R. K. (2009), "Calibration-free wavelength-modulation spectroscopy for measurements of gas temperature and concentration in harsh environments," *Applied Optics*, vol. 48, no. 29, pp. 5546–5560.

[22] Tang, C. L. and Telle, J. M. (1974), "Laser modulation spectroscopy of solids," *Journal of Applied Physics*, vol. 45, no. 10, pp. 4503–4505.

[23] Bomse, D. S., Stanton, A. C. and Silver, J. A. (1992), "Frequency modulation and wavelength modulation spectroscopies: comparison of experimental methods using a lead-salt diode laser," *Applied Optics*, vol. 31, no. 6, pp. 718–31.

[24] Masiyano, D., Hodgkinson, J. and Tatam, R. P. (2008), "Use of diffuse reflections in tunable diode laser absorption spectroscopy: Implications of laser speckle for gas absorption measurements," *Applied Physics B: Lasers and Optics*, vol. 90, no. 2, pp. 279–288.

[25] Schilt, S., Thevenaz, L. and Robert, P. (2003), "Wavelength modulation spectroscopy: combined frequency and intensity laser modulation," *Applied Optics*, vol. 42, no. 33, pp. 6728–6738.

[26] Iseki, T. (2004), "A portable remote methane detector using an InGaAsP DFB laser," *Environmental Geology*, vol. 46, no. 8, pp. 1064–1069.

[27] Upadhyay, A., Wilson, D., Lengden, M., Chakraborty, A. L., Stewart, G. and Johnstone, W. (2017), "Calibration-Free WMS Using a cw-DFB-QCL, a VCSEL, and an Edge-Emitting DFB Laser with In-Situ Real-Time Laser Parameter Characterization," *IEEE Photonics Journal*, vol. 9, no. 2, p. 6801217 (17 pages).

[28] Schiff, H. I., Mackay, G. I. and Bechara, J. (1994), "The Use of Tunable Diode Laser Absorption Spectroscopy for Atmospheric Measurements," in: Sigrist, M. W. (editor), "Air Monitoring by Spectroscopic Techniques," Wiley, New York, pp. 239–334.

[29] Silver, J. A. (1992), "Frequency-modulation spectroscopy for trace species detection: theory and comparison among experimental methods," *Applied Optics*, vol. 31, no. 6, pp. 707–717.

[30] Bjorklund, G. C. (1980), "Frequency-modulation spectroscopy: a new method for measuring weak absorptions and dispersions," *Optics Letters*, vol. 5, no. 1, pp. 15–17.

[31] Werle, P., Slemr, F., Gehrtz, M. and Brauchle, C. (1989), "Wideband noise characteristics of a lead-salt diode laser : possibility of quantum noise limited TDLAS performance," *Applied Optics*, vol. 28, no. 9, pp. 1638–1642.

[32] Wang, L. G., Riris, H., Carlisle, C. B. and Gallagher, T. F. (1988), "Comparison of approaches to modulation spectroscopy with GaAIAs semiconductor lasers: application to water vapor," *Applied Optics*, vol. 27, no. 10, pp. 2071–2077.

[33] Sigrist, M. W. (1994), *Air Monitoring by Spectroscopic Techniques*, A Wiley-Interscience publication, Wiley, New York, USA.

[34] Janik, G. R., Carlisle, C. B. and Gallagher, T. F. (1986), "Two-tone frequency-modulation spectroscopy," *Journal of the Optical Society of America B*, vol. 3, no. 8, pp. 1070–1074.

[35] Hennig, O., Strzoda, R., Mágori, E., Chemisky, E., Tump, C., Fleischer, M., Meixner, H. and Eisele, I. (2003), "Hand-held unit for simultaneous detection of methane and ethane based on NIR-absorption spectroscopy," *Sensors and Actuators, B: Chemical*, vol. 95, no. 1-3, pp. 151–156.

[36] Masiyano, D. (2008), *Use of diffuse reflections in tunable diode laser spectroscopy*, Ph.D. thesis, Cranfield University, Cranfield.

[37] Maddaloni, P., Malara, P., Gagliardi, G. and De Natale, P. (2006), "Two-tone frequency modulation spectroscopy for ambient-air trace gas detection using a

portable difference-frequency source around 3 μm," *Applied Physics B: Lasers and Optics*, vol. 85, no. 2-3, pp. 219–222.

[38] Brewster, D. (1815), "On the laws which regulate the polarisation of light by reflection from transparent bodies," *Philosophical Transactions of the Royal Society of London*, vol. 105, pp. 125–159.

[39] White, J. U. (1942), "Long optical paths of large aperture," *Journal of the Optical Society of America*, vol. 32, no. 5, pp. 285–288.

[40] Ferguson, D., Rao, K., Mickelson, M. and Larson, L. (1993), "An Experimental Study of the 4-0 and 5-0 Quadrupole Vibration Rotation Bands of H_2 in the Visible," *Journal of Molecular Spectroscopy*, vol. 160, no. 2, pp. 315–325.

[41] Herriott, D. R. and Schulte, H. J. (1965), "Folded optical delay lines," *Applied Optics*, vol. 4, no. 8, pp. 883–889.

[42] Thorlabs Inc., "Herriott cell design and example mirrors," https://www.thorlabs.com/newgrouppage9.cfm?objectgroup_id=8169, Date Accessed: 05/07/2017.

[43] Li, C., Dong, L., Zheng, C. and Tittel, F. K. (2016), "Compact TDLAS based optical sensor for ppb-level ethane detection by use of a 3.34μm room-temperature CW interband cascade laser," *Sensors and Actuators B: Chemical*, vol. 232, pp. 188–194.

[44] Venkatesh, C. G., Eng, R. S and Mantz, A. W. (1980), "Tunable diode laser-integrating sphere systems : a study of their output intensity characteristics," *Applied Optics*, vol. 19, no. 10, pp. 1704–1710.

[45] Tranchart, S., Bachir, I. H. and Destombes, J. L. (1996), "Sensitive trace gas detection with near-infrared laser diodes and an integrating sphere," *Applied Optics*, vol. 35, no. 36, pp. 7070–4.

[46] Bergin, S., Hodgkinson, J., Francis, D. and Tatam, R. P. (2016), "Integrating cavity based gas cells: a multibeam compensation scheme for pathlength variation," *Optics Express*, vol. 24, no. 12, pp. 13647–13664.

[47] Laser Components GmbH, "Working with Hollow Silica Waveguides," http://www.lasercomponents.com/fileadmin/user_upload/home/Datasheets/polymicro/hsw_info.pdf, Date Accessed: 21/06/2015.

[48] Francis, D., Hodgkinson, J., Livingstone, B., Black, P. and Tatam, R. P. (2016), "Low-volume, fast response-time hollow silica waveguide gas cells for mid-IR spectroscopy," *Applied Optics*, vol. 55, no. 25, pp. 6797–6806.

[49] Triki, M., Nguyen Ba, T. and Vicet, A. (2015), "Compact sensor for methane detection in the mid infrared region based on Quartz Enhanced Photoacoustic Spectroscopy," *Infrared Physics and Technology*, vol. 69, pp. 74–80.

[50] Jahjah, M., Jiang, W., Sanchez, N. P., Ren, W., Patimisco, P., Spagnolo, V., Herndon, S. C., Griffin, R. J. and Tittel, F. K. (2014), "Atmospheric CH_4 and N_2O measurements near Greater Houston area landfills using a QCL-based QEPAS sensor system during DISCOVER-AQ 2013." *Optics letters*, vol. 39, no. 4, pp. 957–60.

[51] Fischer, C. and Sigrist, M. W. (2002), "Trace-gas sensing in the 3.3-μm region using a diode-based difference-frequency laser photoacoustic system," *Applied Physics B: Lasers and Optics*, vol. 75, no. 2-3, pp. 305–310.

[52] Masiyano, D., Hodgkinson, J. and Tatam, R. P. (2010), "Gas cells for tunable diode laser absorption spectroscopy employing optical diffusers. Part 2: Integrating spheres," *Applied Physics B*, vol. 100, no. 2, pp. 303–312.

[53] Lin, H., Gao, F., Ding, Y., Yan, C. and He, S. (2016), "Methane detection using scattering material as the gas cell," *Applied Optics*, vol. 55, no. 28, p. 8030.

[54] Yu, Y., Sanchez, N. P., Griffin, R. J. and Tittel, F. K. (2016), "CW EC-QCL-based sensor for simultaneous detection of H_2O, HDO, N_2O and CH_4 using multi-pass absorption spectroscopy," *Optics Express*, vol. 24, no. 10, p. 10391.

[55] Dong, L., Tittel, F. K., Li, C., Sanchez, N. P., Wu, H., Zheng, C., Yu, Y., Sampaolo, A. and Griffin, R. J. (2016), "Compact TDLAS based sensor design using interband cascade lasers for mid-IR trace gas sensing," *Optics Express*, vol. 24, no. 6, p. A528.

[56] Dong, L., Li, C., Sanchez, N. P., Gluszek, A. K., Griffin, R. J. and Tittel, F. K. (2016), "Compact CH4 sensor system based on a continuous-wave, low power consumption, room temperature interband cascade laser," *Applied Physics Letters*, vol. 108, no. 1, p. 011106.

[57] Webster, C. and May, R. (1987), "Simultaneous in situ measurements and diurnal variations of NO, NO_2, O_3, jNO_2, CH_4, H_2O, and CO_2 in the 40 to 26km region using an open path tunable diode laser spectrometer," *Journal of Geophysical Research*, vol. 92, no. D10, pp. 11931–11950.

[58] Richard, E., Kelly, K., Winkler, R., Wilson, R., Thompson, T., McLaughlin, R., Schmeltekopf, A. and Tuck, A. (2002), "A fast-response near-infrared tunable diode laser absorption spectrometer for in situ measurements of CH_4 in the upper troposphere and lower stratosphere," *Applied Physics B: Lasers and Optics*, vol. 75, no. 2-3, pp. 183–194.

[59] Hacker, J. M., Chen, D., Bai, M., Ewenz, C., Junkermann, W., Lieff, W., Mcmanus, B., Neininger, B., Sun, J., Coates, T., Denmead, T., Flesch, T., Mcginn, S. and Hill, J. (2016), "Using airborne technology to quantify and apportion emissions of CH_4 and NH_3 from feedlots," *Animal Production Science*, vol. 56, no. 3, pp. 190–203.

[60] Christensen, L. E., Webster, C. R. and Yang, R. Q. (2007), "Aircraft and balloon

in situ measurements of methane and hydrochloric acid using interband cascade lasers," *Applied Optics*, vol. 46, no. 7, pp. 1132–8.

[61] Nadezhdinsky, A. I., Ponurovsky, Y. Y., Shapovalov, Y. P., Popov, I. P., Stavrovsky, D. B., Khattatov, V. U., Galaktionov, V. V. and Kuzmichev, A. S. (2012), "Preliminary results of an aircraft system based on near-IR diode lasers for continuous measurements of the concentration of methane, carbon dioxide, water and its isotopes," *Applied Physics B*, vol. 109, no. 3, pp. 505–510.

[62] Scott, D. C., Herman, R. L., Webster, C. R., May, R. D., Flesch, G. J. and Moyer, E. J. (1999), "Airborne laser infrared absorption spectrometer (ALIAS-II) for in situ atmospheric measurements of N_2O, CH_4, CO, HCl, and NO_2 from balloon or remotely piloted aircraft platforms," *Applied Optics*, vol. 38, no. 21, pp. 4609–4622.

[63] Webster, C. R., May, R. D., Trimble, C. A., Chave, R. G. and Kendall, J. (1994), "Aircraft (ER-2) laser infrared absorption spectrometer (ALIAS) for in-situ stratospheric measurements of HCl, N_2O, CH_4, NO_2, and HNO_3," *Applied Optics*, vol. 33, no. 3, pp. 454–472.

[64] Picarro Inc., "Cavity Ring-Down Spectroscopy (CRDS)," https://www.picarro.com/technology/cavity_ring_down_spectroscopy, Date Accessed: 26/04/2018.

[65] Picarro Inc., "In-flight measurement of carbon monoxide (CO), carbon dioxide (CO2), methane (CH4) and water (H2O)," https://www.picarro.com/products_solutions/gas_analyzers/flight_co_co2_ch4_h2o, Date Accessed: 26/04/2018.

[66] Aerodyne Research Inc., "Astigmatic Multipass Absorption Cells," http://www.aerodyne.com/products/astigmatic-multipass-absorption-cells, Date Accessed: 26/04/2018.

[67] Los Gatos Research, Inc., "Greenhouse Gas Analyzer (CH4, CO2, H2O) datasheet," http://www.lgrinc.com/documents/LGR_FGGA_Datasheet%20-%2020180101.pdf, Date Accessed: 26/04/2018.

Chapter 3

Principles of Tunable Diode Laser Spectroscopy

Chapter 2 covered the different techniques available for the detection of methane, with TDLS offering the most advantageous method. Integrating Spheres were shown to be a promising gas cell for use in this project. This chapter aims to provide further knowledge of the theory and principles behind using TDLS and integrating spheres, along with information on analysis techniques utilised in this thesis.
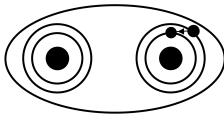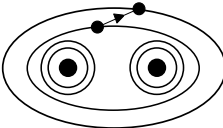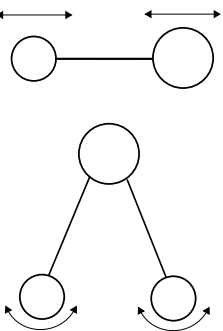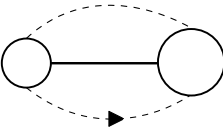
3.1 Spectroscopy theory

As stated in Chapter 2, the basic principle of optical absorption spectroscopy can be expressed using the Beer-Lambert law, as seen in equation 2.1. Optical spectroscopy operation is based on the interaction between electromagnetic radiation and matter, through emission, scattering or absorption of radiant energy. Optical absorption spectroscopy utilises the fact that each molecule has a number of different wavelengths at which molecular transitions occur [1]. These can be rotational, vibrational or electronic depending on the wavelength, as shown in Table 3.1. In these diagrams, the larger circles represent atoms, whilst the black dots indicate the positions of individual electrons. The arrows show the direction of change in each transition.

The infrared region is one of the most favourable for spectroscopic gas detection, as many of the fundamental absorption bands occur there [2]. In this region vibrational

energy is dominant, with the molecular bonds either stretching or bending. These produce changes in the dipole moment of the molecule allowing interaction with photons to occur, with energy absorbed or emitted, producing a spectrum. In the shorter wavelength regions, X-ray, visible and UV, the transitions are principally electrical, with the excitation of a valence electron moving the electronic charges in the molecule [1]. This change in the electric dipole of the molecule produces a spectrum by interacting with the electric field of radiation. In the longer wavelength microwave region, the molecular transitions are dominated by rotation. If there is a charge separation between the atoms in the molecule (for example in HCl, the hydrogen atom carries a net positive charge, whilst the chlorine carries a net negative charge), when the molecule rotates, the component dipole moment in a given direction fluctuates, producing a spectrum.

Table 3.1: *Dominant molecular transitions at various wavelengths, adapted from [1].*

X-ray 100pm - 10nm	Visible and UV 10nm - 1μm	Infra-red 1μm - 100μm	Microwave 100μm - 1cm
Change of electron configuration		Change of configuration	Change of orientation

Each molecule has a unique set of molecular transitions depending on its structure, producing absorption bands at different points in the electromagnetic spectrum. Figures 3.1 and 3.2 show the absorption bands for methane in the 3.3μm and 1650nm wavelength regions. Normally, instrumentation utilising optical spectroscopy would only focus on one absorption region to quantify the target gas concentration. This region would ideally have a strong absorption line for the target gas and no

overlapping lines from other gas species that could interfere with any measurements made.
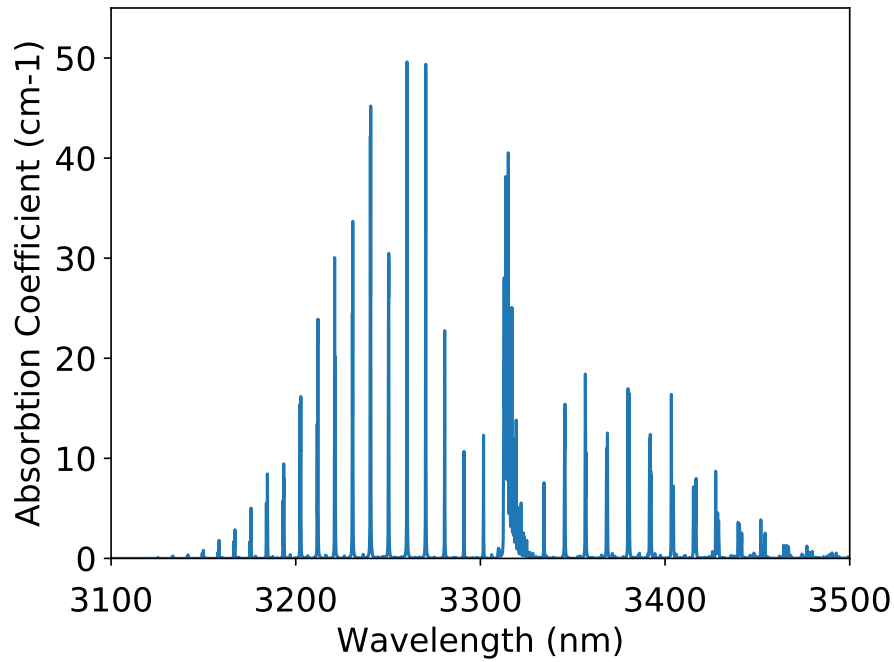
Figure 3.1: *Absorption band for methane in the 3.3μm wavelength region, plotted from the HITRAN database [3].*
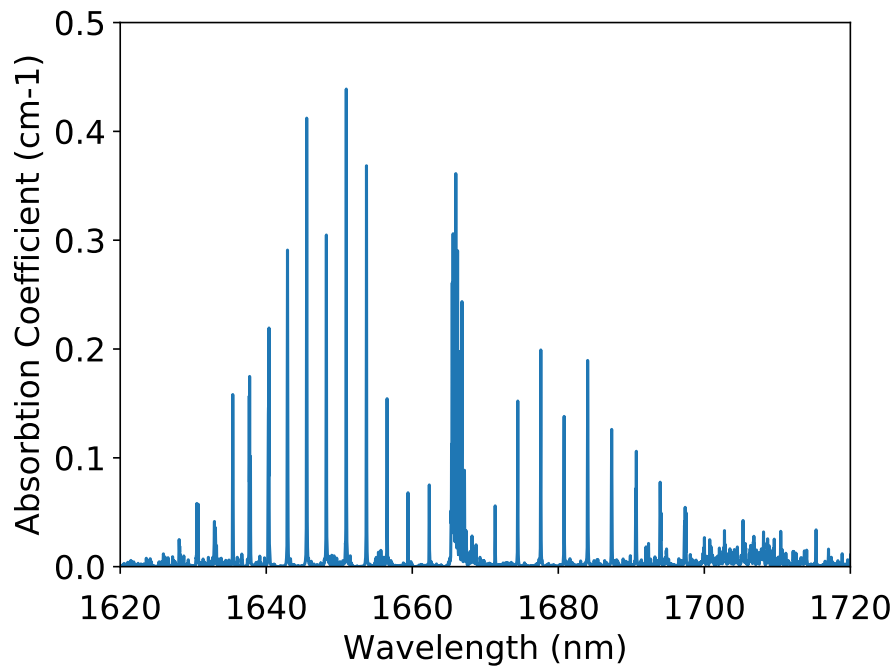
Figure 3.2: *Absorption band for methane in the 1650nm wavelength region, plotted from the HITRAN database [3].*

3.1.1 Pressure and temperature effects

Although the absorption coefficient is important in the detection of a target gas species, the line strength S (the integral of the absorption cross section $\sigma(\nu)$ over its wavenumber (ν) range), is just as, if not more fundamental. This relation can be seen in equation 3.1 for a single absorption line [2].

$$S = \int_{-\infty}^{\infty} \sigma(\nu)d\nu \tag{3.1}$$

The value of S for a given absorption line depends on the temperature of the target gas, whilst the absorption cross section, along with the line shape and width, depend both on its temperature and pressure. This dependence on temperature and pressure can be characterised into three separate line broadening regimes: Doppler, Lorentz, and Voigt.

The first of these, Doppler broadening, arises from random thermal motion of the gas molecules and dominates at pressures below approximately 10 Torr (13.3 mbar). The line shape for a Doppler-broadened absorption line has the form of a Gaussian function. As Doppler broadening only dominates at very low pressures, it only needs to be taken into account in very specific circumstances or at extremely high altitudes (above approximately 30km).

At pressures above 100 Torr (133.3 mbar), the line shapes and widths are determined primarily by collision induced broadening. In this region, the absorption line shape is determined by a Lorentzian function [4]:

$$L(\nu) = \frac{1}{\pi} \frac{\frac{1}{2}\Delta\nu_L}{(\nu - \nu_0)^2 + (\frac{1}{2}\Delta\nu_L)^2} \tag{3.2}$$

where ν_0 is the absorption line centre and $\Delta\nu_L$ is the Lorentzian line width. In general, the pressure broadened line widths in this regime depend on the gas partial pressure (self-broadening), the total pressure (foreign gas broadening, e.g. air) and

the temperature. As the background concentration of methane in the atmosphere is relatively low, the self-broadening aspect is negligible and can be ignored. For a given temperature, $\Delta\nu_L$ can be shown to increase linearly as the pressure increases [2]:

$$\Delta\nu_L = 2b_c p \qquad (3.3)$$

Where p is the gas pressure and b_c is the pressure broadening coefficient. For pressure broadened lines, the absorption cross section at ν_0 can be expressed as [2]:

$$\sigma_0 = \frac{2S}{\pi\Delta\nu_L} = \frac{S}{\pi b_c p} \qquad (3.4)$$

In the Lorentzian pressure regime, the peak absorption cross section decreases with increasing total pressure, with line widths typically being on the order of 0.1cm^{-1} at atmospheric pressure. This is approximately 1-2 orders of magnitude larger than those in the Doppler regime. This additional broadening results in significantly smaller peak cross sections, with the absorption lines of many larger molecules blending and overlapping. According to the ideal gas law, however, the change in pressure also results in a change in the total number of molecules, acting to almost compensate for the reduced strength of the measured absorption.

Measurements made at pressures between 10 and 100 Torr fall into the Voigt regime, where the line shape and width are described using a convolution of Doppler and pressure broadening functions. Typical absorption line widths in this regime fall between 5×10^{-3} and 2×10^{-2} cm^{-1}. Operation in this pressure range increases sensitivity and selectivity of a measurement system, however it does limit measurements to point sampling, where the pressure can be controlled or reduced, or to higher altitudes.

As mentioned in Chapter 1, the measurements to be taken in this project will be within the atmospheric boundary layer, with most of these occurring below an

altitude of 1km. Pressures up to this altitude fall between approximately 1100 mbar and 900 mbar. Figure 3.3 shows a representation of how a methane absorption line at 3260nm changes within this pressure window. It shows that the width and height of the absorption line decrease slightly as the pressure drops. As the change is only small, however, it should not be a significant factor during detection.
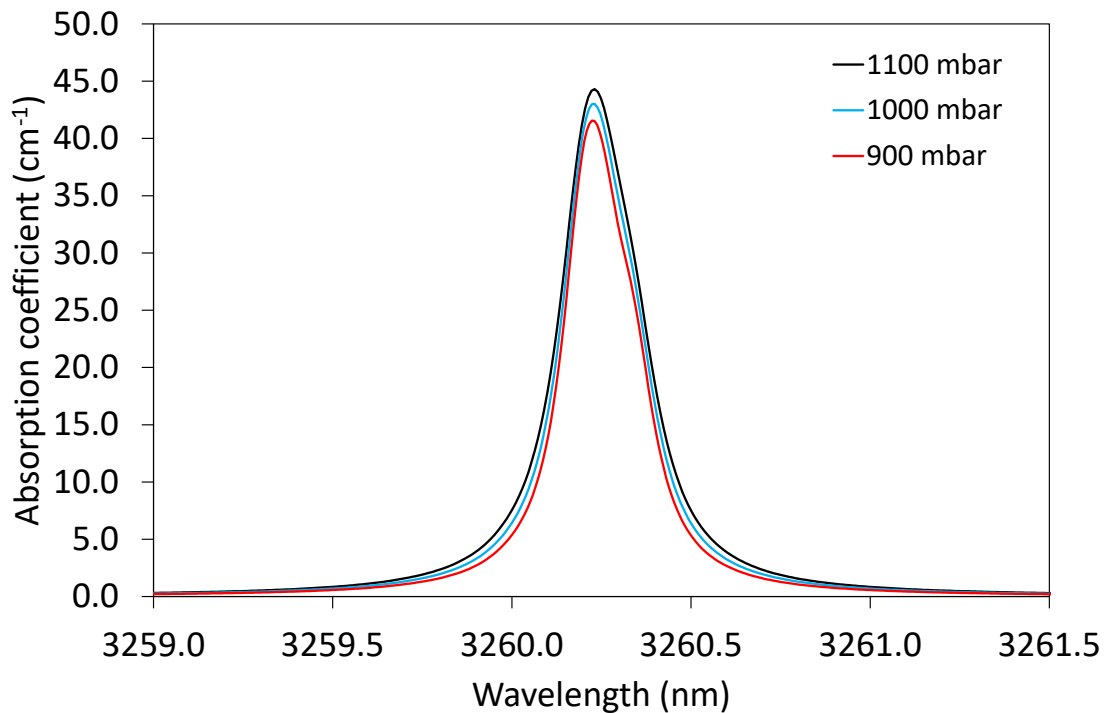
Figure 3.3: *Comparison between absorption line shapes for a methane absorption line at 3360nm at pressures between 900 mbar and 1100 mbar.*

3.2   TDLS theory

As stated in the previous chapter (section 2.5.1) direct spectroscopy operates by continuously modulating the injection current of a laser with a sawtooth or triangular waveform. Measurements of a gas absorption line are then compared with a zero-gas reference to obtain a normalised version of the gas absorption line, as shown in Figure 3.4. This follows the Beer-Lambert equations laid out in section 2.2 in Chapter 2.
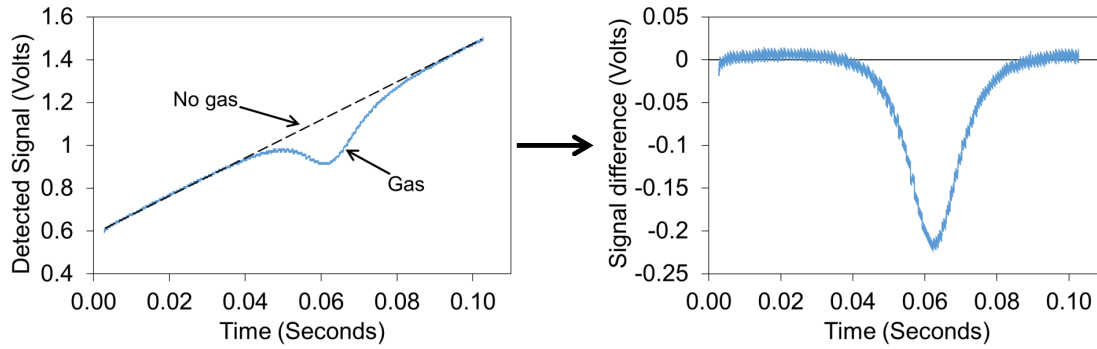
Figure 3.4: *Comparison between the raw data collected with and without the presence of methane (left) and the resultant signal difference (right).*

To determine a limit of detection (LOD) for a TDLS based system, a number of processing steps have to be made. By performing multiple zero-gas measurements, a value for the background noise level can be obtained. Making a comparison of the standard deviation of this noise against the peak value of the gas measurement, a single-point limit of detection can be obtained. This provides a simple analysis of the performance of the system.

The LOD can then be improved in a couple of different ways. By averaging the data across a length of time, the random noise in the signal can be reduced. This is discussed in more detail in sections 3.2.1 and 3.2.2. This reduces the standard deviation of the noise, decreasing the LOD. Rather than just relying on a single point in the measurement, a line fit can also be performed on the gas line, allowing for much lower LODs to be produced than would otherwise be possible. This is covered in more detail in section 3.2.3.

3.2.1 Noise sources

In a TDLS based system, a variety of noise sources can be present: detector noise, laser noise, injection current noise, optical feedback and interference fringes. These sources limit the performance of the system.

The main components of detector noise are Johnson noise, shot noise, and 1/f (pink) noise [5]. The first of these, Johnson (or thermal) noise occurs due to random fluctuations caused by thermal agitation of the charge carriers in an electrical

conductor, irrespective of the voltage applied. Thermal noise is nearly constant throughout the frequency spectrum, and is often referred to as "white" noise. Shot noise occurs as a result of the random arrival times of photons on the detector. It is independent of the modulation frequency used, however it is proportional to the square root of the laser power and detector bandwidth. Detector 1/f noise is thought to be caused by potential barriers in semiconductors and semiconductor contacts, depending greatly on what manufacturing procedures are used, particularly with respect to contacts and surfaces.

As all three noise sources depend linearly on the detector bandwidth, reducing this bandwidth by introducing a low-pass filter or using signal integration can reduce the noise levels, however this has the adverse effect of increasing the response time [5].

As a result of the fluctuations arising from technical and mechanical origins, the output of a laser will always contain some noise. This noise appears as fluctuations in the output power of the laser. These fluctuations can be traced either to the inherent behaviour of the laser diode (commonly known as intrinsic noise) or to external influences such as injection current noise, temperature instabilities, mechanical vibrations, and optical feedback.

Fluctuations in the injection current can be reduced through the use of low noise current sources, whilst temperature instabilities can be addressed using a highly stabilised controller combined with increased cooling capability (e.g. larger heatsinks or liquid cryogen Dewars). Mechanical and thermal instability can be isolated by line-locking the laser to an absorption feature or to a Fabry-Perot etalon. Intrinsic noise is produced by photon and carrier density fluctuations, refractive index fluctuations, and partition noise resulting from mode competition in multimode lasers. Intrinsic noise depends heavily on the manufacturing process, design of the laser being utilised, and on the operating current and temperature being used.

Interference fringes are a common source of noise in TDLS based systems. The

fringes themselves arise from Fabry-Perot etalons produced between reflecting or scattering surfaces such as mirrors, detector windows, semiconductor surfaces, and components of multipass cells. The free spectral range (FSR) Δv corresponding to a Fabry-Perot etalon of length L can be expressed using the following equation [6]:

$$\Delta v = \frac{c}{2nL} \tag{3.5}$$

where c is the speed of light in a vacuum and n is the refractive index of the cavity. Measurement of the FSR allows the optical elements responsible for the etalon to be identified and potentially for the fringes to be reduced. Removing the fringes from a signal cannot however be done through simple subtraction, as thermal and mechanical instabilities, even if slight, can cause the etalon spacing to change with time.

A number of different approaches to reducing interference fringes have been found to be effective. More basic adjustments to the set-up used include using reflective optics rather than refractive optics wherever possible, avoiding parallel surfaces (for example aligning windows at the Brewster angle for the wavelength of the laser used), avoiding sharp focus, and through careful selection of the laser diode, modulation waveform and amplitude. Mechanically oscillating the pathlength with an external device has also been shown to average out and reduce the fringes.

3.2.2   Allan variance and deviation

Allan variance and deviation plots are used to characterise the stability of a system and help to analyse the noise and drift in signal over time [7]. Whilst white noise can be reduced to zero by averaging over an infinite number of measurements, there are other types of uncertainty that may cause the signal to drift and will not average out over time.

As described in 1966 by D. W. Allan [8] and further in 1993 by Werle *et al* [7], the Allan variance is calculated from a time series data set. For a series of N data

points, the average value A can be calculated using equation 3.6, where x_i refers to the individual points in the time series. The variance σ^2 can then be defined using equation 3.7, providing the highest and lowest level of the data spread, with the variance of the mean as $Var(A) = \sigma^2/N$.

$$A = \frac{1}{N} \sum_{i=1}^{N} x_i \tag{3.6}$$

$$\sigma^2 = \frac{1}{N-1} \sum_{i=1}^{N} (x_i - A)^2 \tag{3.7}$$

The elements of the original data set can then be divided into M subsets containing k elements, where $M = N/k$. For each of these M subgroups, an average value of A_n and a corresponding variance σ_n^2 can be calculated, as shown in equations 3.8 and 3.9. The variance of the mean is then defined by $Var(A_n) = \sigma_n^2/k$, with n denoting the subgroup number and k the number of elements in the subgroup n.

$$A_n = \frac{1}{k} \sum_{l=1}^{k} x_{(n-1)k+l} \tag{3.8}$$

$$\sigma_n^2 = \frac{1}{2(k-1)} \sum_{l=1}^{k} (x_{(n-1)k+l} - A_n)^2 \tag{3.9}$$

The analysis of a long dataset can be very time consuming; as such it would be beneficial to utilise a more efficient method to determine the optimum averaging group size. The definition of the general variance can be described in the following way:

$$\sigma_A^2(M, T, \tau) = \frac{1}{2(M-1)} \sum_{n=1}^{M} (A_n - A_{n-1})^2 \tag{3.10}$$

where M is the number of groups used in obtaining a sample variance, T is the time interval between the beginning of two consecutive measurements, and τ is the integration time. The variance of the means σ_A^2 is the well-known "Allan Variance",

with σ_A defined as the Allan deviation. This was introduced by Allan [8] in 1966 for the characterisation of frequency standards. The log-log plot of an Allan deviation often follows the form of a 'V' curve, as shown in Figure 3.5. At short timescales, white noise is averaged down to a minimum point, before rising at longer timescales due to the effects of drift. The turning point in the dataset occurs at the optimum averaging time period.
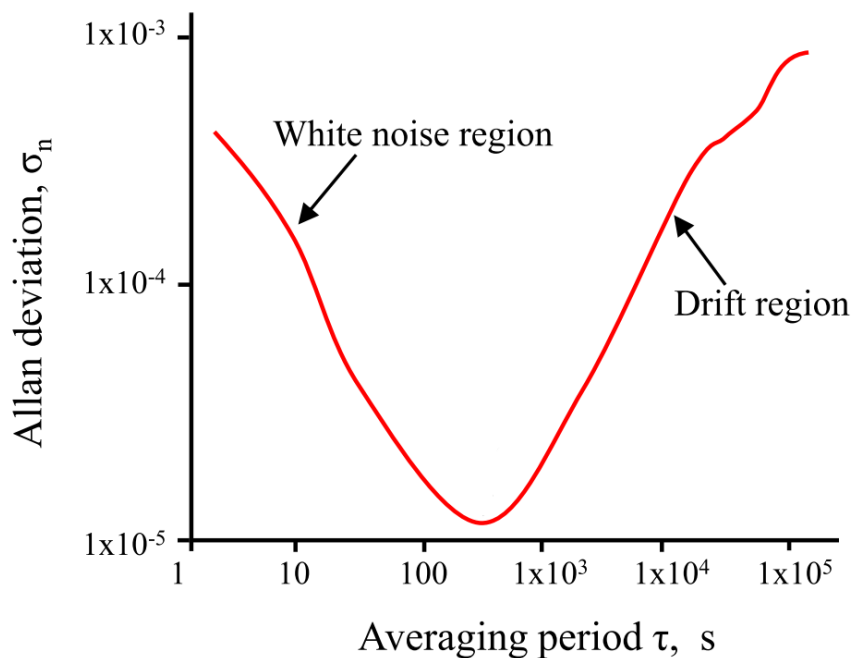
Figure 3.5: *Example of the form of an Allan deviation graph, adapted from [9].*

3.2.3   Absorption line fitting

To help reduce the limit of detection, a fitting algorithm is often applied to the measurement of the absorption line. These algorithms, as shown in Figure 3.6, use a least squares curve fitting approach to fit a curve using set parameters to any absorption features being analysed. As they follow the form of an absorption line, rather than a single point, this allow any absorption lines being observed to be tracked into the background noise present. This allows much lower concentrations to be analysed than would otherwise be possible.
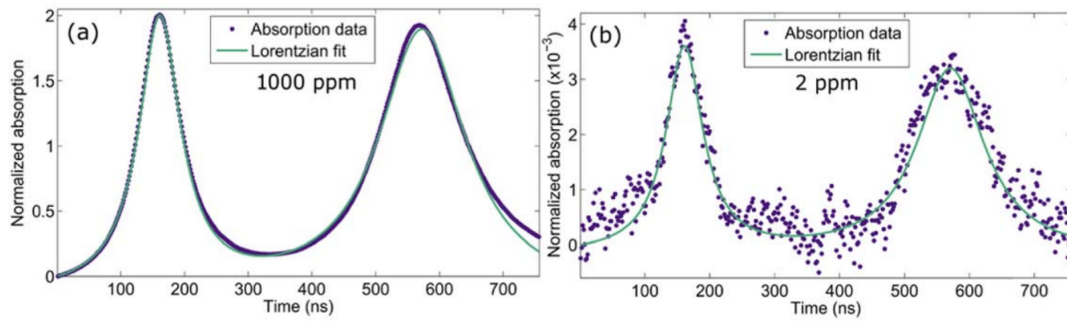
Figure 3.6: *Example of a fitting algorithm applied to a pair of methane absorption lines at concentrations of 1000ppm (a) and 2ppm (b), taken from [10].*

A common algorithm used for this technique is the Levenberg-Marquardt algorithm. The algorithm was first published in 1944 by Kenneth Levenberg [11] and rediscovered in 1963 by Donald Marquardt [12]. This algorithm takes the following form:

$$(\mathbf{J}^T \cdot \mathbf{J} + \lambda_d \cdot (\mathbf{J}^T \cdot \mathbf{J})) \cdot \delta = \mathbf{J}^T \cdot (\mathbf{y} - \mathbf{f}(\mathbf{a})) \tag{3.11}$$

where $\mathbf{f}$ is the vector of the iterations of the model curve $f(x_i, \mathbf{a})$, with $\mathbf{a}$ being the initial guess for the parameter vector. $\mathbf{J}$ and $\mathbf{J}^T$ are the Jacobian matrix and its transpose of $\mathbf{f}$, $\mathbf{y}$ is the vector of the individual y_i values (paired to the x_i values), δ is the iterative step value, and λ_d is a non-negative damping factor adjusted at each iteration.

For example, for a single absorption line, initial parameter values for the height, full-width half-maximum, and position of a Lorentzian peak are input into the algorithm alongside a damping factor and iterative step value. If this damping factor results in the reduction of the residual, the algorithm continues to the next iteration, with the damping factor modified by the iterative step value. This process continues until either the residual falls below a predefined limit, or the residual increases (in which case values from the previous iteration are output).

3.3　Integrating spheres

A brief introduction to integrating spheres was covered in Chapter 2, section 2.6.4. Integrating Spheres were first developed in 1900 by R. Ulbricht [13] to accurately measure the total luminous flux of different light sources. The sphere allowed flux measurements to be made in five minutes rather than half an hour [14]. A picture of the set up used can be seen in Figure 3.7.
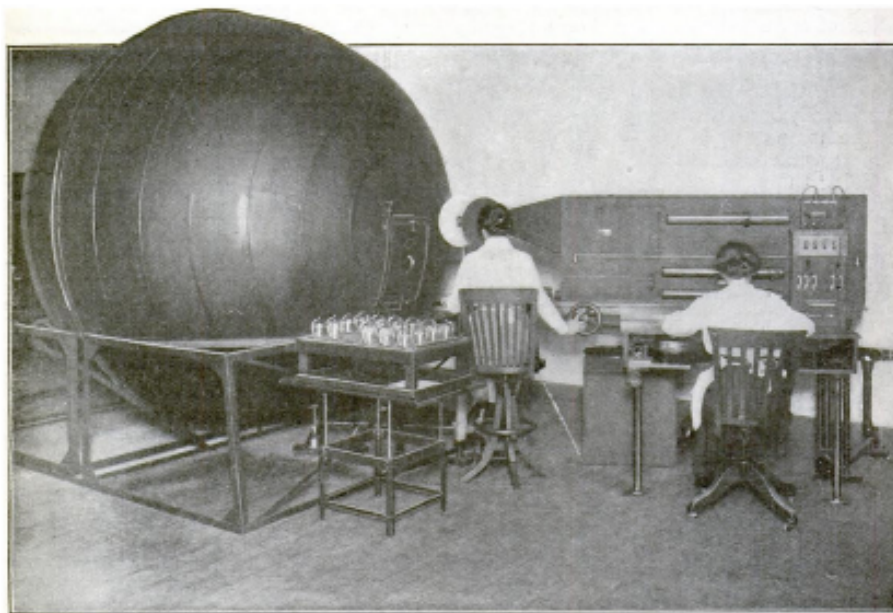
Figure 3.7: *A 100 inch sphere photometer, taken from [14].*

As stated previously, in 1980, Venkatesh *et al* [15] adapted an integrating sphere for use as a gas absorption cell. For a diffuse cavity with a uniform light field and of any geometry, such as an integrating sphere, the effective optical pathlength (EOPL, ℓ_{eff}) can be expressed using the following equation [16]:

$$\ell_{eff} = ML_{ave} \tag{3.12}$$

where L_{ave} is the single-pass average pathlength and M is the reflection multiplier, a function of the reflectivity ρ of the diffuse internal surface and the port fraction f (the sum of all port areas/inner surface area). This relationship can be expressed as:

$$M = \frac{\rho}{1 - \rho(1 - f)} \tag{3.13}$$

For example, a 10cm diameter integrating sphere with a Spectralon coated interior

surface with a reflectivity of 0.99 and two 5mm diameter ports would have a reflection multiplier of 88.1, producing an EOPL of 8.81m. In practice, however, it is often found that the theoretical pathlength does not match that of the pathlength observed. This is often due to fouling on the sphere wall (such as dirt, grime, etc.), an imperfect applied coating, or a combination of both. This has the effect of reducing the sphere's reflectivity and, as a result, its effective pathlength. As such, the actual pathlength of the sphere often needs to be calibrated. This is done by making a comparison against a gas cell of known length L_{cell} (often a single-pass cell). A known concentration of a target gas is measured in each cell, with the sphere pathlength L_{sphere} calculated using:

$$L_{sphere} = \frac{A_{sphere}}{A_{cell}} L_{cell} \tag{3.14}$$

where A_{sphere} and A_{cell} are the absorption measurements for the sphere and cell respectively.

3.3.1   Noise and error

There are a number of potential noise sources that could become an issue when utilising integrating spheres, with the main potential problems arising from contamination of the sphere wall, speckle noise, and interference fringes. Interference fringes for conventional cells have previously been covered, in section 3.2.1.

It was shown in the previous section that the reflectivity of the integrating sphere has a significant impact on the effective pathlength. As a result, if contamination of the sphere wall was to occur, an error could be introduced in the detected gas absorption. Bergin *et al* [17] have shown that a contamination covering 1.2% of the sphere wall resulted in an error in the measured gas absorption coefficient of approximately 41%. To correct for this, the effective pathlength of the sphere would either need to be regularly recalibrated, or a correction scheme introduced. Such correction schemes include calibration with oxygen in air [16], normalising by dry sphere response change [18], measuring the temporal decay in a pulsed system [19],

and real-time pathlength adjustment using a four beam ratiometric setup [17].

Speckle noise forms when light is scattered in random directions when incident on a rough or diffuse surface. When a coherent light source, such as a laser, illuminates a diffuse surface, the reflected components interfere, producing a complex, stationary interference pattern that has a granular appearance. The reflected wave from an optically rough surface consists of contributions from numerous independent scattering areas.

Light scattered from different parts of the surface will have different pathlengths as a result of the surface profile, with an interference fringe pattern occurring when two or more reflected beams intersect. As the light has high coherence, any two points can produce an interference pattern, with each pairs fringes occurring at different orientation and separation. The speckle pattern that results is a complex mixture of bright and dark spots, caused by the constructive and destructive interference that takes place. The strength and form of the interference pattern that results is dependent on both the wavelength of light used and the topography of the diffuse surface utilised.

Optical feedback of the laser occurs due to backscattered or back reflected light from optical components coupling into the laser cavity, resulting in modulations in the amplitude and frequency of the lasing field [20]. Through tuning the injection current or temperature of the laser, or through relative motion between the laser and a remote target, periodic signals will be generated with similar properties to those generated by a Fabry-Perot etalon [21]. It has been shown that optical feedback in TDLS can introduce degradation in the detected absorption line shape and broadening of the absorption spectra [22]. Through the use of reflecting optics, careful alignment of optical components, and utilising optical isolators and apertures, optical feedback can be reduced, however a reduction in the detected laser intensity can occur as a result [23].

3.3.2   Project suitability

There are a number of distinct advantages to utilising integrating spheres over other forms of multipass cells. The two main advantages are the tolerance to misalignment and, as a result of this, the ability to have free-space coupling.

The tolerance to misalignment arises from the fact that integrating spheres do not have a fixed path that the light travels along, rather an effective optical pathlength. This means that the orientation of the incident light into the sphere is not a factor in determining the pathlength and therefore the limit of detection.

Due to this alignment tolerance, free-space optics can be utilised, reducing the amount of additional optics needed to introduce light into the sphere, such as collimators, couplers and optical fibre. Instead, the laser and detectors can potentially be butted directly up to the sphere ports, potentially increasing the laser power being utilised and reducing the volume that the equipment takes up. This also reduces the potential for background methane outside the cell to affect any measurements being made. For butt-coupling to be utilised, optical feedback effects would need to be investigated as these have been performance limiting in the near infrared.

There are, however, a number of potential risks that will need to be investigated before it can be definitively stated that integrating spheres are the best option for this project. The effective optical pathlength of an integrating sphere is often not as long as those seen in alternative multipass cells. This is especially true in the mid-infrared where the gold coating used has a lower surface reflectivity. Whether the resultant pathlength would produce a satisfactory limit of detection would need to be investigated.

Speckle interference from the sphere could also potentially be an issue. This would need to be measured to determine if it can be seen above the noise floor of the detectors. Although the detectors used in the mid-infrared have an inherently higher noise level, it would still need to be analysed to see if it could cause problems.

3.4   Conclusions

In this chapter, a review of the principles behind optical spectroscopic detection of methane has been performed, including how different wavelengths of light affect the molecule, allowing for detections to be made, along with how different pressure levels can affect the absorption line shape.

A description of the procedure used in TDLS based systems was provided alongside an overview of the different noise sources that need to be accounted for and minimised. A description of the Allan variance was given along with the theory behind it, before the Levenberg-Marquardt absorption line fitting technique was discussed.

Finally, further information and theory behind the use of integrating spheres as a multipass gas cell was provided. Some basic relations and equations describing the spheres were shown, along with a discussion of the noise sources present. An overview describing the advantages and potential risks that integrating spheres have for use in this project was presented. Integrating spheres show promise for in-flight applications due to their tolerance to misalignment, however there are a number of potential risks, such as speckle interference, that need to be investigated.

References

[1] Banwell, C. N. and McCash, E. M. (1994), *Fundamentals of molecular spectroscopy*, European Chemistry Series, McGraw-Hill, London, UK.

[2] Sigrist, M. W. (1994), *Air Monitoring by Spectroscopic Techniques*, A Wiley-Interscience publication, Wiley, New York, USA.

[3] Rothman, L., Gordon, I., Babikov, Y., Barbe, A., Chris Benner, D., Bernath, P., Birk, M., Bizzocchi, L., Boudon, V., Brown, L., Campargue, A., Chance, K., Cohen, E., Coudert, L., Devi, V., Drouin, B., Fayt, A., Flaud, J.-M., Gamache, R., Harrison, J., Hartmann, J.-M., Hill, C., Hodges, J., Jacquemart, D., Jolly, A., Lamouroux, J., Le Roy, R., Li, G., Long, D., Lyulin, O., Mackie, C., Massie, S., Mikhailenko, S., Müller, H., Naumenko, O., Nikitin, A., Orphal, J., Perevalov, V., Perrin, A., Polovtseva, E., Richard, C., Smith, M., Starikova, E., Sung, K., Tashkun, S., Tennyson, J., Toon, G., Tyuterev, V. and Wagner, G. (2013), "The HITRAN2012 molecular spectroscopic database," *Journal of Quantitative Spectroscopy and Radiative Transfer*, vol. 130, pp. 4–50.

[4] Weisstein, E.W., "Lorentzian Function from MathWorld - A Wolfram Web Resource," http://mathworld.wolfram.com/LorentzianFunction.html, Date Accessed: 23/04/2018.

[5] Schiff, H. I., Mackay, G. I. and Bechara, J. (1994), "The Use of Tunable Diode Laser Absorption Spectroscopy for Atmospheric Measurements," in: Sigrist, M. W. (editor), "Air Monitoring by Spectroscopic Techniques," Wiley, New York, pp. 239–334.

[6] RP Photonics Consulting GmbH, "Free Spectral Range," https://www.rp-photonics.com/free_spectral_range.html, Date Accessed: 26/04/2018.

[7] Werle, P., Mücke, R. and Slemr, F. (1993), "The limits of signal averaging in atmospheric trace-gas monitoring by tunable diode-laser absorption spectroscopy

(TDLAS)," *Applied Physics B: Photophysics and Laser Chemistry*, vol. 57, no. 2, pp. 131–139.

[8] Allan, D. W. (1966), "Statistics of Atomic Frequency Standards," *Proceedings of the IEEE*, vol. 54, no. 2, pp. 221–230.

[9] Chowdhury, S. A. (2015), *Fibre optic hydrogen sensing for long term use in explosive environments*, Ph.D. thesis, Cranfield University, Cranfield.

[10] Francis, D., Hodgkinson, J., Livingstone, B., Black, P. and Tatam, R. P. (2016), "Low-volume, fast response-time hollow silica waveguide gas cells for mid-IR spectroscopy," *Applied Optics*, vol. 55, no. 25, pp. 6797–6806.

[11] Levenberg, K. (1944), "A method for the solution of certain non-linear problems in least squares," *Quarterly of Applied Mathematics*, vol. 2, no. 278, pp. 164–168.

[12] Marquardt, D. W. (1963), "An Algorithm for Least-Squares Estimation of Nonlinear Parameters," *Journal of the Society for Industrial and Applied Mathematics*, vol. 11, no. 2, pp. 431–441.

[13] Ulbricht, R. (1900), "Die Bestimmung der mittleren, räumlichen Lichtintensität durch nur eine Messung," *Elektrotech. Zeit*, vol. 29, pp. 595–597.

[14] Popular Science Monthly (1916), "A quick method of measuring light," vol. 89, no. 6, p. 848.

[15] Venkatesh, C. G., Eng, R. S. and Mantz, A. W. (1980), "Tunable diode laser-integrating sphere systems : a study of their output intensity characteristics," *Applied Optics*, vol. 19, no. 10, pp. 1704–1710.

[16] Yu, J., Zheng, F., Gao, Q. and Li, Y. (2013), "Effective optical path length investigation for cubic diffuse cavity as gas absorption cell," *Applied Physics B: Lasers and Optics*, vol. 116, no. 1, pp. 135–140.

[17] Bergin, S., Hodgkinson, J., Francis, D. and Tatam, R. P. (2016), "Integrating cavity based gas cells: a multibeam compensation scheme for pathlength variation," *Optics Express*, vol. 24, no. 12, pp. 13647–13664.

[18] Dana, D. R. and Maffione, R. A. (2006), "A New Hyperspectral Spherical-Cavity Absorption Meter," *Ocean Sciences Meeting (Eos Transactions American Geophysical Union, 2006).*

[19] Cone, M. T., Musser, J. A., Figueroa, E., Mason, J. D. and Fry, E. S. (2015), "Diffuse reflecting material for integrating cavity spectroscopy, including ring-down spectroscopy," *Applied Optics*, vol. 54, no. 2, pp. 334–346.

[20] Giuliani, G., Norgia, M., Donati, S. and Bosch, T. (2002), "Laser diode self-mixing technique for sensing applications," *Journal of Optics A: Pure and Applied Optics*, vol. 4, no. 6, pp. S283–S294.

[21] Schilt, S. and Thévenaz, L. (2004), "Experimental method based on wavelength-modulation spectroscopy for the characterization of semiconductor lasers under direct modulation," *Applied Optics*, vol. 43, no. 22, pp. 4446–4453.

[22] Fukuda, M., Ooyama, S., Utsumi, A., Kondo, Y., Kurosaki, T. and Masuda, T. (2008), "Effect of optical feedback noise on tunable diode laser spectroscopy," *Applied Physics B: Lasers and Optics*, vol. 90, no. 2, pp. 269–272.

[23] Masiyano, D. (2008), *Use of diffuse reflections in tunable diode laser spectroscopy*, Ph.D. thesis, Cranfield University, Cranfield.

Chapter 4

Tunable diode laser spectroscopy with a new near infrared external cavity diode laser

The theory and principles behind spectroscopy and TDLS have been described in Chapter 3. This chapter outlines work performed with a new type of laser in the near infrared, with comparisons made against a standard DFB diode laser. This new laser has been shown to have good potential for use with gas sensing. This chapter therefore aims to evaluate its current situation for use in TDLS and for its suitability for use in challenging conditions.

4.1   Near infrared lasers

Typically in the near infrared, distributed feedback (DFB) diode lasers or vertical cavity surface emitting lasers (VCSEL) are utilised for use with TDLS. Each laser must be custom made at a distinct wavelength to target a specific gas absorption line, an example of which can be seen in Figure 4.1. To perform TDLS based measurements on these absorption lines, a tuning range of at least 0.1nm is required.

To provide a stable operating wavelength for the DFB laser, a grating structure is employed, usually written above the active wavelength region. The grating acts as an optical filter, causing a single wavelength to feed back into the gain medium and

lase. As the grating provides this optical feedback, reflections from the facets or cleaved mirrors are not required for wavelength selection, unlike in Fabry-Perot laser diodes. An example of the internal schematic of a DFB laser diode can be observed in Figure 4.2.
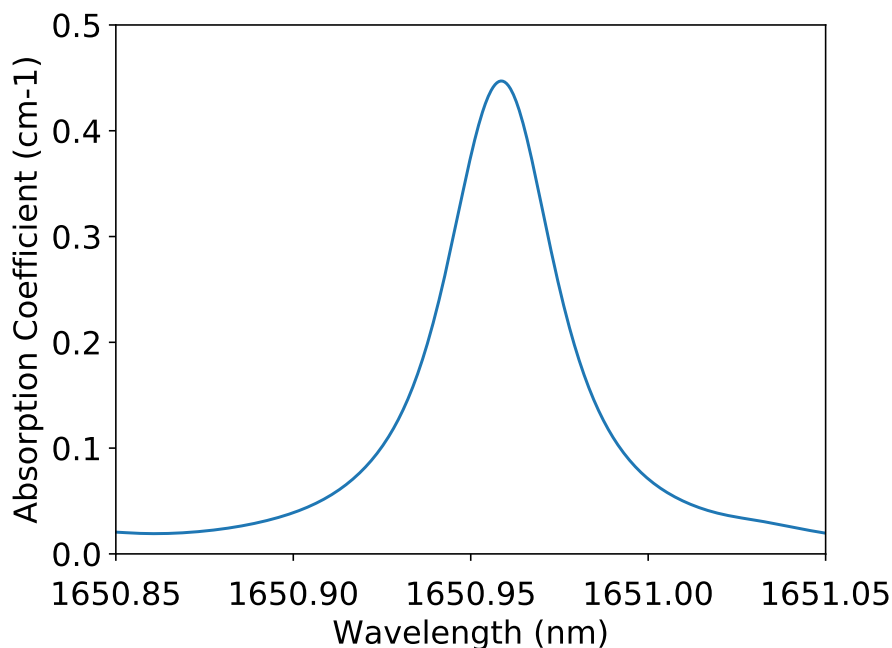
Figure 4.1: *Methane absorption line at 1650.96nm, taken from HITRAN database [1].*
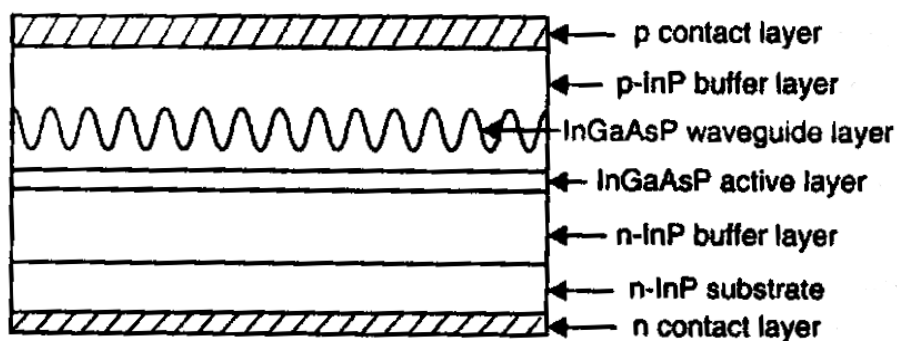
Figure 4.2: *Schematic of the internal structure of a DFB laser, taken from [2].*

VCSELs are a form of laser diode that have laser beam emission perpendicular to the surface, contrary to a standard diode laser where the emission comes from the edge of the device. A schematic of the typical gain structure of these lasers can be

seen in Figure 4.3. These devices hold a number of production advantages over other laser diodes. Edge emitting devices can only be tested at the end of the production process, meaning that if there are any defects, they are not detected until it is too late, with time and material being wasted. VCSELs, however, can be tested at numerous stages along the production process to check for material quality and for any issues that may occur.
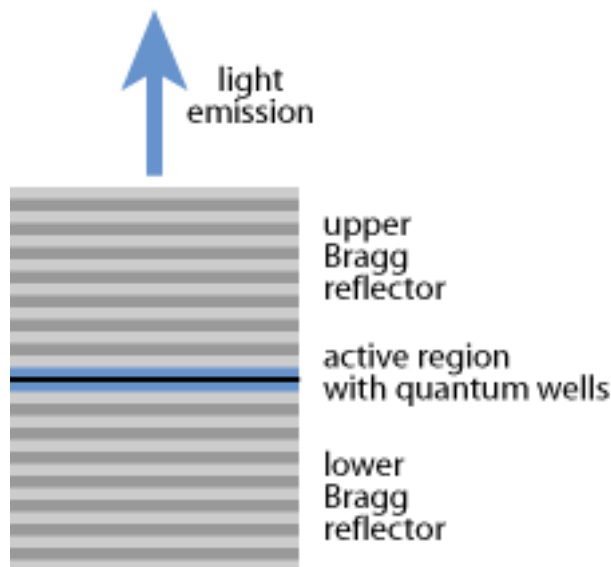
Figure 4.3: *Schematic gain structure of a VCSEL, taken from [3].*

Both of these devices offer tunable, narrow linewidth lasers that can be manufactured to operate at a selected wavelength to allow for the detection of methane. However, they are limited in that if a wavelength outside of the range provided by the purchased laser is sought, a new laser would have to be acquired, often at quite a high cost to the user.

External cavity diode lasers (ECDL) offer narrow linewidth operation and single-mode output with the ability to tune over a wide wavelength range [4]. With these lasers, a diode is often utilised as a gain medium specifically designed for use with an ECDL. These can be obtained commercially, often known as "gain chips", especially in the Near IR region. A separate wavelength-selective element, generally a grating, is then normally integrated into the external cavity. This allows the laser to be tuned to a specific wavelength, similar to the VCSEL and DFB lasers. Separating

these components provides a simpler, more cost effective way to fabricate lasers for wavelength sensitive applications. The most common configurations using this technique are the Littrow [5] and Littman-Metcalf [6]. Configurations for each of these can be observed in Figure 4.4. The Littrow configuration is the simplest of the two, involving fewer optical elements and less initial alignment, however the Littman-Metcalf configuration has an advantage in that it avoids beam deflection during tuning.
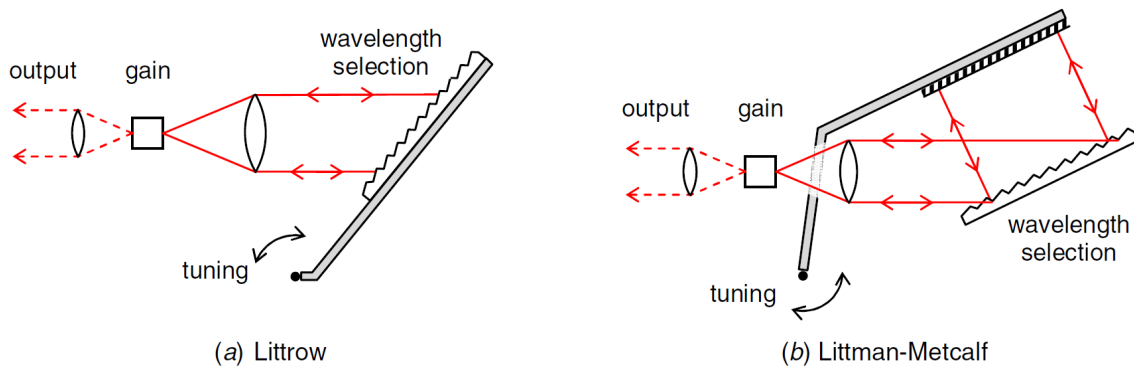
Figure 4.4: *Schematic diagrams of the Littrow (a) and Littman-Metcalf (b) configurations for ECDLs, taken from [7].*

4.2 Characterisation of Laser

The ECDL used in this chapter was developed by Lynch *et al* [8] and loaned from the University of Southampton for testing purposes. It uses a planar silica-on-silicon platform incorporating a UV-written Bragg grating as the wavelength selective element of the laser cavity. This design architecture means that custom wavelengths can be written "on demand" with relatively low capital investment.

4.2.1 Description of ECBSL

The external cavity Bragg stabilised laser (ECBSL) used a 1650nm InP gain-chip (Thorlabs SAF1091H) with an external cavity planar lightwave circuit (PLC) . The gain chip has a highly reflective rear facet (90%) and an anti-reflective coated, angle terminated waveguide. The gain chip was directly butt-coupled to the external cavity PLC, containing the direct UV-written waveguide and Bragg grating, as shown in

Figure 4.5. A heating assembly had been deposited directly over the Bragg grating to provide thermal tuning.
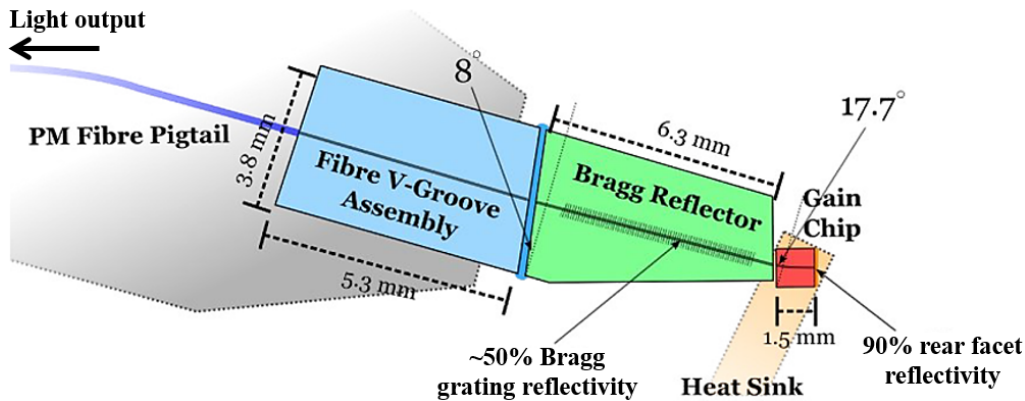
Figure 4.5: *Schematic diagram of ECBSL, adapted from [8].*

As shown in Figure 4.6, the Bragg grating and Fibre V-groove assembly were mounted on a Thorlabs Nanomax 3-axis stage, separating the primary wavelength selective element from the gain element. Using an optical spectrum analyser (OSA) (Yokogawa AQ6370C) to monitor the laser output power and a microscope to observe the alignment, the Bragg grating could be gradually manoeuvred into a position such that the laser power was at a maximum. An alignment tolerance of approximately 1μm in each axis was required to correctly align the Bragg grating to the gain-chip.

4.2.2   ECBSL performance

An example of the laser output can be seen in Figure 4.7. The figure demonstrates that the device exhibits sidemode suppression ratios of >40dB. It has also been noted that it has a relative intensity noise of <-150dB/Hz [9]. These figures are comparable to other commercially available ECDLs, with a pigtailed ECDL from Thorlabs (SFL1620S) demonstrating a relative intensity noise of -150dB/Hz [10].
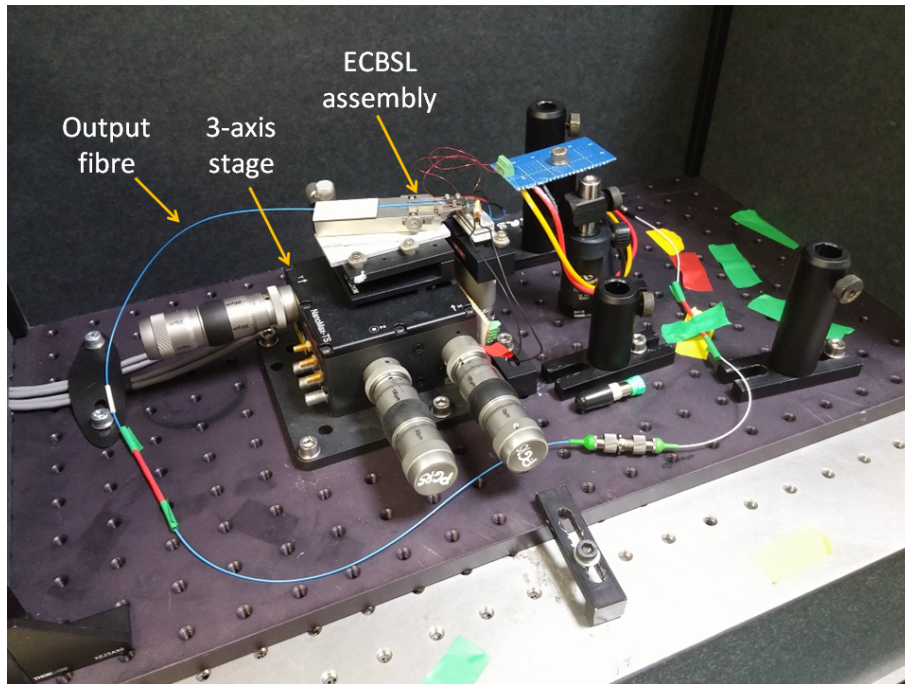
Figure 4.6: *Photograph of ECBSL in the laboratory, as received from University of Southampton.*
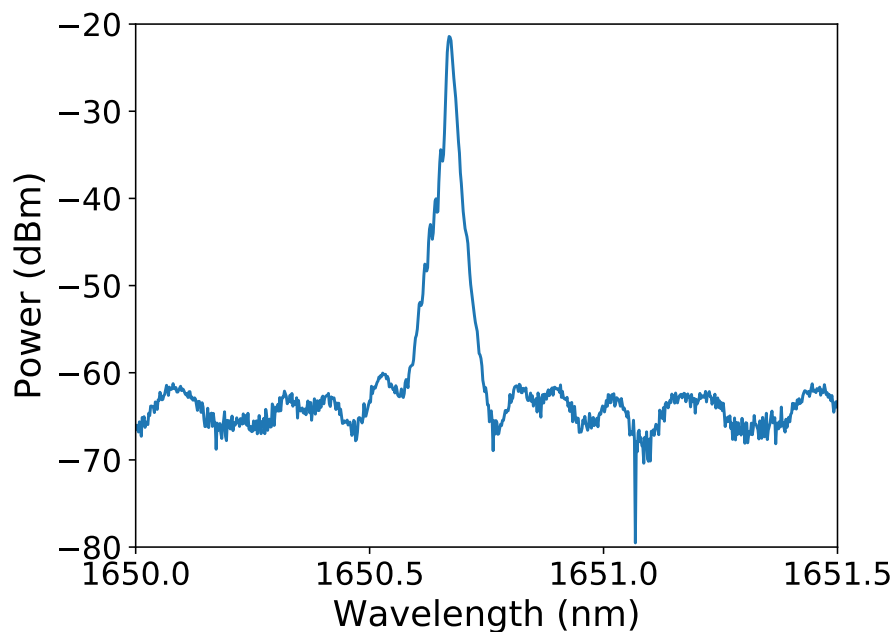
Figure 4.7: *Example of the output produced by the ECBSL, taken using an OSA.*

The heating element for the Bragg grating was controlled by a programmable voltage source (Keithley 230), with the gain chip temperature and current controlled by a laser diode controller (Stanford Research Systems model LDC502). It was found that

70

in this configuration, below current levels of 310mA and above 410mA the output of the laser would mode-hop, producing a sudden shift in wavelength. It was therefore required to operate the laser in this current range to avoid this issue.

To determine how the wavelength of the laser changes when the injection current is adjusted, the current was increased in steps of 5mA between 310mA and 410mA with the wavelength output recorded. Measurements of the laser output were taken using the OSA (with accuracy ±0.01nm). A graph showing the result of this can be observed in Figure 4.8.
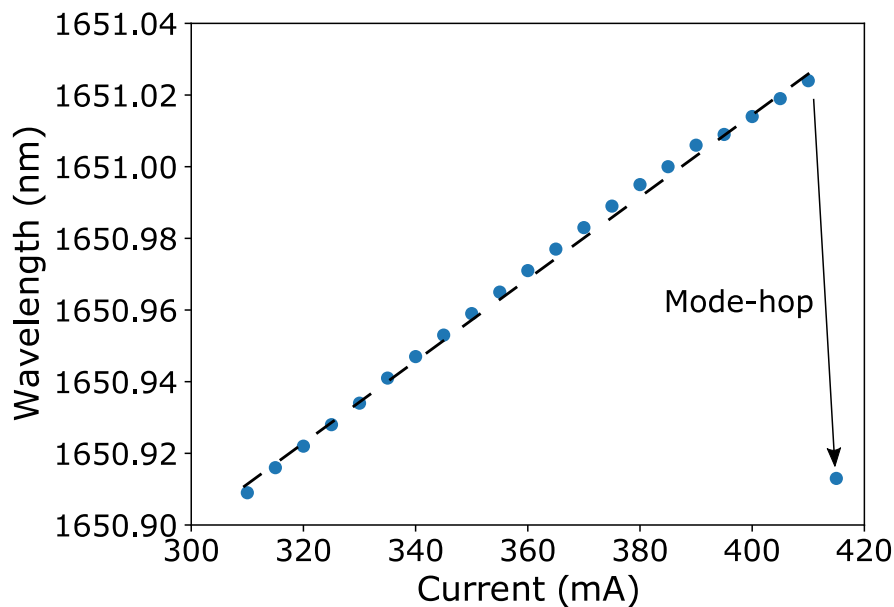
Figure 4.8: *Tuning Characteristics of the ECBSL. Points represent measured data, with the dashed line representing a linear trendline. An example of a mode-hop can be seen at 415mA.*

This tuning curve shows that the wavelength output of the laser increases by approximately 0.13nm when the injection current is changed between the lower and upper current limits, providing a tuning coefficient of 1.3×10^{-3}nm/mA. Although this wavelength range is relatively small, it is just large enough to take measurements of the 1651nm methane absorption line shown in Figure 4.1. Mode hop-free tuning of the ECBSL was observed at modulation frequencies of up to 10kHz, however the tuning range at this frequency is slightly reduced, essentially limiting the current

modulation to lower frequencies.

4.2.3   Methane detection with ECBSL

A line diagram of the experimental set-up used to detect methane using the ECBSL can be seen in Figure 4.9. To ensure that the tuning range of the laser was as large as possible, the laser emission was modulated with a sawtooth waveform at 80Hz using a USB oscilloscope (Picoscope 5444B). This was then directed through a 25cm single-pass gas cell with Brewster aligned windows. The beam was detected using a Thorlabs PDA400 amplified InGaAs detector, with the amplified signal collected using the Picoscope and PC.
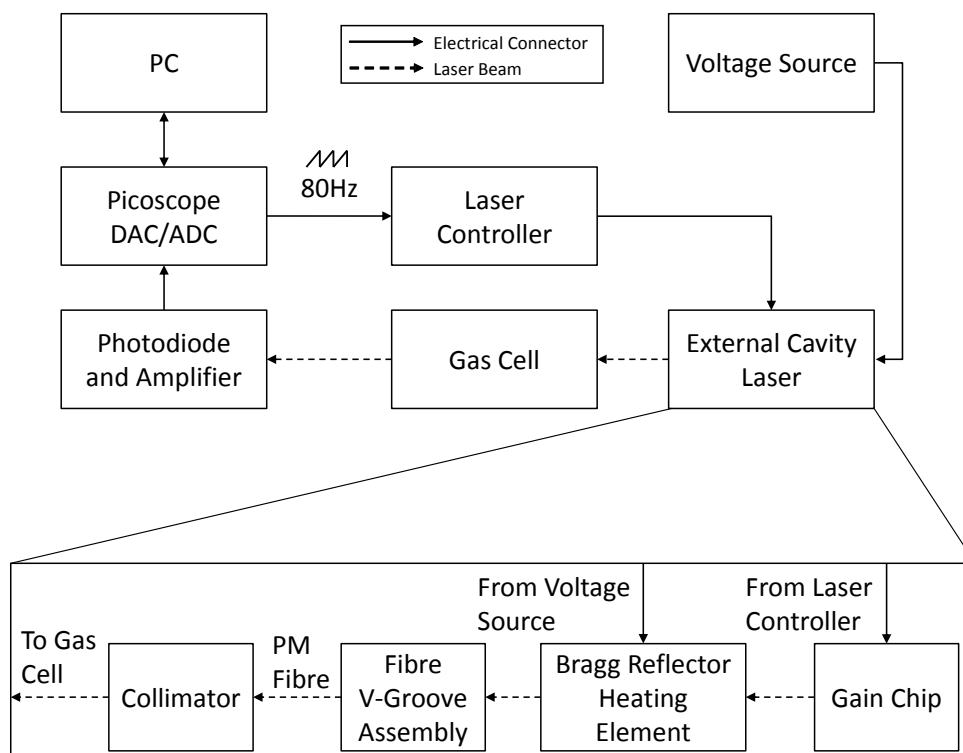
Figure 4.9: *Line diagram showing set-up used to evaluate suitability of ECBSL to detect methane.*

To control the flow of methane and air being fed to the gas cell, methane and synthetic air cylinders were connected up to a pair of mass flow controllers (Brooks Instrument model GF040CXX) regulated by a set point controller (Brooks Instrument 0254).

Initially, a 2.5% methane in air cylinder was utilised to more easily determine the correct current and temperature settings for the laser to align the absorption line with the centre of the waveform. A line diagram of the mass flow controller set-up can be observed in Figure 4.10.
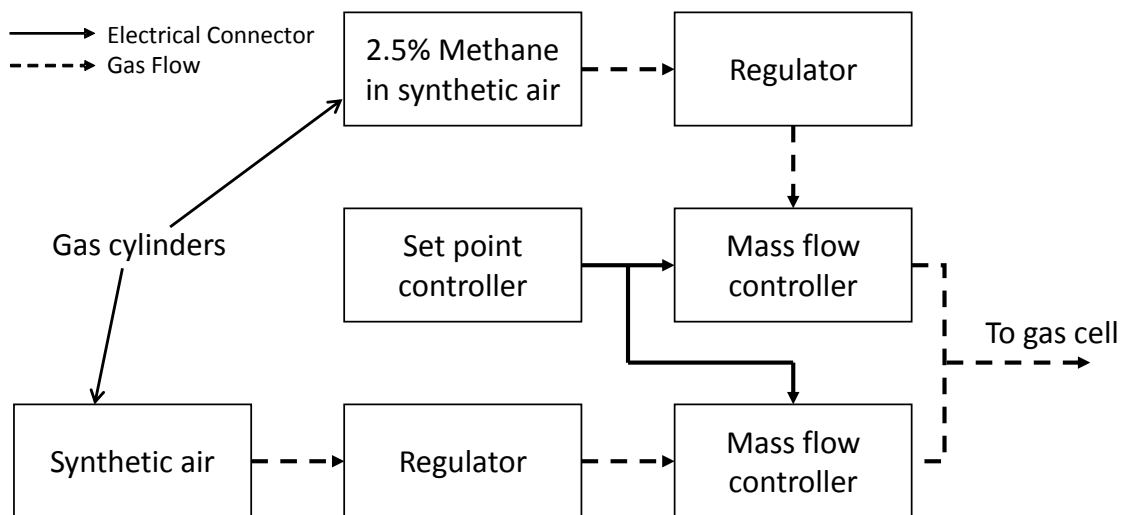
Figure 4.10: *Line diagram showing set-up of the mass flow controllers with gas cylinders containing 2.5% methane in air and synthetic air.*

Figure 4.11 shows a comparison between the raw data collected for a measurement of synthetic air and of a measurement of 2.5% methane in air. The graph shows the limitations of the tuning range of the laser, with the width of the absorption line only just covered by the laser modulation. Due to the absorption line being slightly off centre in this measurement, the 2.5% methane reading does not quite meet the baseline at the bottom of the curve. This can then be seen clearly in Figure 4.12 which displays the calculated absorbance for this measurement, following the process described in chapter 2, section 2.5.1. The wavelength scale of Figure 4.12 has been determined by comparing the measurement to the HITRAN absorption line in Figure 4.1.

By changing the flow rates from the cylinders, the concentration of methane in the gas cell could be adjusted. Using this technique, a range of concentrations were measured between 0 and 25000ppm. Measurements were averaged over a 1 second period so absorbance values for each measurement could be calculated, the results of

which can be seen in Figure 4.13. The graph shows that the absorbance has a linear relationship with the concentration of methane in the cell.
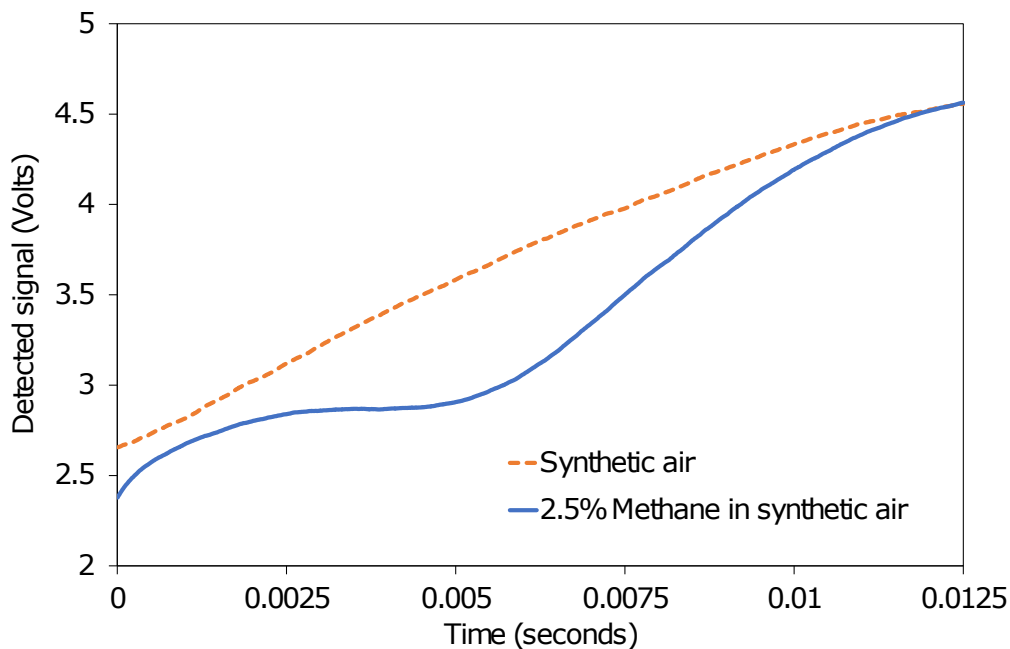
Figure 4.11: *Comparison between raw data collected for air and 2.5% methane using ECBSL.*
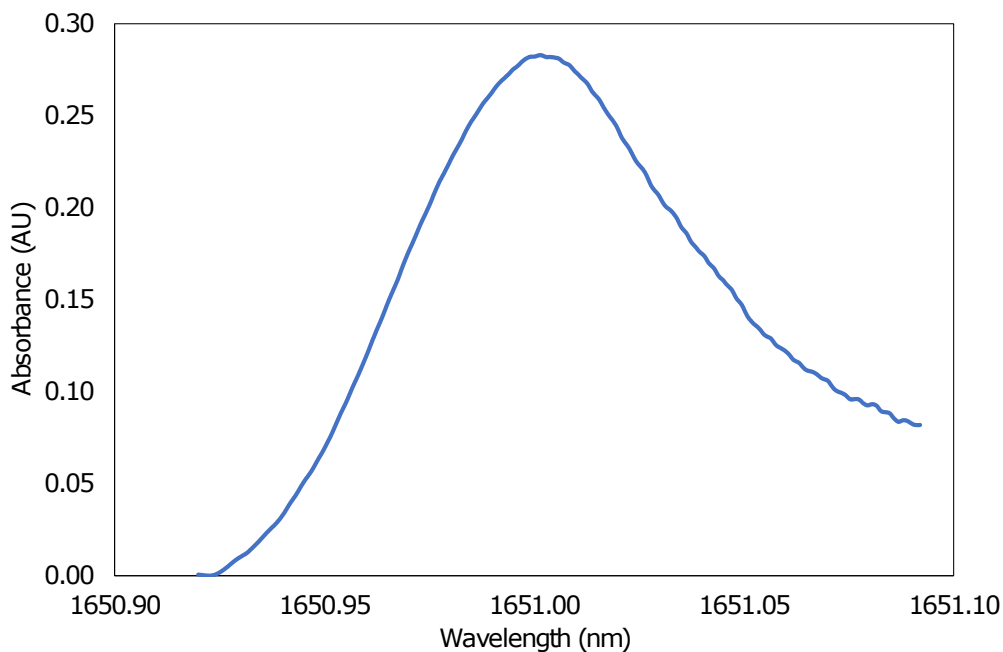
Figure 4.12: *Example of calculated absorbance for 2.5% methane concentration detected using ECBSL.*
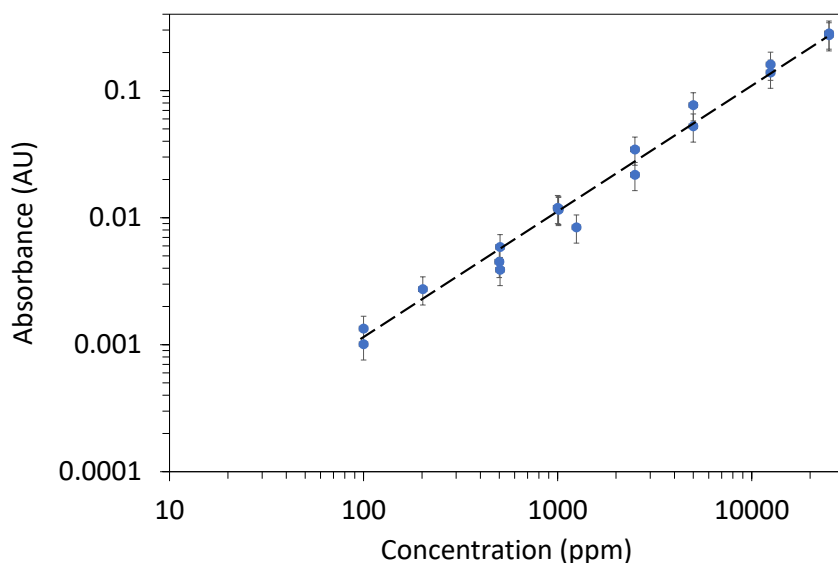
Figure 4.13: *Graph showing methane concentrations detected using the ECBSL against their respective absorbance strengths.*

It was found that the poor alignment stability of the laser affected the baseline readings that were being made (when attempting to take measurements below concentrations of 100ppm). This baseline drift prevented a clean measurement being made, restricting the concentration range that could be analysed. The effect of this can also be seen in Figure 4.13 with the large scatter in the data points around the linear fit. This scatter is likely attributable to fluctuations in the baseline and variations in flow rate from the mass flow controllers. The fluctuation in the baseline caused the absorbance calculations to produce values that did not necessarily correspond precisely to its respective methane concentration.

To see what limit of detection could be obtained if measurements could be taken at lower concentrations, a calculation of the noise equivalent absorbance (NEA, in AU) using this set-up was performed by performing a $\Delta I/I_0$ analysis using two synthetic air measurements. A standard deviation of 8.3×10^{-5}AU was calculated, and from this, a limit of detection could be calculated by comparing it to the peak absorbance at 100ppm, resulting in a single-point LOD of 8.3ppm.

4.3 Comparative analysis with DFB laser

To determine if the ECBSL performs within an acceptable operational range, a comparison with a conventional DFB fibre-coupled laser were performed, using as similar a set up as is possible to gain as close a comparison as possible. The DFB, a NEL NLK1U5EAAA 1651nm laser, was mounted in a Thorlabs LM14S2 butterfly laser mount (as shown in Figure 4.14) and was controlled by a Profile TED200 temperature controller and Profile LDC202 laser diode controller. Using the Yokogawa OSA to record the wavelength output of the laser, a current tuning curve for this laser was produced by increasing the injection current in 10mA steps between 10mA and 150mA, with the TEC set to operate the laser at 14.2kΩ (approximately 17.2°C). A graph showing the results of this can be seen in Figure 4.15.
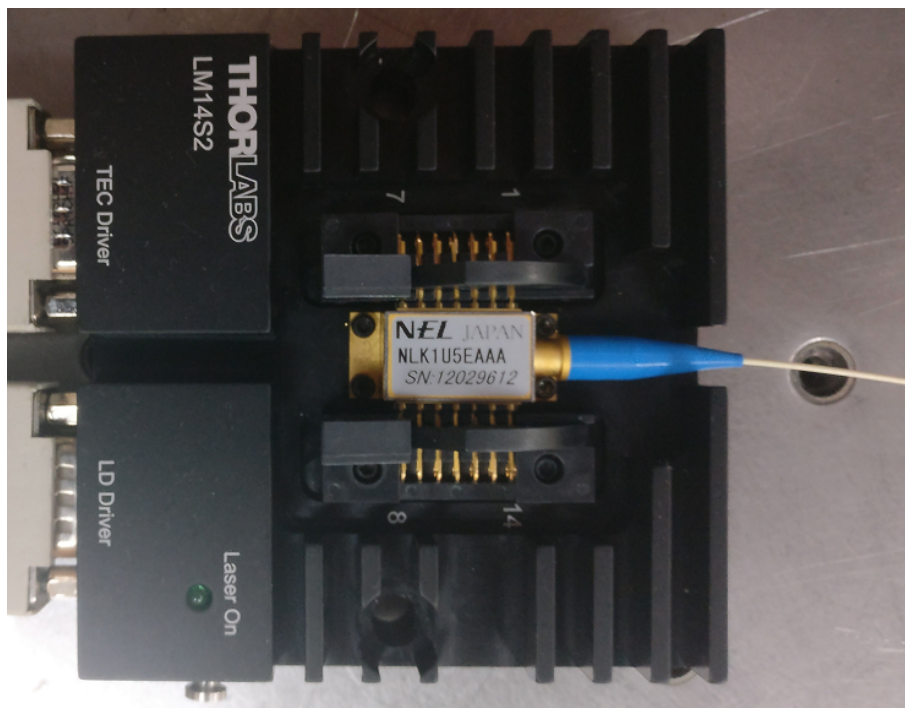
Figure 4.14: *DFB fibre-coupled laser mounted in a Thorlabs butterfly laser mount, as used in this section.*

The tuning curve shows some non-linearity compared with that seen with the ECBSL, however the tuning range of the DFB is significantly greater, 0.9nm instead of 0.12nm. This provides an average tuning coefficient of 6.4x10^{-3}nm/mA, which although is

not accurate due to the non-linearity seen, does provide a comparison against the ECBSL. Although the tuning range of the ECBSL is sufficient to measure a gas absorption line, the extra range of the DFB allows for adjustments to be made should the position of the gas line change in relation to the laser line.
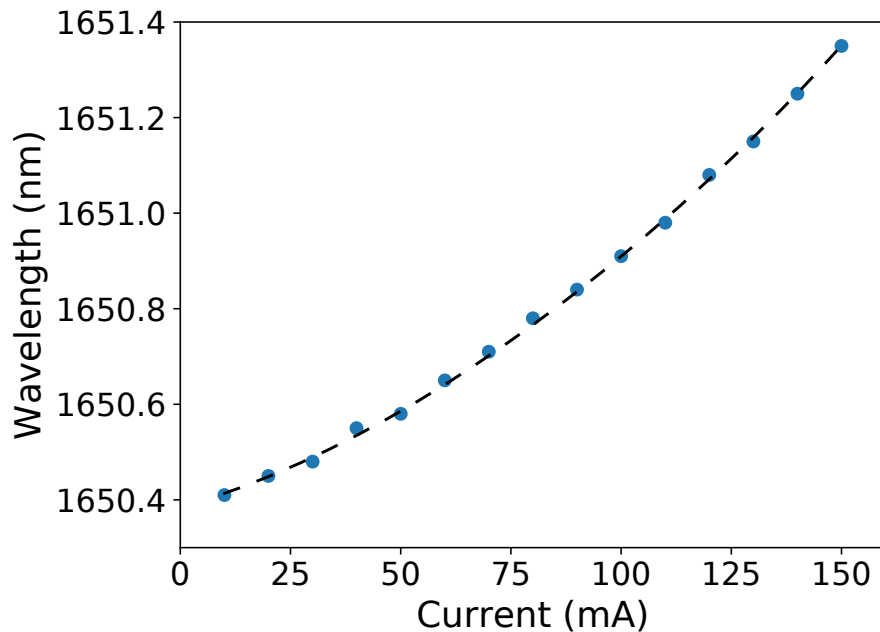
Figure 4.15: *Graph displaying how the wavelength output of a DFB fibre-coupled laser changes when the injection current is increased.*

Following this, the DFB laser was then aligned so that the output was collimated and directed through a 25cm single-pass absorption cell. The windows on this were aligned at the Brewster angle for this wavelength (54.95°), with the cell slowly rotated into a position such that any interference fringes present could no longer be observed. The wavelength of this laser was targeted at the same gas absorption line at 1651nm using current and temperature settings of 109.2mA and 14.215kΩ (17.2°C). The injection current of the DFB was modulated using a 1kHz triangle waveform with an amplitude of 0.5V. As before, the modulated laser beam was detected using a Thorlabs PDA400 amplified InGaAs detector and collected using the Picoscope and PC. A line diagram of this setup can be seen in Figure 4.16.
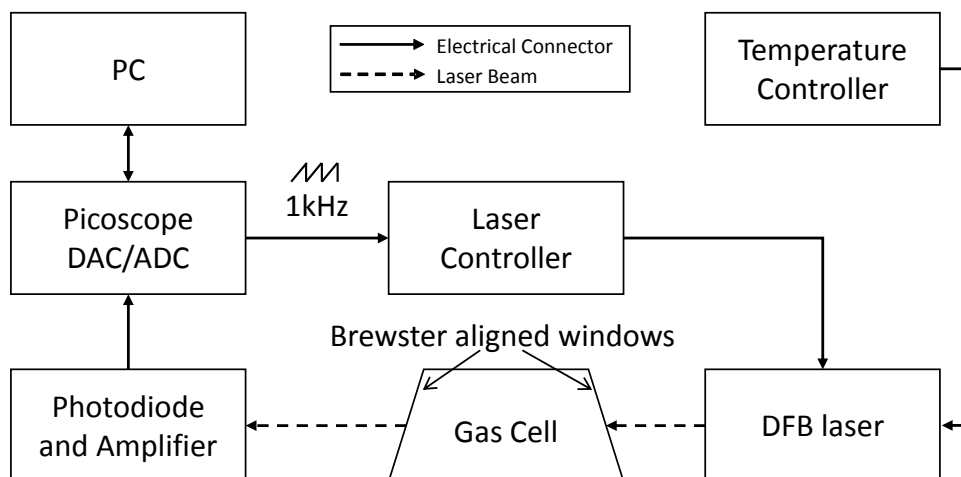
Figure 4.16: *Line diagram of set up used for methane detection with DFB laser.*

A 1010ppm methane in air cylinder was connected to the Brooks Instrument controller along with a synthetic air cylinder. The lower concentration cylinder was used for this part of the experiment as it was expected that the laser would be more stable than the ECBSL, due to its packaging, allowing for lower concentration measurements to more easily be taken. Preliminary measurements were taken at 1010ppm (as seen in Figure 4.17) and 500ppm to confirm that the laser was performing as expected. The calculated absorbance values were confirmed against the theoretical values obtained from the HITRAN database for the same concentrations and pathlengths. Due to the non-linear tuning curve seen in Figure 4.15, a non-linear wavelength scale was used to correct this, with the result verified against data from the HITRAN database.

Once it was confirmed that the DFB laser was operating normally, lower concentration measurements could be made. The concentration level was set to 200ppm and decreased in 10ppm increments down to 20ppm. Absorbance values were once again calculated for each measurement from the recorded data, the results of which can be seen in Figure 4.18. As with the ECBSL, the graph shows a linear relationship between the concentration of methane in the gas cell and the absorbance values calculated.
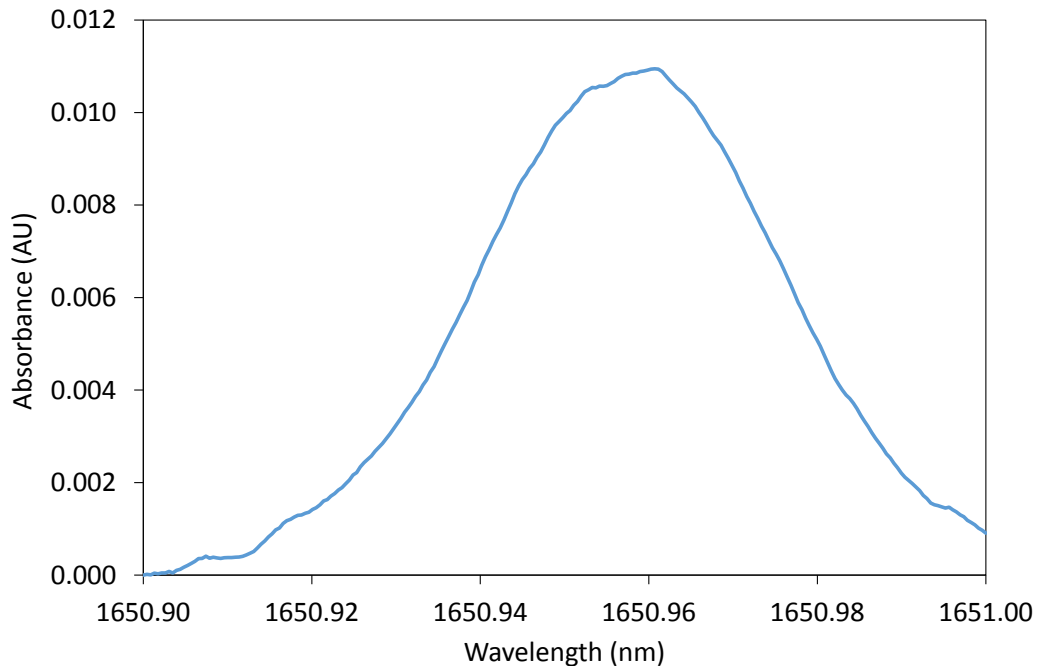
**Figure 4.17:** *Example of calculated absorbance for 1010ppm methane concentration detected using DFB fibre-coupled laser.*
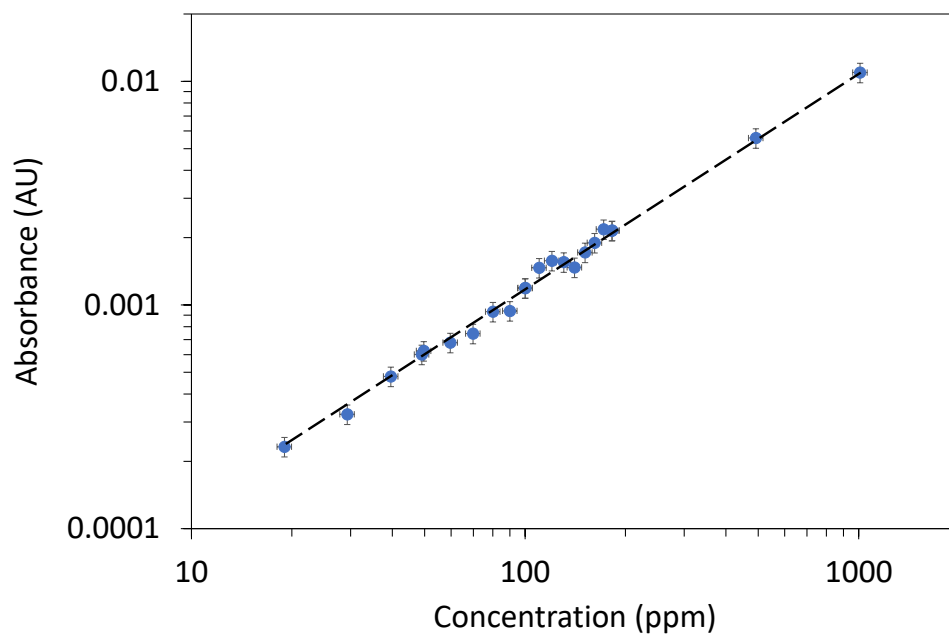
Figure 4.18: *Graph showing methane concentrations detected using the DFB laser against their respective absorbance strengths.*

A calculation of the NEA for this set-up was performed, resulting in a standard deviation of 8.26×10^{-5}AU. From this, a limit of detection could be calculated by comparing it to the absorbance strength at 100ppm. This resulted in a single-

point LOD of 8.26ppm. As the limits of detection for both lasers are very similar, this implies that the performance of both lasers were limited by the same factors, suggesting that the ECBSL could be effective for use in methane detection for short-term measurements. The larger scatter seen in the concentration measurements for the ECBSL show that it would be less suitable over longer-term measurements or outside of laboratory conditions.

4.4 Conclusions

In this chapter investigations were performed into the suitability of utilising a new external cavity Bragg-stabilised laser for use in methane detection, with comparisons made between this laser and a fibre-coupled DFB laser. The chapter summarises the background regarding the lasers that are available in the wavelength regime utilised. A description of the ECBSL was provided, showing the schematic of the laser along with its emission.

The tuning curves produced for each laser showed that the tuning range of the ECBSL is sufficient to cover the target methane absorption line, whereas the increased range of the DFB allows for measurements to continue even if the relative position of the absorption line changes.

It was found that alignment stability issues affected baseline readings and introduced drift when making measurements at low ppm level methane concentrations using the ECBSL. As a result, this limited the concentration range over which comparisons could be made. This can be seen in the concentration curve in Figure 4.13 as it was not possible to take reliable readings below 100ppm. The lack of stability of the laser also restricted the number of measurements that could be made at a time, as the gain chip and Bragg grating had to be realigned periodically due to mechanical drift.

It was found, however, that although the stability of the laser did restrict what measurements could be made, the single-point limit of detection for the ECBSL

was at a similar level to that of the DFB, 8.3ppm compared with 8.26ppm. It can therefore be inferred that the ECBSL could potentially be used in a gas detection system. It should be noted, however, that this is a short-term LOD, with the scatter on the data points in the ECBSL concentration curve implying a higher longer-term LOD. This is primarily affected by alignment sensitivity of the laser and could be solved through better packaging.

To summarise, it has been shown that a new form of external cavity Bragg-stabilised laser can be utilised to detect methane in a laboratory set up, showing comparable NEA and LOD to a fibre-coupled DFB laser. There are currently, however, a number of drawbacks with this ECBSL that limit its use. To improve the system, the laser needs to be mounted and packaged. This would reduce the issues observed with stability and drift.

In this current configuration, it would not be possible to utilise this laser for the purpose of detecting methane outside the laboratory, especially not on a light aircraft. As such, further investigations into alternative lasers will need to be undertaken to find one suitable for this project.

References

[1] Rothman, L., Gordon, I., Babikov, Y., Barbe, A., Chris Benner, D., Bernath, P., Birk, M., Bizzocchi, L., Boudon, V., Brown, L., Campargue, A., Chance, K., Cohen, E., Coudert, L., Devi, V., Drouin, B., Fayt, A., Flaud, J.-M., Gamache, R., Harrison, J., Hartmann, J.-M., Hill, C., Hodges, J., Jacquemart, D., Jolly, A., Lamouroux, J., Le Roy, R., Li, G., Long, D., Lyulin, O., Mackie, C., Massie, S., Mikhailenko, S., Müller, H., Naumenko, O., Nikitin, A., Orphal, J., Perevalov, V., Perrin, A., Polovtseva, E., Richard, C., Smith, M., Starikova, E., Sung, K., Tashkun, S., Tennyson, J., Toon, G., Tyuterev, V. and Wagner, G. (2013), "The HITRAN2012 molecular spectroscopic database," *Journal of Quantitative Spectroscopy and Radiative Transfer*, vol. 130, pp. 4–50.

[2] Ghafouri-Shiraz, H. (2003), *Distributed feedback laser diodes and optical tunable filters*, Wiley, Chichester, UK.

[3] RP Photonics Consulting GmbH, "Vertical Cavity Surface-emitting Lasers," https://www.rp-photonics.com/vertical_cavity_surface_emitting_lasers.html, Date Accessed: 11/12/2017.

[4] Zorabedian, P. (1995), "Tunable External-Cavity Semiconductor Lasers," in: Duarte, F. J. (editor), "Tunable Lasers Handbook," chap. 8, Academic Press.

[5] Ricci, L., Weidemüller, M., Esslinger, T., Hemmerich, A., Zimmermann, C., Vuletic, V., König, W. and Hänsch, T. W. (1995), "A compact grating-stabilized diode laser system for atomic physics," *Optics Communications*, vol. 117, no. 5-6, pp. 541–549.

[6] Littman, M. G. and Metcalf, H. J. (1978), "Spectrally narrow pulsed dye laser without beam expander." *Applied Optics*, vol. 17, no. 14, pp. 2224–2227.

[7] Hodgkinson, J. and Tatam, R. P. (2013), "Optical gas sensing: a review," *Measurement Science and Technology*, vol. 24, no. 1, p. 012004 (59 pages).

[8] Lynch, S. G., Gates, J. C., Berry, S. A., Holmes, C. and Smith, P. G. R. (2015), "Thermally tunable integrated planar Bragg-grating stabilized diode laser," *Proceedings of SPIE - Novel In-Plane Semiconductor Lasers XIV*, vol. 9382, p. 93820O.

[9] Lynch, S. G. (2017), *Integrated planar cavities for external cavity diode lasers*, Ph.D. thesis, Southampton University, Southampton.

[10] Thorlabs Inc., "1620 nm External Cavity Single-Frequency Laser Diode," https://www.thorlabs.de/newgrouppage9.cfm?objectgroup_id=4934, Date Accessed: 28/01/2018.

Chapter 5

Mid infrared tunable diode laser spectroscopy of methane

Initial work using a new external cavity Bragg stabilised laser was demonstrated in Chapter 4, along with comparisons made against a standard DFB fibre-coupled laser. Although this laser showed promise for potential use in gas sensing, it is not yet a viable solution for this project in its current state. As such, alternative lasers would need to be utilised to make further progress. In this chapter, work undertaken using an interband cascade laser in the mid infrared is presented. Characterisation of the laser is performed along with an analysis of its performance using both a standard single-pass cell and an integrating sphere.

5.1   Mid infrared lasers

Up until relatively recently, the choice of laser for use in the mid infrared was limited to a few DFB laser diodes, difference frequency generation (DFG) lasers, and quantum cascade lasers (QCLs). More recently, interband cascade lasers (ICLs) have been made commercially available to provide an additional means of operating in this wavelength region. DFB lasers were covered at the start of the previous chapter, the remaining options will be covered in the following sections.

5.1.1   Difference frequency generation lasers

DFG lasers sources consist of two seed lasers sources (a signal and laser pump source) combined and focussed into a non-linear optical medium to generate an idler output at the difference frequency between the two [1]. DFGs utilise an optical crystal with a high non-linearity coefficient that is transparent in the desired wavelength range to achieve wide, mode-hop free tuning.

One of the main limitations regarding the output power of DFG sources is the damage threshold of the crystal. Even so, output powers of up to tens of mW can be achieved with these lasers [2]. To achieve a wide tuning range in the mid IR, DFG sources require a widely tunable near IR seed source. As discussed in the previous chapter, there are numerous options in the 1500-1600nm near IR telecoms band.

There are, however, a number of limitations with using DFG lasers. The main issue is that when operating the crystal needs to be realigned periodically. DFG systems are also often significantly larger than other discrete laser devices, severely limiting their use in field applications. Although progress has been made in improving their reliability and field robustness through the use of optical fibre, Richter *et al* have shown that performance drops by approximately a factor of 10 compared with laboratory measurements [1].

5.1.2   Quantum cascade lasers

Quantum cascade lasers (QCLs) operate through the use of a series of quantum well structures. Artificial energy levels are created using these structures, providing transitions independent of the material bandgap. As each electron passes through the cascade structure, photons are emitted. As with semiconductor laser diodes, QCLs use DFB structures to ensure singlemode emission. Current QCLs are commercially available from around 4μm to 15μm and potentially beyond. This in turn means that QCLs are available that can target the methane absorption lines at 7.8μm, but not at 3.3μm.

QCLs have been widely produced in both pulsed and continuous wave forms, providing potential power levels significantly higher than alternative lasers. This makes them suitable for use in applications using photoacoustic or backscatter detection, however does mean that increased thermal management is needed to dissipate the additional heat generated.

5.1.3   Interband cascade lasers

ICLs fill an important gap between the wavelengths available using standard DFB laser diodes and QCLs, being commercially available in the 3-6μm range. This is significant as there are numerous fundamental absorption bands in this wavelength region. Output powers for these lasers are of the order of one to tens of mW. Physically, ICLs can be considered to be a hybrid of both conventional laser diodes and QCLs. A diagram showing the well structures of all three can be observed in Figure 5.1. Both pulsed and continuous wave versions are commercially available, with DFB structures utilised to provide mode-hop free, singlemode operation [3].

ICLs provide an enticing compromise between the wavelength operation range of the DFG lasers and the usability of QCLs, without having the drawbacks of being oversized or needing additional thermal management. As a result of this, it was decided to utilise an ICL for use with this project.

5.2   Characterisation of ICL

The laser, as shown in Figure 5.2, that was chosen for use with this project was an ICL (Nanoplus) operating at a typical wavelength of 3311.3nm and output power of 2.3mW. At the time of purchase, these lasers were new to the market, with the choice of wavelength being limited. This wavelength was chosen due to its proximity to both a strong methane absorption line at 3313nm and a water absorption line at 3308.5nm. As is noted later on in Section 5.4, the methane absorption feature at this wavelength is complex, meaning that a tuning range of at least 1nm was required to provide reliable results.
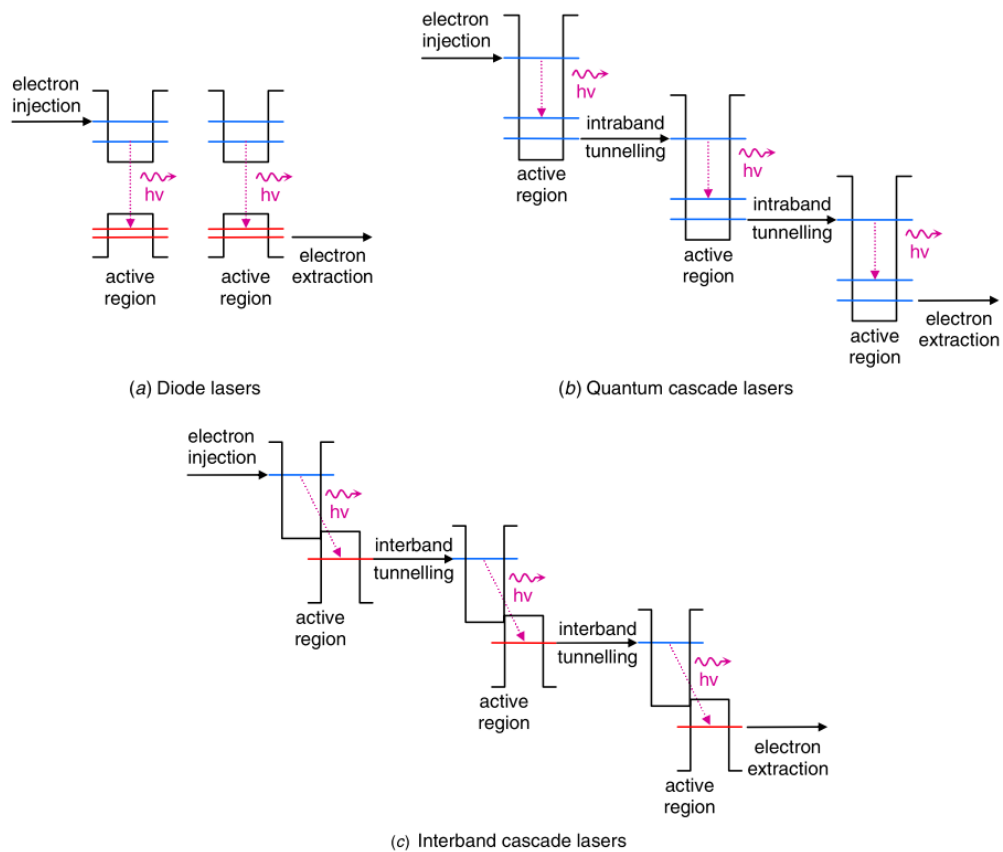
Figure 5.1: *Comparison of energy levels and active region processes for laser diodes, QCLs and ICLs, taken from [3].*

Figure 5.2: *Picture of 3311.3nm ICL in Laboratory. The laser is packaged within a large heatsink and collimation optics.*

5.2.1   Initial set-up

To operate the laser, a combination current and temperature controller (Stanford Research Systems LDC502) was connected. To ensure that the laser was operating correctly, the laser output was directed at a mid infrared OSA (Yokogawa AQ6376, on loan from DM Optics Limited) to check the emission spectrum. Using the typical values of 30.0°C and 37.0mA as stated in the laser datasheet, the emission spectrum shown in Figure 5.3 could be acquired. Taking into account that the laser was potentially not aligned perfectly with the OSA, the emission observed appears to match the expected spectrum shown in the laser datasheet, as seen in Appendix A.
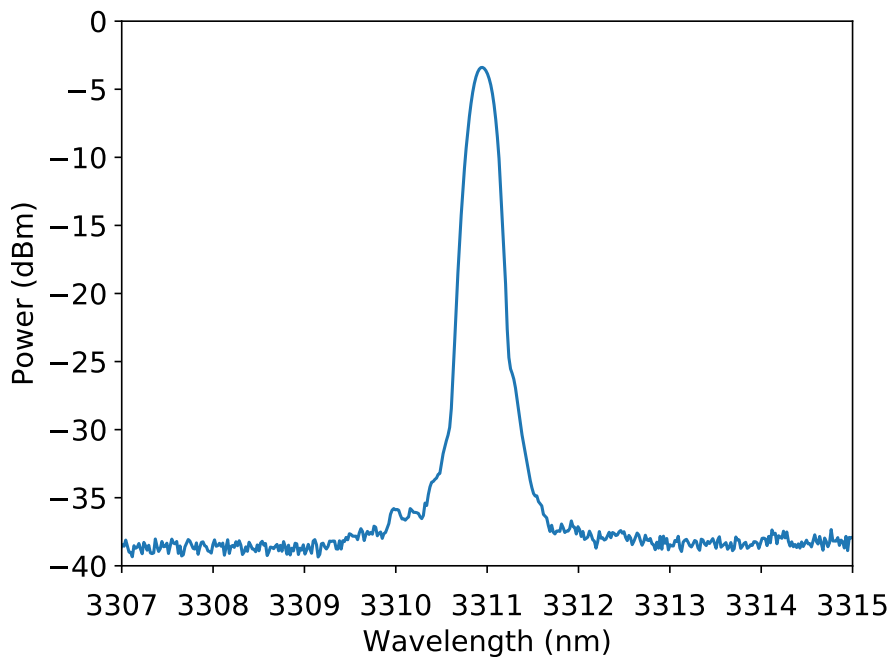
Figure 5.3: *Emission spectrum of 3311nm ICL at typical values of 30.0°C and 37mA, measured with an OSA (Yokogawa AQ6376) with a resolution of 0.1nm.*

Whilst aligned with the OSA, the injection current was gradually increased from just below the threshold current (18mA) to the max current rating (45mA) with the temperature still set at 30.0°C. This provided a current tuning curve for the laser, as shown in Figure 5.4. From this graph, a tuning coefficient of 0.166 nm/mA could be calculated for the ICL.
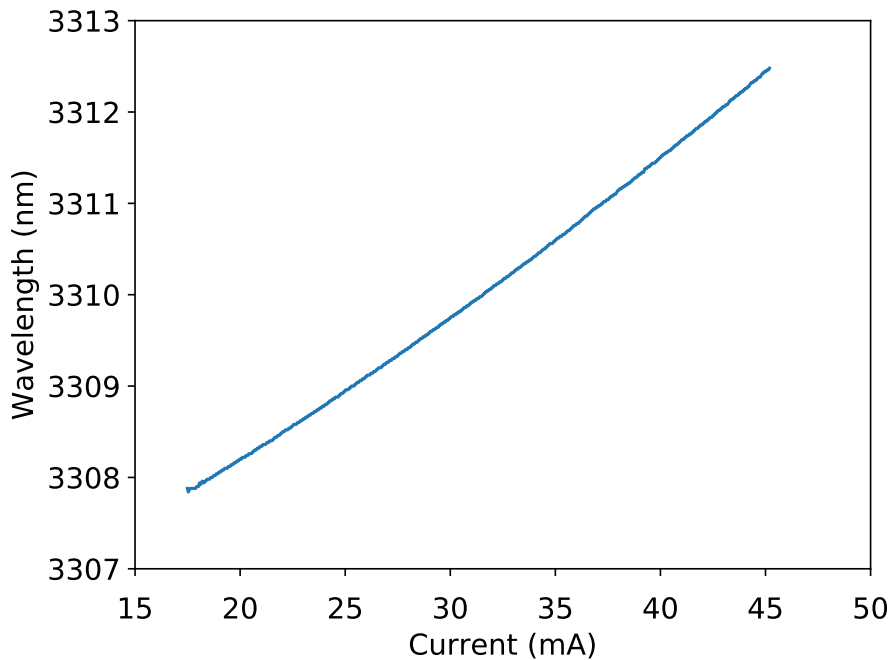
Figure 5.4: *peak emission wavelength vs current of 3311nm ICL at 30.0°C, taken using Yokogawa AQ6376 OSA.*

Once the output characteristics of the laser were confirmed, the laser emission was aligned with a lensed mercury cadmium telluride (MCT) detector (VIGO PVI-2TE-5), with the output amplified using a variable gain transimpedance amplifier (Femto DLPCA-200). A function generator (Stanford Research Systems DS345) was connected to the laser controller to modulate the laser emission.

5.2.2   Modulation curvature analysis

It was noted when performing an initial ramp modulation (5Hz, 0.1Vpp amplitude) with the laser, there was a significant curvature in the detected signal, as seen in Figure 5.5. As the tuning curve for the laser appears approximately linear, it was thought that the detector may be responsible. To confirm this hypothesis, comparisons were made between the ICL and a blackbody source (Heitronics SW11B and SR11C).
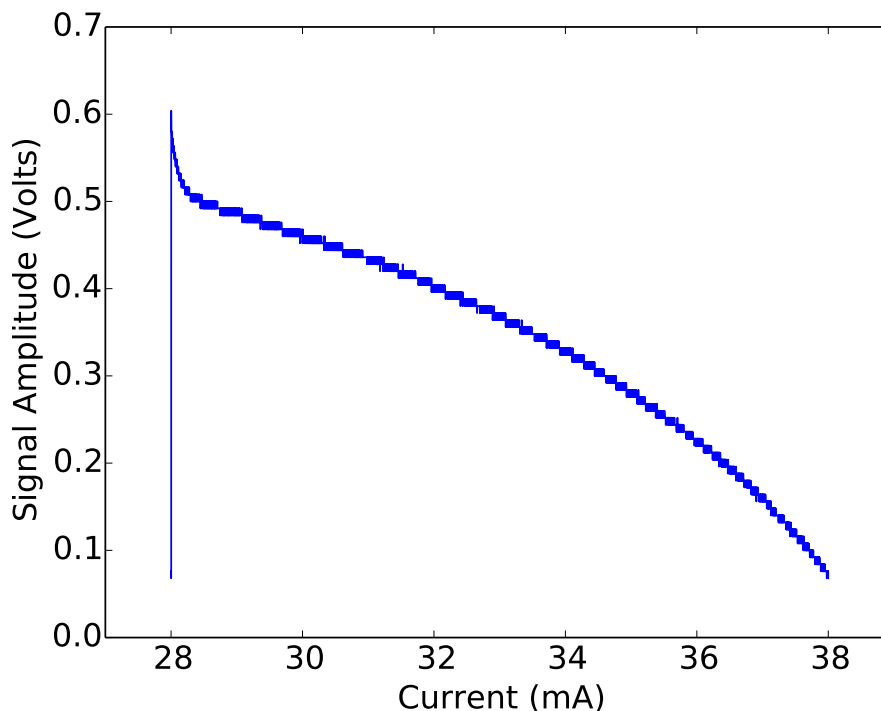
Figure 5.5: *Modulation curvature observed when initially modulating the ICL at 5Hz with a sawtooth waveform.*

The detector was positioned in front of the blackbody source, with a chopper wheel (Scitec Instruments 300CD) placed between them. The source was then set to operate at 400°C and the chopper wheel at 20Hz, with measurements from the detector and amplifier monitored and taken using an oscilloscope (Tektronix DPO 2014). The detector and chopper wheel were then positioned in front of the ICL and measurements were similarly taken with the ICL operating at 40mA and 30°C. These measurements can be seen in Figures 5.6 and 5.7.

The use of a chopper on the blackbody source and ICL should produce either a regular square or trapezium wave, depending on the ratio of the beam width to the chopper blade width. What is seen, however, is that although the transition between signal and no signal is well defined, the top and bottom of the square wave for each signal is significantly slanted. As both of the signals are affected in the same way, it suggests that the cause of the curvature seen previously is caused by the detector.
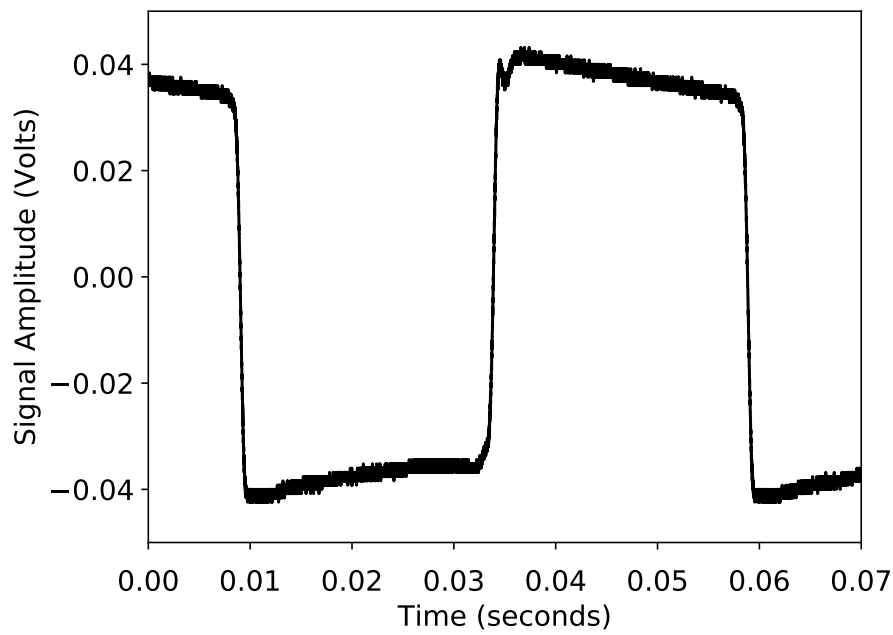
Figure 5.6: *Signal recorded by detector from Blackbody source at 400°C, modulated at 20Hz using a chopper wheel.*
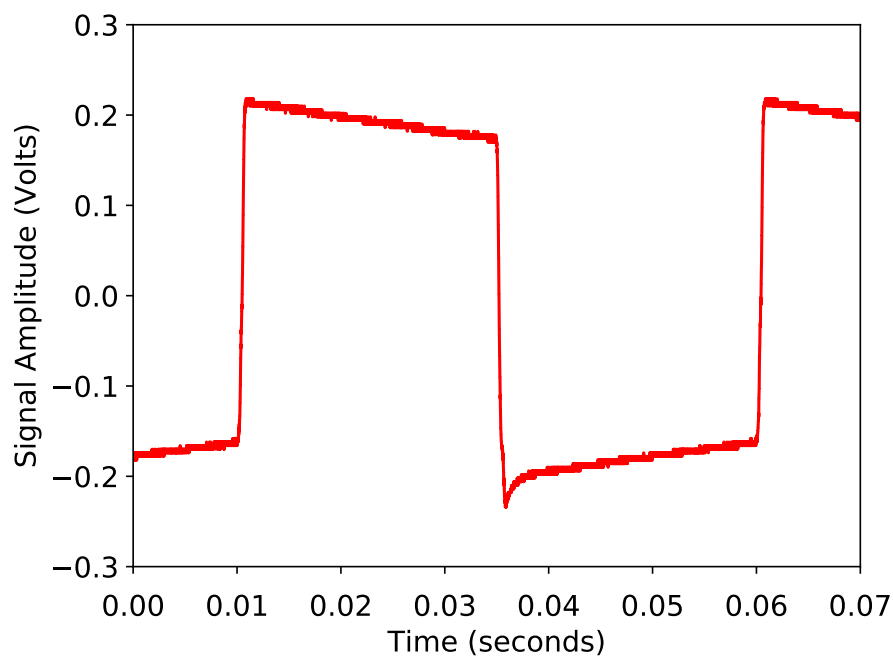
Figure 5.7: *ICL at 40mA and 30°C, modulated at 20Hz using a chopper wheel.*

To investigate further, the rotation frequency of the chopper wheel was increased from 20Hz to 75Hz. As shown in Figures 5.8 and 5.9, it was seen that the higher frequency modulation decreased the severity of the slope. Although at this frequency

91

the slope has not been entirely removed, it has definitely been reduced.
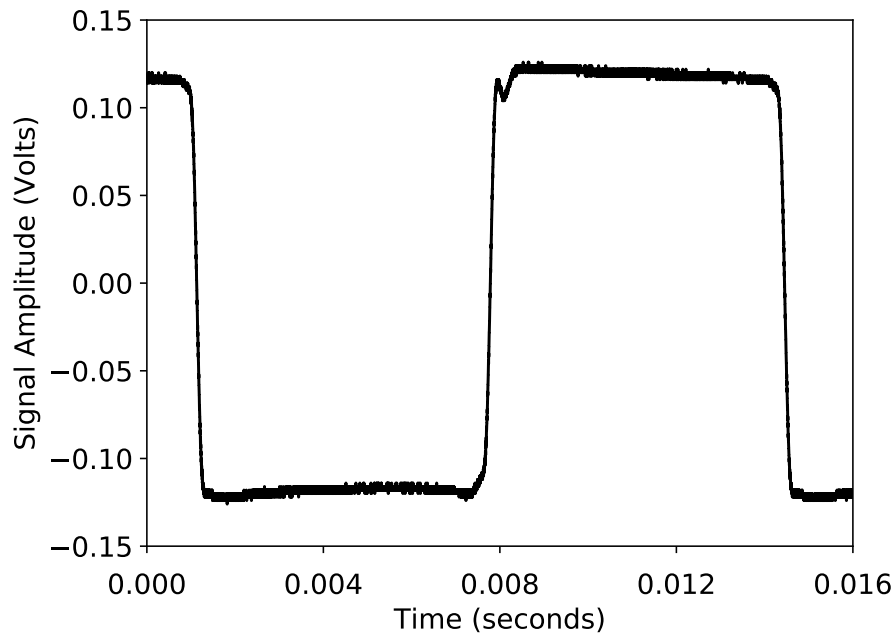
Figure 5.8: *Blackbody source at 400° C, modulated at 75Hz using a chopper wheel.*
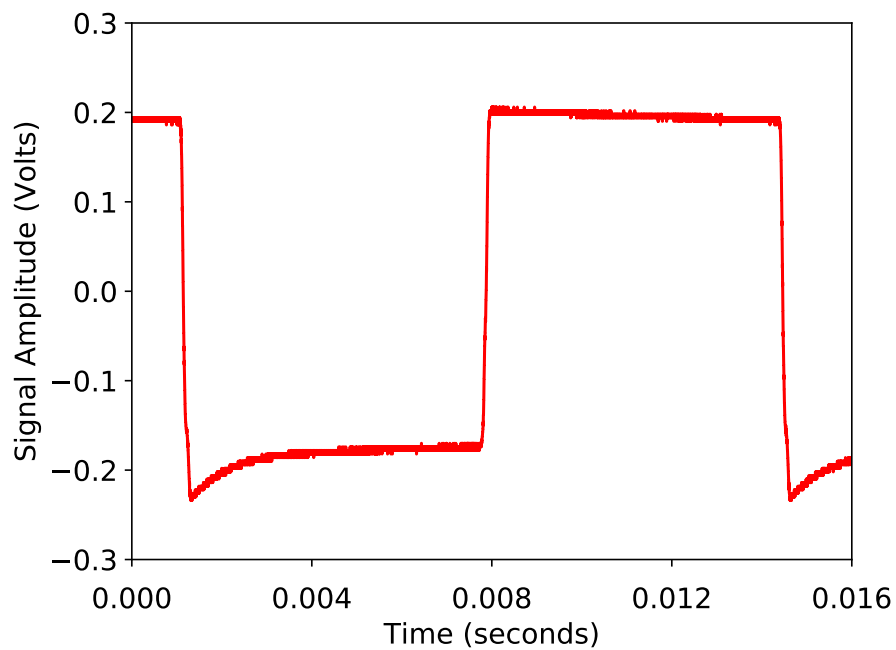
Figure 5.9: *ICL at 40mA and 30° C, modulated at 75Hz using a chopper wheel.*

Using this knowledge, it was concluded that the ICL should be modulated at a higher frequency to remove the modulation curvature. The detector was realigned with the ICL and a 100Hz ramp modulation frequency was applied to the injection current of the laser, as shown in Figure 5.10. It can be seen that, as before, the distortion is significantly reduced at this higher frequency, however it has still not disappeared completely. The frequency was then increased up to 1kHz, as seen in Figure 5.11. This figure shows that, with the exception of a small curve at the bottom of the ramp, the distortion on the signal is now removed. As a result of this, it was decided that the ICL should be modulated at this frequency in future usage.

5.3 Analysis of noise

With the curvature of the detected output signal explained, with a solution to reduce its severity determined, an analysis of the system noise could commence. During previous use, it was noted that the output of the function generator (HP 33120A) was not entirely stable, occasionally fluctuating in the time domain. This was therefore replaced by a digital to analogue converter (DAC) and data acquisition card, controlled through Labview (The control code can be viewed in Appendix B).

With the new DAC in place, a 30 second average was taken of the detected signal and was subtracted from an individual sawtooth to determine how respectable the signal is. It was noted upon analysis that a period structure was present in the signal, as shown in Figure 5.12. The current has been converted to wavelength in these plots using the tuning curve produced in Figure 5.4.
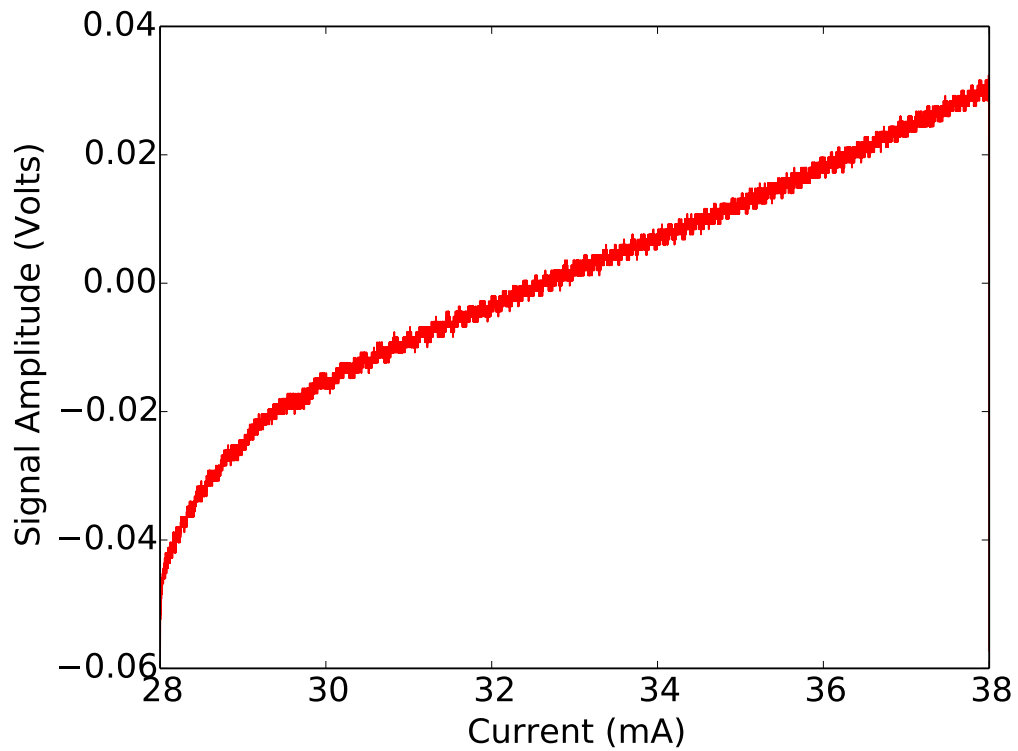
Figure 5.10: *Modulation of ICL using a 100Hz sawtooth waveform.*
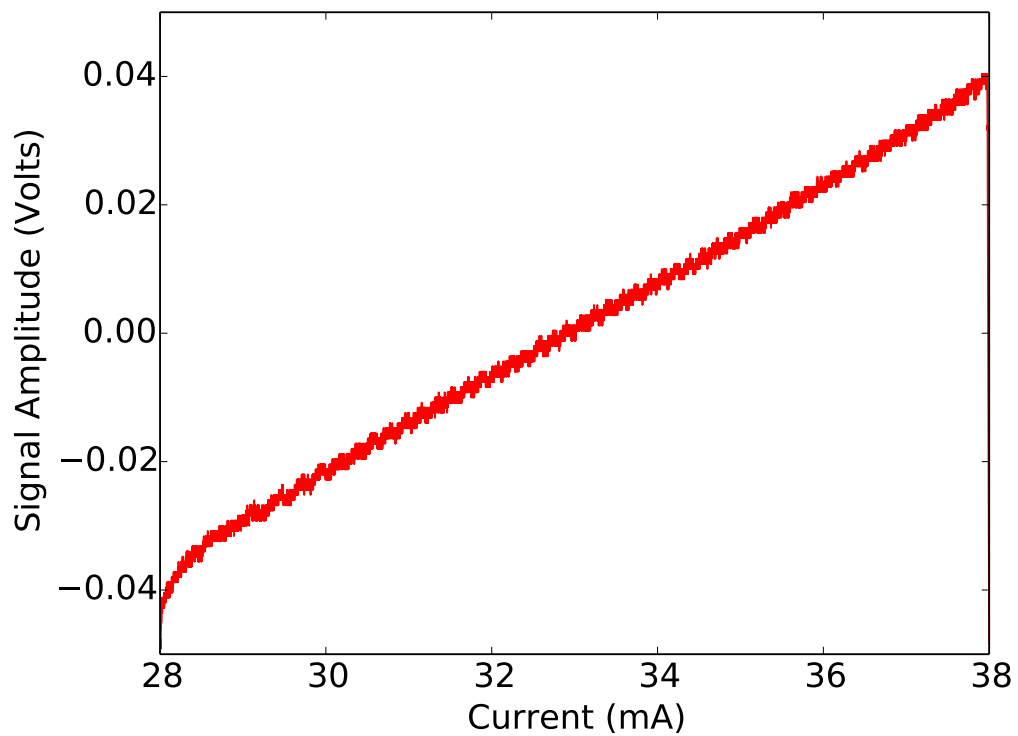
Figure 5.11: *Modulation of ICL using a 1kHz sawtooth waveform.*
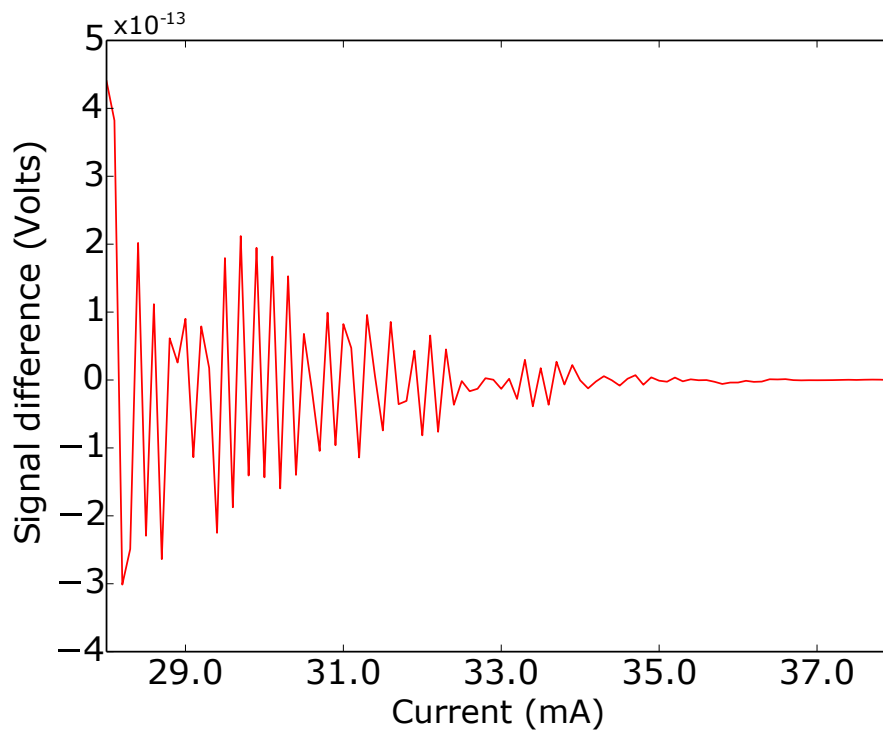
Figure 5.12: *Individual detected ramp signal subtracted from averaged signal with VIGO detector.*

It was thought that this could possibly be attributed to an interference effect introduced by the lensed detector. To confirm this, and potentially reduce the interference fringes, the detector was replaced by an unlensed MCT detector (Hamamatsu P3981) mounted in a heatsink (Hamamatsu A3179). A comparison between the different detectors can be seen in Table 5.1.

Table 5.1: *Comparison between VIGO and Hamamatsu detectors.*

Parameter	VIGO PVI-2TE-5	Hamamatsu P3981
Lensed	Yes	No
Wavelength range	2.5μm - 5.1μm	2.0μm - 4.3μm
Detectivity	1×10^{11} cm·Hz$^{1/2}$/W	5×10^{10} cm·Hz$^{1/2}$/W
NEP	1×10^{-12} W/Hz$^{1/2}$	2×10^{-12} W/Hz$^{1/2}$
Rise time (τ_R)	80ns	10μs
Bandwidth ($\approx 0.35/\tau_R$)	4.375MHz	35kHz

The detector was angled at the Brewster angle (54.76°) to reduce any back-reflection from the detector windows, before the previous process was repeated, with the

outcome shown in Figure 5.13. The fringes appear to have now been removed, with the scale of the signal approximately a factor of ten smaller than that seen previously. This suggests that the signal is no longer limited by the interference fringes, but rather the background detector noise.

To provide a more accurate representation of the noise of each component, a network signal analyser (SRS SR780) was used. An initial measurement of the background noise on the analyser was taken by connecting a shorted out BNC connector to the input. This provided a background reading, as shown in Figure 5.14, with a floor value of 8.0×10^{-9} VHz$^{-1/2}$.
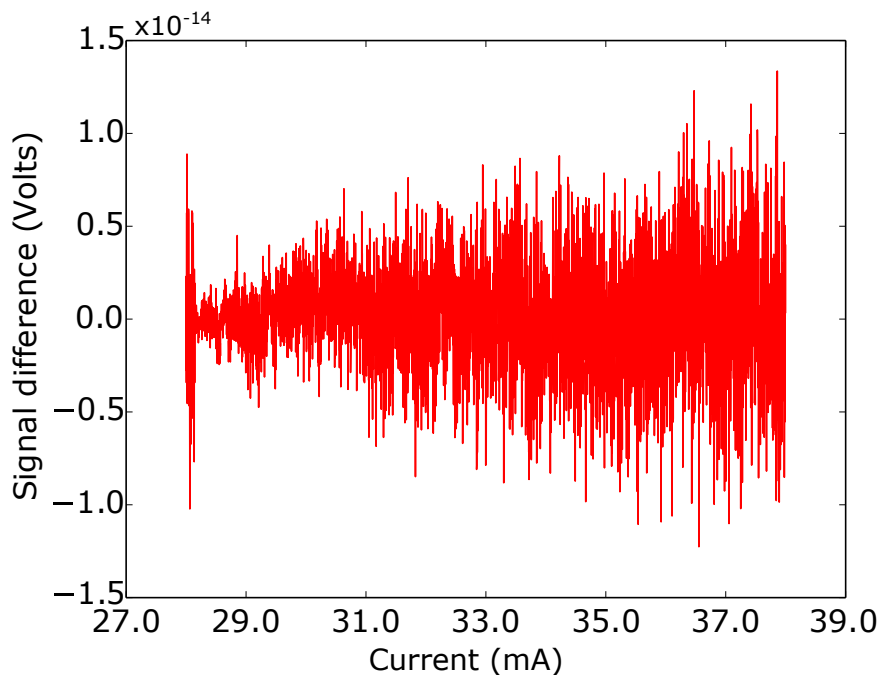
Figure 5.13: *Individual detected ramp signal subtracted from averaged signal with Hamamatsu detector.*

To ensure that the detector was operating with the lowest possible noise level, it was cooled through the use of a temperature controller (Graseby Infrared model TC-328). A target thermistor resistance was set on the controller, causing a current to be applied to the detector peltier. This resistance value was gradually increased until a runaway thermal effect was caused in the detector. This manifests itself as a continually increasing current being applied to the detector. The thermistor

value was then set just below this level at 7.3kΩ (-20°C) to provide stable operating conditions.

The signal analyser was then connected directly to the detector and amplifier, with a gain setting of $1\text{x}10^5$ V/A. With no light incident upon it, a measurement of the detector noise could be made, providing a floor value of $1.8\text{x}10^{-6}$ VHz$^{-1/2}$. Following this, the ICL was aligned directly with the detector and set to emit using the typical settings (30°C and 37mA). The output from the detector was recorded as the laser noise, providing a reading of $2.2\text{x}10^{-6}$ VHz$^{-1/2}$. An adaptor was then placed on the current control input for the laser that could measure the noise across a 100Ω resistor connected to the injection current pin in order to measure the noise on the drive current. This provided a value of $1.5\text{x}10^{-9}$ AHz$^{-1/2}$.

These could then be converted into AU by dividing through by the signal strength (current or voltage depending on the value) before multiplying by the square root of the noise equivalent bandwidth (NEBW) for the system. The NEBW was calculated using Equation 5.1 [4], where N_S is the number of recorded signals in the averaging time (1 second) and τ_B is the time of each recorded data point (10μs), providing a value of 50Hz.

$$NEBW = N_S \frac{1}{4\tau_B} \qquad (5.1)$$

Table 5.2 displays the individual noise values (with their respective AU equivalents) for each component in descending order. This shows that the limiting factor in terms of noise in the system will either be the laser or the detector, depending on the set-up used. At high intensities the laser noise will dominate, with the detector likely dominating at lower intensities.
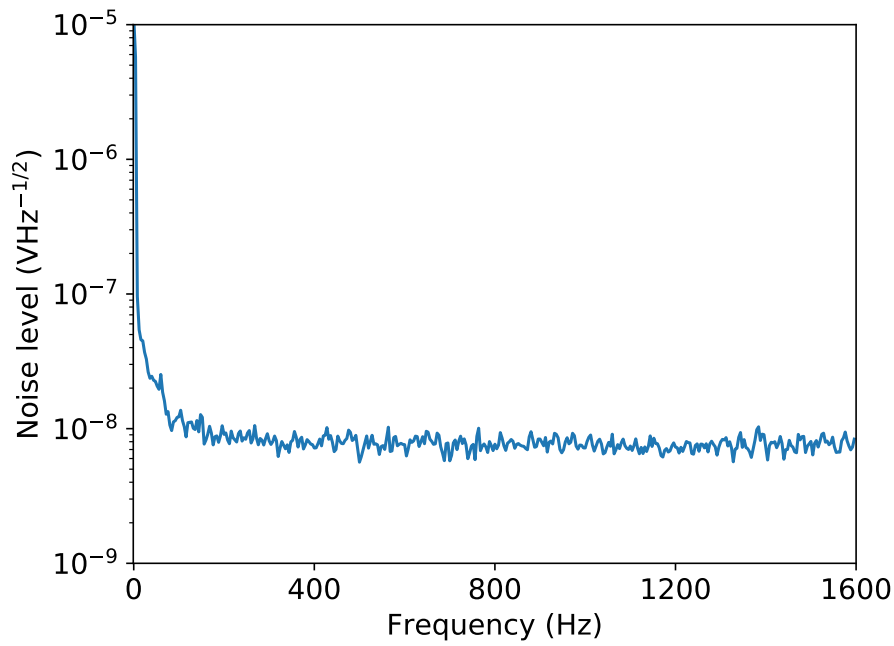
Figure 5.14: *Background noise levels detected using network signal analyser.*

Table 5.2: *Individual noise values for components in set-up.*

Noise Source	Level	Equivalent level in AU
Laser on	2.2×10^{-6} VHz$^{-1/2}$	1.5×10^{-3} AU
Detector only	1.8×10^{-6} VHz$^{-1/2}$	1.3×10^{-3} AU
Injection current	1.5×10^{-9} AHz$^{-1/2}$	2.7×10^{-7} AU
Background	8.5×10^{-9} VHz$^{-1/2}$	6.0×10^{-6} AU

5.4   Methane Detection

The methane line to be targeted by the following experimental procedures can be observed in Figure 5.15. This absorption feature is a combination of approximately six individual absorption lines, giving it its distinctive shape.
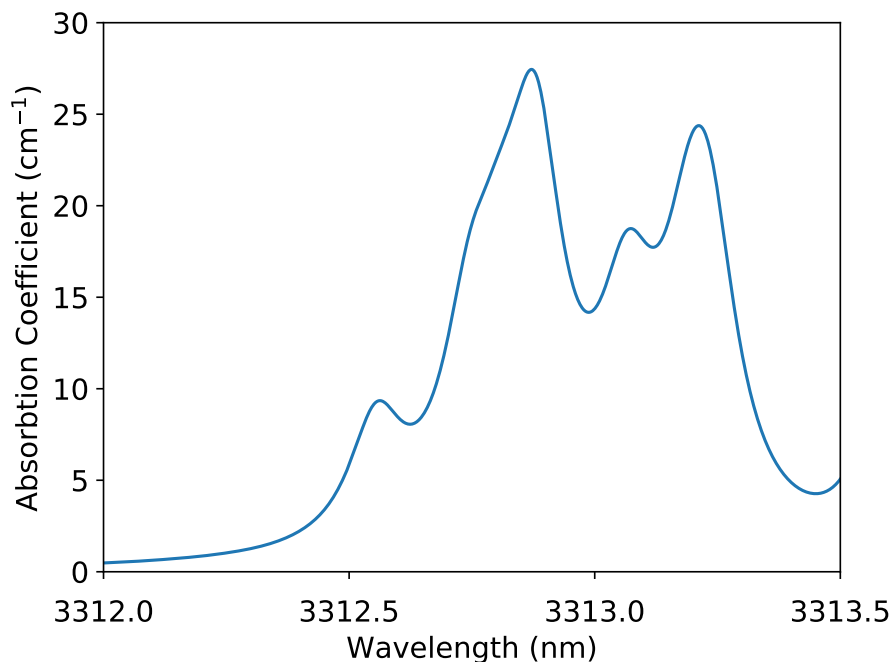
Figure 5.15: *100% methane absorption line centred around 3313nm, calculated from the HITRAN database [5].*

5.4.1   Single-pass gas cell

To enable initial measurements of methane to take place, a single-pass 25cm gas cell was produced. Calcium fluoride, CaF_2, windows were aligned at the Brewster angle at each end of the cell. The cell was then gradually rotated so that the alignment of the windows corresponded to the polarisation state of the laser, as described in the datasheet in Appendix A, to prevent interference fringes from being generated. A line diagram of the set-up utilising the single-pass gas cell can be seen in Figure 5.16. The analogue to digital converter (ADC) and DAC card (National Instruments USB-6212 OEM) was set to record data from the detector and amplifier at 100kS/s (kilo-samples per second) at 16bit resolution. As in Chapter 4, to control the flow of methane to the cell, methane and synthetic air cylinders were connected up to a pair of mass flow controllers, regulated by a set-point controller. For this experiment, a 1010ppm methane in air cylinder was utilised. The synthetic air cylinder used has a certified trace hydrocarbon level of <0.1ppm.
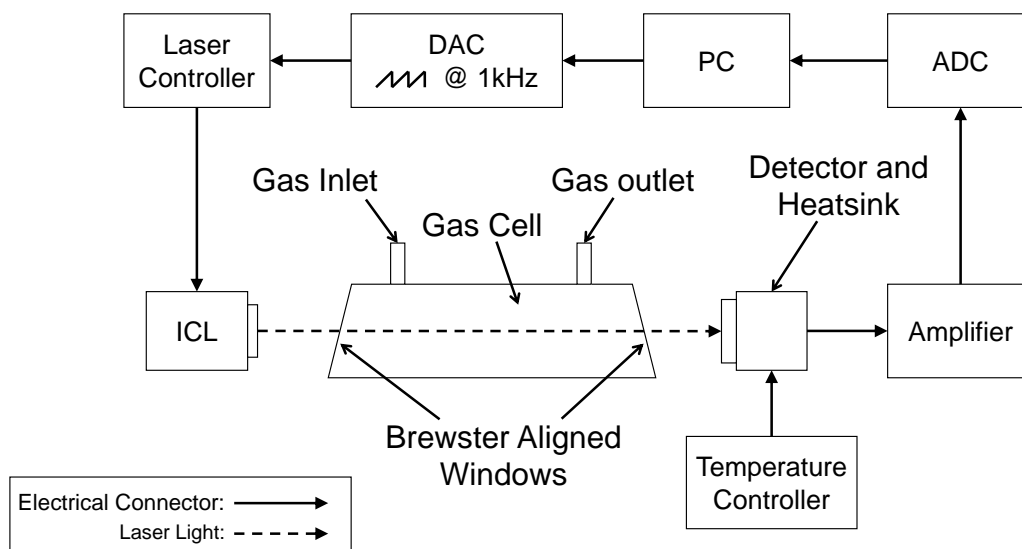
Figure 5.16: *Line diagram of initial experimental set-up utilising a 25cm pathlength single-pass gas cell.*

To determine the optimum temperature and current settings for the ICL so that the gas absorption line was centred on the current modulation ramp, the mass flow controllers were set so that gas from the methane cylinder was flowing at 1000 scc/min to the gas cell. By slowly adjusting the current and temperature, optimal conditions of 40.6mA and 34.5°C could be obtained with a 0.1Vpp sawtooth modulation waveform from the DAC card providing a 10mA current modulation. A graph showing the comparison between signals detected with and without methane present can be observed in Figure 5.17.

Measurements were then taken of the target absorption lines between 0 and 1010ppm methane concentrations by using the mass flow controllers to regulate the flow rates from the cylinders. The flow rates from each controller were set to total 1000 scc/min for each concentration. Measurements were then averaged over 1 second to reduce noise levels.

It was noted when attempting to analyse these measurements, the apparent absorbance values produced were lower than expected for a gas cell of this pathlength. It was thought that this discrepancy could be caused by a dark current on the detector.

To attempt to confirm this hypothesis, a modified version of the injection current modulation waveform was produced that caused the current to drop below the threshold level for the ICL for 2ms every second. This would allow a measurement of the "baseline" voltage level of the detector. A graph showing a portion of the modified waveform can be observed in Figure 5.18.
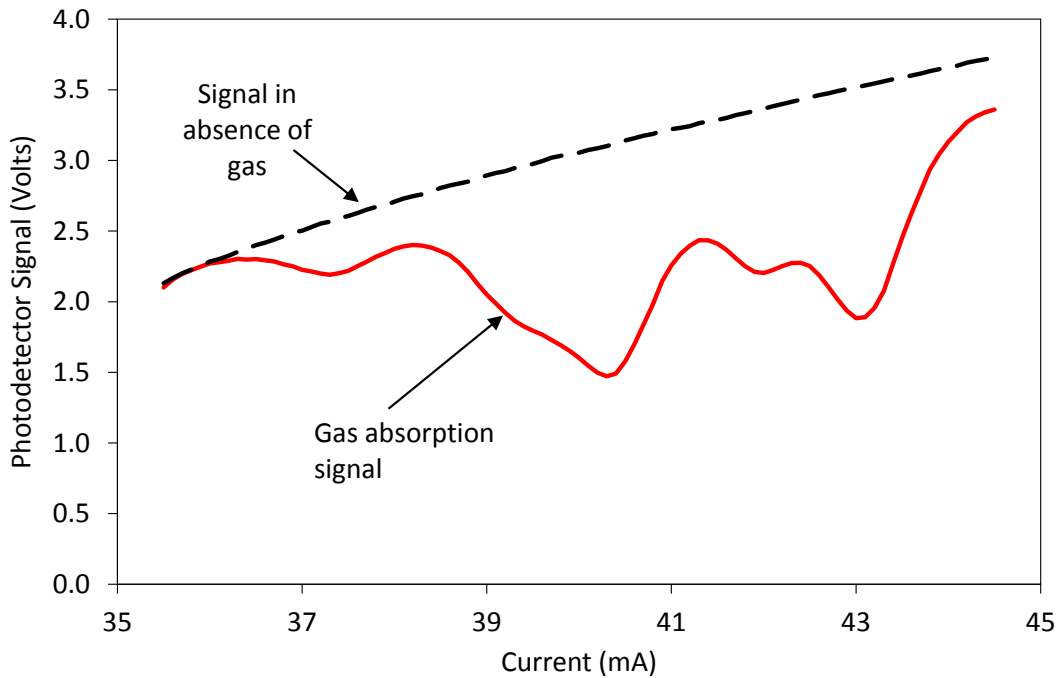
Figure 5.17: *Comparison between detected signals with and without the presence of 1010ppm methane.*

By subtracting this baseline from the signal when performing the analysis, an absorbance value could be produced that matched that seen with the data from the HITRAN database [5]. Figure 5.19 shows a comparison between the detected absorbance signal at 1010ppm and the same absorption lines from the HITRAN database. The graph shows a high correlation between the two curves, with some discrepancy seen at the edges. This is likely due to the detected signal at those points being in close proximity to the edge of the sawtooth waveform. The remaining discrepancies in the absorption peak strength and wavelength are likely caused by the data from HITRAN only covering a single isotopologue in this plot.
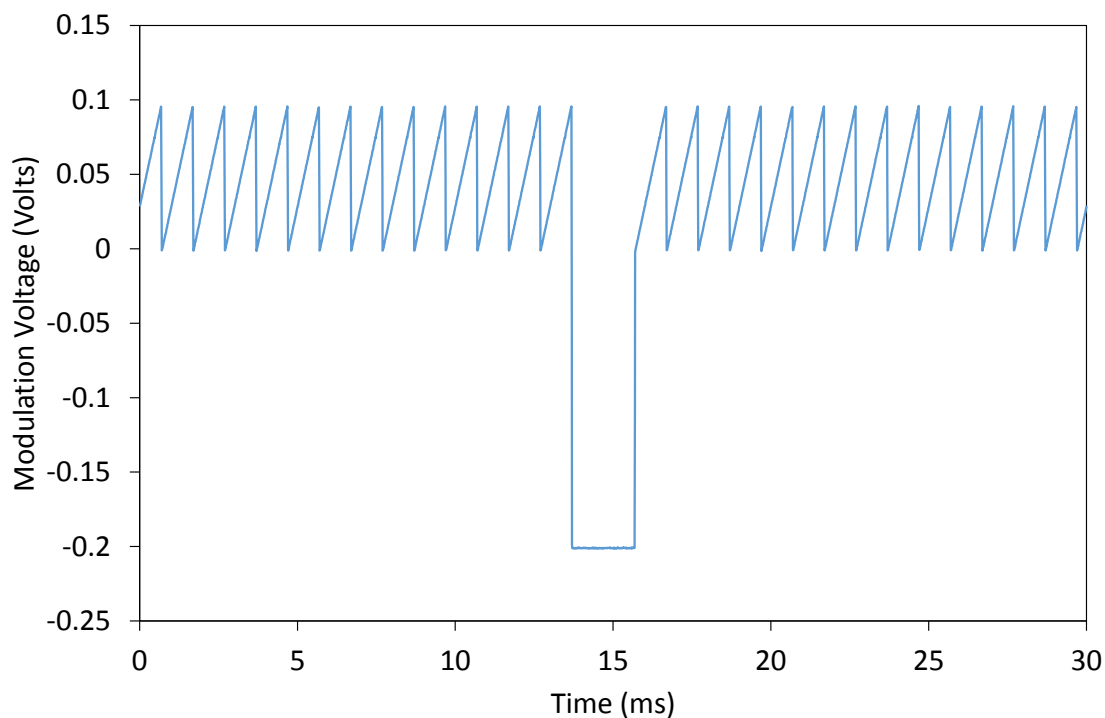
Figure 5.18: *Example section of the modified modulation waveform containing period to drop laser current below the lasing threshold to measure the dark current on the detector for 2ms every second.*
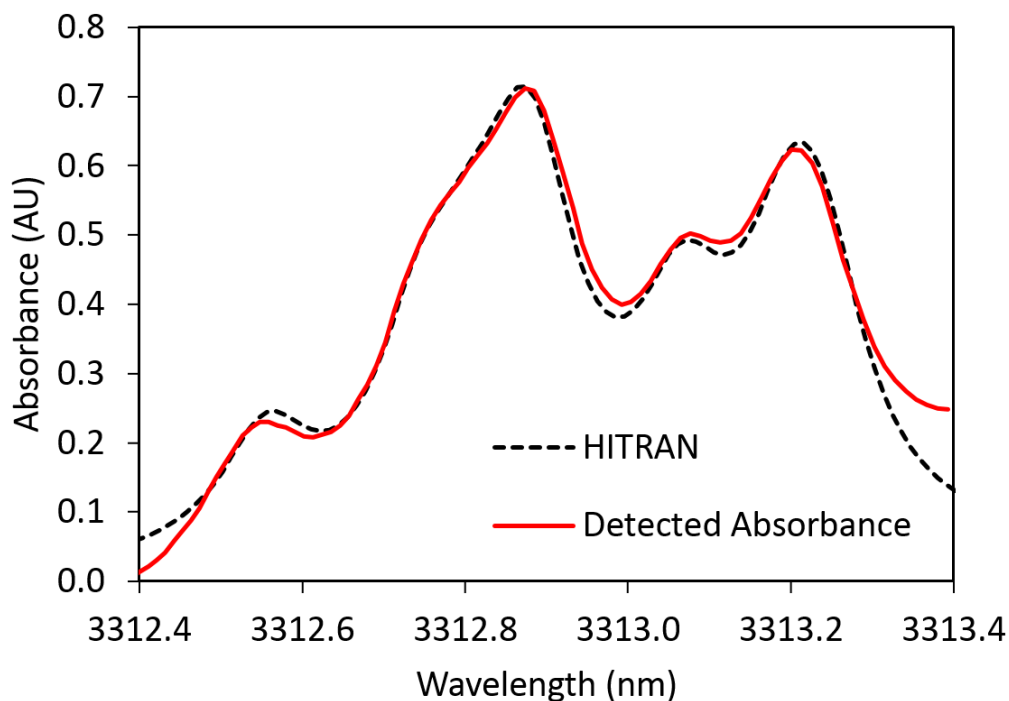
Figure 5.19: *Comparison between the detected absorbance and data from the HITRAN database for 1010ppm methane concentration, showing a high correlation between the two.*

With this solution in place, the value for the dark current could then be subtracted from the detected signals for the remaining concentrations. With this, a graph of peak absorbance against concentration could be plotted as seen in figure 5.20. A calculation for the NEA was then performed, resulting in a standard deviation of 1.8×10^{-3} AU. Using this value, a single-point limit of detection of 2.2ppm for a 1 second average could be calculated by comparing it against the absorbance strength seen at 50ppm.

Figure 5.20: *Concentration curve for single-pass cell set-up.*

Although the absorption line strength at this wavelength is approximately 45 times greater than the methane line targeted in the near infrared, the limit of detection is only approximately four times smaller. This can likely be attributed to the increased noise of the detectors and lasers available in the mid-infrared over those in the near infrared.

5.4.2 Integrating Sphere

To attempt to improve the limit of detection of the system, the single-pass gas cell was replaced with a 4 inch diameter integrating sphere with Infragold [6] interior

coating. A line diagram showing the adjusted experimental set-up can be observed in Figure 5.21. The integrating sphere was adapted so that there were two ports for the laser and detector, along with gas inlet and outlet ports. Thin blown polyethylene was used for the windows on the ports for the detector and laser, as this was found to be thin enough to reduce any interference fringes whilst having a high transmission at this wavelength.
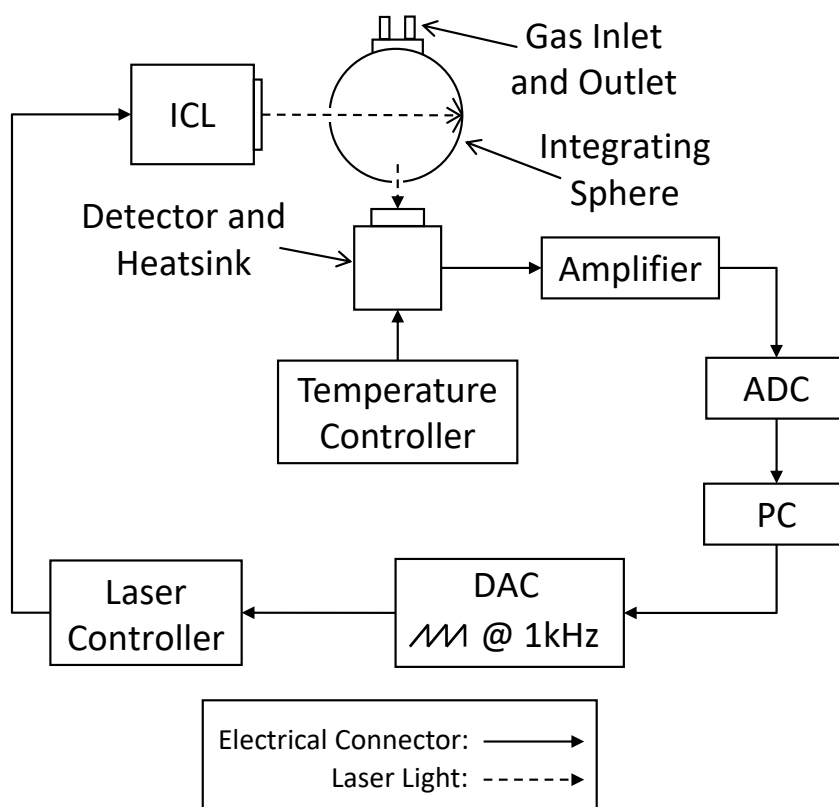
Figure 5.21: *Line diagram of experimental set-up using an integrating sphere.*

Using Equation 3.12 in Chapter 3, the integrating sphere was calculated to have a theoretical pathlength of 1.079m±0.008m, using a port fraction of 0.04±0.005 and reflectivity of 0.95±0.005. However when initial absorbance calculations were performed, it was noted that the absorbance value was significantly lower than expected. As the dark current was already being accounted for, it was likely that the issue this time was that the actual pathlength did not match up with the calculated pathlength. When compared with the absorbance values obtained for the single-pass

cell, a pathlength of 54.5cm was calculated. This equates to a coating reflectivity of 0.88, calculated using equations 3.12 and 3.13.

Attempts were made to clean the sphere using the manufacturers instructions (spraying with acetone, rinsing with de-ioised water, then drying with clean, dry air), however no increase was seen. It can therefore be assumed that the diffuse coating on the inside of the sphere either: does not uniformly coat the surface, with a reduction in the average reflectivity of the sphere being the result; the coating is less reflective than stated in the datasheets; or a combination of the two.

A second sphere was purchased in an attempt to isolate the issue with the pathlength. It was thought that perhaps over time the coating had become damaged in some respect. On testing the new sphere, however, it was found to produce the same pathlength as the old sphere. Although the pathlength of the sphere was not to the level that was expected, it was still over twice as long as that of the single-pass cell, potentially providing a improvement in the limit of detection.

To confirm this, measurements of the methane absorption line were performed at concentrations between 0 and 250ppm using the same procedure as for the single-pass cell. A graph displaying the calculated absorbances against their respective concentrations can be seen in Figure 5.22. A calculation for the NEA was then performed, resulting in a standard deviation of 1.6×10^{-3} AU. Using this value, a single-point limit of detection of 1.0ppm could be calculated by comparing it against the absorbance strength seen at 50ppm.

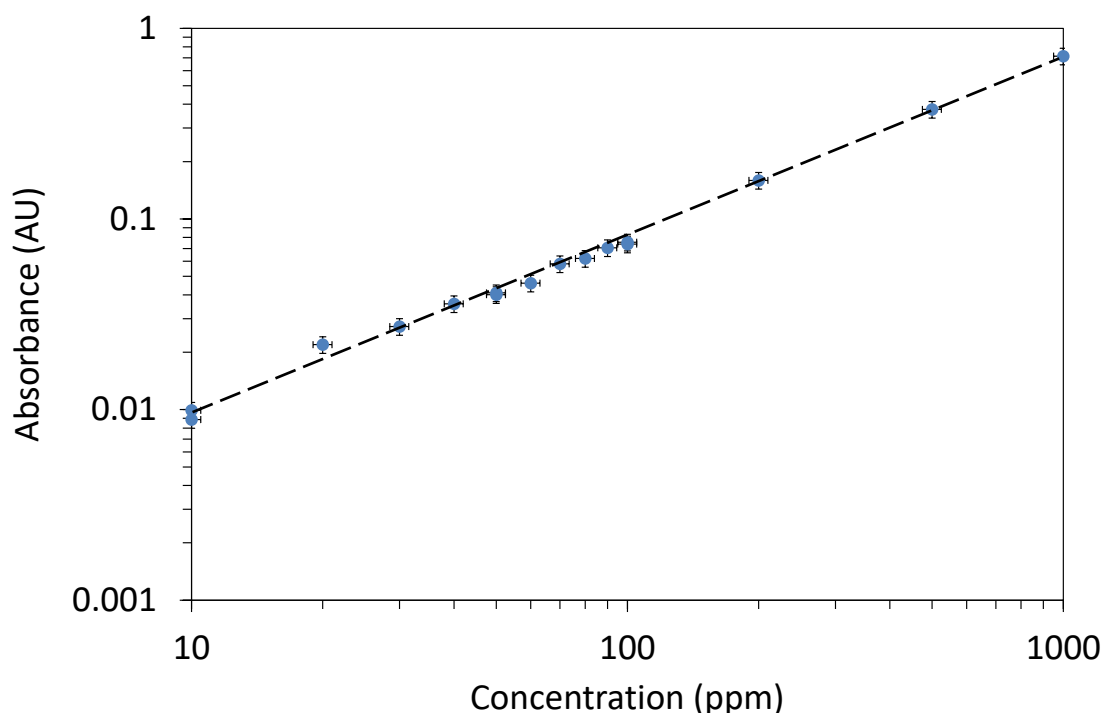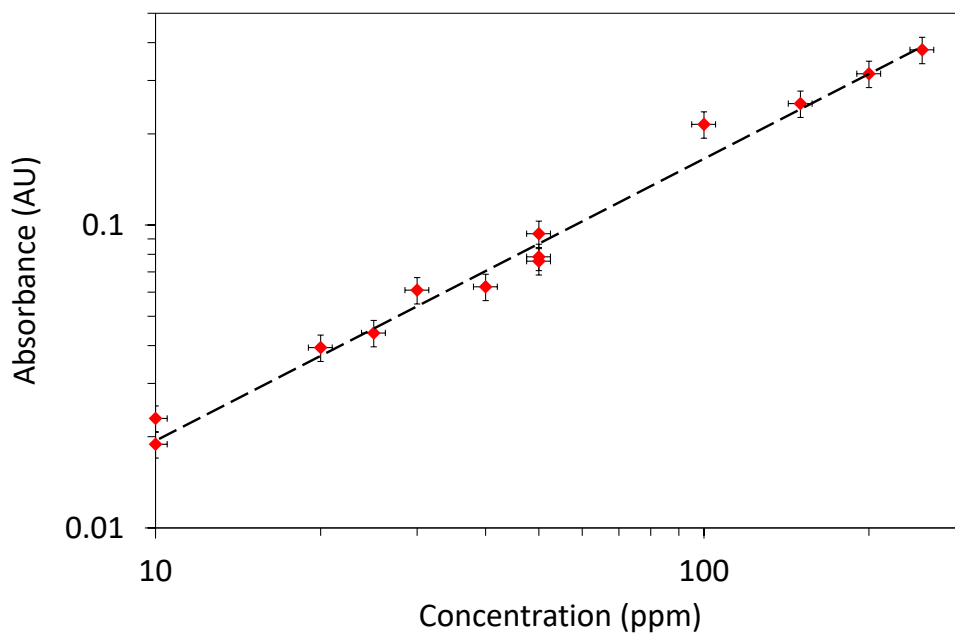**Figure 5.22:** *Concentration curve for integrating sphere set-up.*

5.4.3 Allan Variance

As discussed in chapter 3, to determine the optimum averaging time of the system an Allan variance analysis needed to be performed. To achieve this, the integrating sphere needed to contain a (relatively) constant methane concentration over a period of 1 hour. The best way to achieve this was to feed a constant low flow of a set methane concentration to the integrating sphere from a cylinder. As such, the 0.1% methane cylinder previously used was swapped for a 50ppm methane in air cylinder.

In an attempt to provide higher quality measurements at both short and long time intervals, the data acquisition card was replaced by one with the ability to record at a higher number of samples per second (NI USB 6366) at a 16 bit resolution. Using this new acquisition card, the maximum rate that could be reliably recorded was found to be 1MS/s; above this value buffer overflow errors were being triggered on the computer being utilised. The current modulation amplitude was also increased slightly (from 0.1Vpp to 0.15Vpp) to make use of the non-absorbing region next to the methane line, allowing a more accurate baseline to be provided. An example of the resultant measured absorbance can be observed in Figure 5.23.
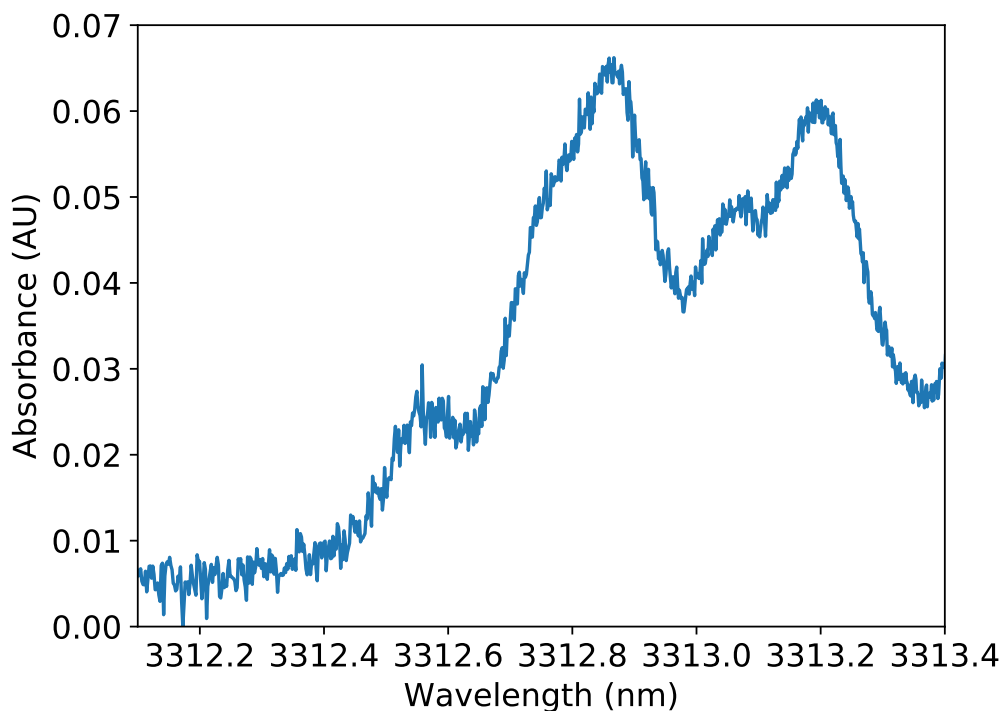
Figure 5.23: *Example of 1 second averaged absorbance detected with increased acquisition rate for 50ppm methane concentration.*

A measurement of a flow of 100 scc/min from the synthetic air cylinder was made before the mass flow controllers were set to provide a constant flow rate of 100 scc/min from the 50ppm methane cylinder. The Labview code was then set to record for 1 hour to provide the time series data for the Allan deviation. One second averages were then made throughout the data series, providing 3600 absorbance values for this time period. A graph of the peak absorbance values can be observed in Figure 5.24. It can be seen that although there is some fluctuation in the peak absorbance level over time, it remained reasonably well centred around 0.07 AU.
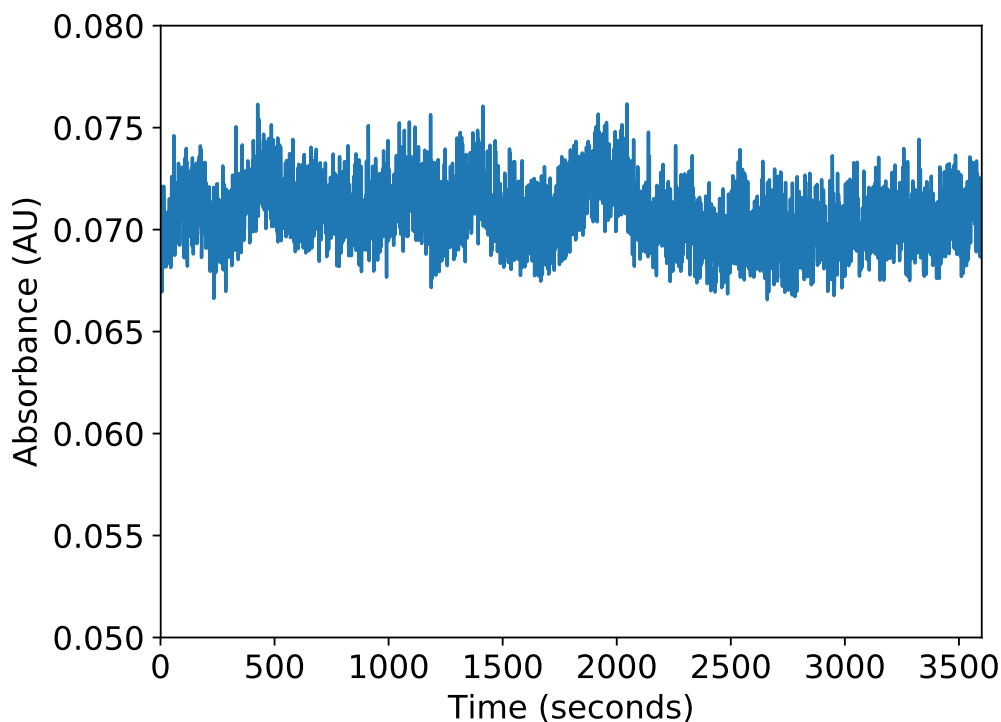
Figure 5.24: *Variation in detected absorbance over a one hour time period.*

Using the equations discussed in Chapter 3, an Allan deviation of the absorbance data could be calculated. A plot of the resultant calculated Allan deviation values can be seen in Figure 5.25. The plot follows the expected form of an Allan deviation, with an initial drop for the white noise before increasing due to drift in the recorded signal. Although there are points towards the end of the graph that drop below the initial minimum, these are likely to be unstable as they fluctuate widely at that point. Therefore it should be stated that an optimum averaging period occurs at approximately 25 seconds.

5.4.4   Absorption line fitting

To make full use of the knowledge gained from performing the Allan deviation, an absorption line fit of data obtained over this averaging time (25 seconds) was performed using a MATLAB script provided by Dr. Daniel Francis. The Levenberg-Marquardt fitting algorithm, as discussed in Chapter 3, was utilised to perform this task.
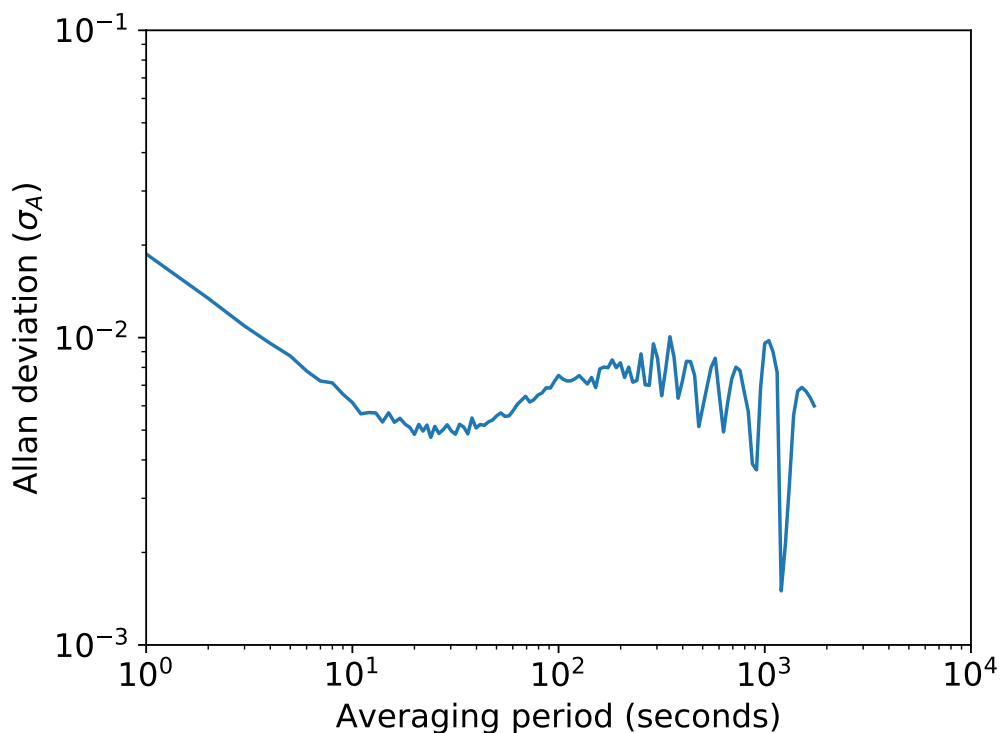
Figure 5.25: *Allan deviation for one hour of detected absorbance data.*

Due to the complex nature of the target absorption feature, a brief test to determine how many peaks the algorithm should fit to was required. The suitability of the individual fits was determined by comparing their residuals, with a lower residual meaning a better fit. As the number of peaks was increased, the residual produced continued to decrease up to ten individual peaks. However, on inspecting the curves produced by the higher peak number attempts, and comparing them against the HITRAN data for this region, it suggested that the algorithm was attempting to fit to absorption lines outside of the target area. It was therefore found that a Lorentzian fit of 7 evenly spaced peaks provided the best result, matching the number of absorption lines present according to the HITRAN database. An example of the fit produced can be seen in Figure 5.26.

To gain a limit of detection from this fitting process, the absorption line fits were divided by the HITRAN data for the absorption feature. A standard deviation was then taken to provide the limit of detection. Using this technique, a limit of detection of 0.3ppm was estimated.
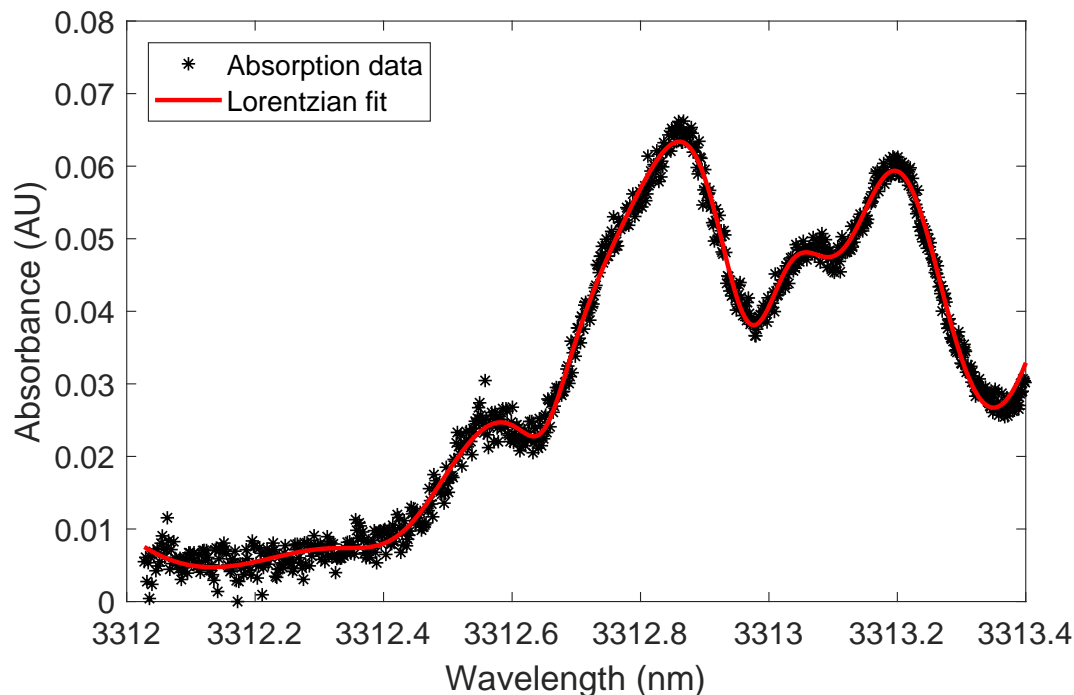
Figure 5.26: *Example of absorption line fit using the Levenberg-Marquardt algorithm for a concentration of 50ppm, using 7 overlapping individual lines.*

5.5   Conclusions

In this chapter, investigations were performed into the viability of using an interband cascade laser, coupled with an integrating sphere, for use in methane detection. A full characterisation of the laser and detector set-up was performed. It was found that at low modulation frequencies, the signal recorded on the detectors had a noticeable curvature. To correct this, an injection current modulation frequency of 1kHz was employed for all future measurements. A full noise analysis of the experimental set-up was performed, with a maximum noise value of 2.2×10^{-6} VHz$^{-1/2}$ recorded for the laser, corresponding to 1.5×10^{-3} AU.

Measurements of methane were performed with the ICL using both a 25cm pathlength single-pass gas cell and an integrating sphere with an effective pathlength of 54.5cm. Concentration curves were produced using each gas cell, with single point limit of detections of 2.2ppm and 1.0ppm found for the single-pass cell and integrating sphere

respectively. It is thought that the performance of the integrating sphere is limited by the reflectivity of the Infragold coating which has a manufacturer-quoted value between 94 and 95% in the mid infrared. Calculations showed, however, that a shorter pathlength than expected was achieved, with a mean reflectivity of approximately 0.88.

Improvements to the limit of detection were sought through the use of an Allan deviation plot to find the optimum averaging period and utilisation of absorption line fitting techniques. It was found that the optimum averaging time for this system was 25 seconds. Using this knowledge, an absorption line fit was performed for this duration, providing a limit of detection of 0.3ppm.

It can be concluded from the work carried out in this chapter that the combination of ICL and integrating sphere would be beneficial for use in the detection of methane on light aircraft. As such, investigations into the design and development of instrumentation for this purpose are described in Chapter 6.

References

[1] Richter, D., Fried, A. and Weibring, P. (2009), "Difference frequency generation laser based spectrometers," *Laser and Photonics Review*, vol. 3, no. 4, pp. 343–354.

[2] Asobe, M., Tadanaga, O., Yanagawa, T., Umeki, T., Nishida, Y. and Suzuki, H. (2008), "High-power mid-infrared wavelength generation using difference frequency generation in damage-resistant Zn:LiNbO3 waveguide," *Electronics Letters*, vol. 44, no. 4, pp. 288–290.

[3] Hodgkinson, J. and Tatam, R. P. (2013), "Optical gas sensing: a review," *Measurement Science and Technology*, vol. 24, no. 1, p. 012004 (59 pages).

[4] Ingle, J. D. and Crouch, S. R. (1988), *Spectrochemical Analysis*, Prentice Hall PTR, New Jersey, USA.

[5] Rothman, L., Gordon, I., Babikov, Y., Barbe, A., Chris Benner, D., Bernath, P., Birk, M., Bizzocchi, L., Boudon, V., Brown, L., Campargue, A., Chance, K., Cohen, E., Coudert, L., Devi, V., Drouin, B., Fayt, A., Flaud, J.-M., Gamache, R., Harrison, J., Hartmann, J.-M., Hill, C., Hodges, J., Jacquemart, D., Jolly, A., Lamouroux, J., Le Roy, R., Li, G., Long, D., Lyulin, O., Mackie, C., Massie, S., Mikhailenko, S., Müller, H., Naumenko, O., Nikitin, A., Orphal, J., Perevalov, V., Perrin, A., Polovtseva, E., Richard, C., Smith, M., Starikova, E., Sung, K., Tashkun, S., Tennyson, J., Toon, G., Tyuterev, V. and Wagner, G. (2013), "The HITRAN2012 molecular spectroscopic database," *Journal of Quantitative Spectroscopy and Radiative Transfer*, vol. 130, pp. 4–50.

[6] Labsphere Inc., "Infragold NIR-MIR Reflectance Coating," https://www.labsphere.com/labsphere-products-solutions/materials-coatings-2/coatings-materials/infragp-d/, Date Accessed: 21/11/2017.

Chapter 6

Development of instrumentation for the detection of atmospheric methane on a light aircraft

Laboratory measurements of methane using an interband cascade laser and integrating sphere were undertaken in Chapter 5. Having shown a limit of detection below that of the background atmospheric methane level, it was decided to use this combination for the instrument. This chapter covers the work undertaken in designing and developing this instrument, with a laboratory test taking place before being installed in the aircraft and an initial flight test.

6.1   Background

Light aircraft hold a number of advantages over other forms of aviation with regards to measuring in situ. These include being able to fly closer to (and slower through) any potential sources/plumes of methane, allowing for longer, more accurate measurements of the source to take place.

To facilitate measurements of atmospheric methane in situ, a Scottish Aviation Bulldog light aircraft owned by Cranfield University (as seen in Figure 6.1) was proposed. This aircraft is a two-seater training aircraft with a maximum speed of 130 knots, stall speed of 54 knots, and range of 540 nautical miles [1]. Within this

aircraft, a certified mounting box is present (as shown in Figure 6.2) that allowed instrumentation to be secured inside the aircraft. By utilising the mounting points within the box that were already installed, it was thought that the process of flight certification could be simplified. This did, however, present a number of design restrictions on the size, weight, and power requirements of the instrument. These can be seen laid out in Table 6.1.

To reduce the need for the additional complication of certification, components chosen to be used within the instrument would need to be CE marked (as required). This particularly applied to electrical components. Important mechanical fixings, such as the bolts to secure the instrument to the aircraft, had to be traceable. By doing so, the need to have any assessment done on individual components is removed. As such, only off-the-shelf components could be utilised in the instrument.

The main potential risks that need to be addressed in the development of instrumentation for measurements in-flight are fire hazards, mechanical instability, and power drain. By using CE marked components in the operating range as stated by the manufacturer reduces the potential fire risk involved. To mitigate any mechanical hazards, such as a bolt coming loose mid-flight, anti-vibration washers and nuts will be utilised, whilst the instrument itself will be contained within a sealed box. Finally, to mitigate for a power drain from the instrument potentially causing the aircraft to malfunction, the power to the instrument is required to have a fuse that will trip when too much power is drawn.

Table 6.1: *Design restrictions for instrumentation, making use of previously certified modification to the Bulldog.*

Parameter	Constraint
Size (mm)	300x167x270
Power (Watts)	140
Weight (kg)	5

Figure 6.1: *The Cranfield Scottish Aviation Bulldog aeroplane in flight.*

Figure 6.2: *Mounting box inside Scottish Aviation Bulldog, with internal dimensions of 300X167X270mm.*

6.2   Choice of Components

To meet these criteria for the design restrictions, careful consideration was required in the choice of components to replace the laboratory equipment utilised in the previous chapter, with the set-up still matching that seen in Figure 5.21. These components would have to be relatively small and lightweight, have low power consumption, yet still be able to provide sufficient performance for reliable measurements to be made. As mentioned previously, electrical components had to be CE marked, ruling out the use of any custom designed electronics.

Due to the higher compliance voltage (6V) of the ICL compared with other laser diodes, the range of available laser controllers was quite limited. The controller chosen (Thorlabs ITC102) provides both current and temperature control that covers the operating range of the ICL, whilst also being relatively compact. Its large heatsink would also prevent it from overheating in the enclosed environment. The choice of thermal controller for the detector (Wavelength Electronics HTC3000 & HTCEVALPCB) followed a similar reasoning, with a large current output capability and a reasonable sized heatsink for cooling.

Due to their small size, low power requirements, and reasonable performance, the amplifiers chosen were the switchable gain transimpedance amplifiers that come connected to standard silicon detectors from Thorlabs (PDA36A-EC). The detectors were removed from these amplifiers, with a BNC cable soldered to the input pins to allow input from the Hamamatsu MCT detectors. These amplifiers have different performance characteristics than the Femto amplifier used previously. The bandwidth of the new amplifier is higher (5.5MHz compared with 400kHz), however the gain setting utilised is lower, 4.75×10^3V/A against 1×10^5V/A. The data acquisition card (National Instruments USB-6212 OEM) was chosen due to its known high performance capabilities and its compact nature.

The choice of PC to control the instrument was more complicated. The chosen

PC would have to be small, like the other components, whilst also being able to run the Labview code previously produced, and powerful enough to not limit measurements. This is a combination that does not usually occur, as powerful PCs are often larger and require significantly more power. The PC eventually chosen (Zotac ZBOX-PI320) was approximately the same size as many of the alternative miniature computers on the market (such as the Raspberry Pi), however it had a more powerful processor and larger RAM capacity. The expandability of the PC is limited (with only USB, micro SD, and ethernet ports available) however this was sufficient for use in this project. The memory used in this PC was entirely solid state, making it more robust than a computer utilising a conventional hard disk drive.

Two different voltage regulators (RS Pro SD-15B-5 and Murata Power Solutions UEI-12/5-Q48N-C) were used due to the need for both 5V and 12V supplies for different components. Finally the pump (Sensidyne AA120CNSN) was chosen primarily for its small size, however it still has a reasonable maximum flow rate, approximately 2.4 litres/min. A full list of the components can be seen in Table 6.2.

6.3 Development of instrument

6.3.1 Design progression

To determine how the selected components would be arranged inside the instrument, 3D computer aided design (CAD) block diagrams of the possible internal layout were produced. Each block in these diagrams represents the total space that an individual component takes up, with the wire frame around the outside of the instrument representing its maximum size. Figure 6.3 shows the initial design made using this technique. It was originally thought that a cuboid integrating cavity could be fabricated for use within the instrument to reduce the space required, however it was decided for later designs that this would be unnecessary. At this stage the design was also incomplete, as components such as the voltage regulators and pump had not yet been included.

Table 6.2: *List of components in the instrument.*

Component	Make/model	Thumbnail image
Laser	Nanoplus ICL	
Laser controller	Thorlabs ITC102	[2]
Detector and heatsink	Hamamatsu P3981 and A3179-01	
Detector temperature controller	Wavelength Electronics HTC3000 and HTCEVALPCB	
Amplifier	Switchable gain amplifier from Thorlabs PDA36A-EC	[3]
Gas cell	Labsphere Infragold coated integrating sphere	
ADC/DAC	National Instruments USB-6212 OEM	[4]
Pump	Sensidyne AA120CNSN	[5]
Voltage regulators	RS Pro SD-15B-5 and Murata Power Solutions UEI-12/5-Q48N-C	[6, 7]
PC	Zotac ZBOX-PI320	[8]
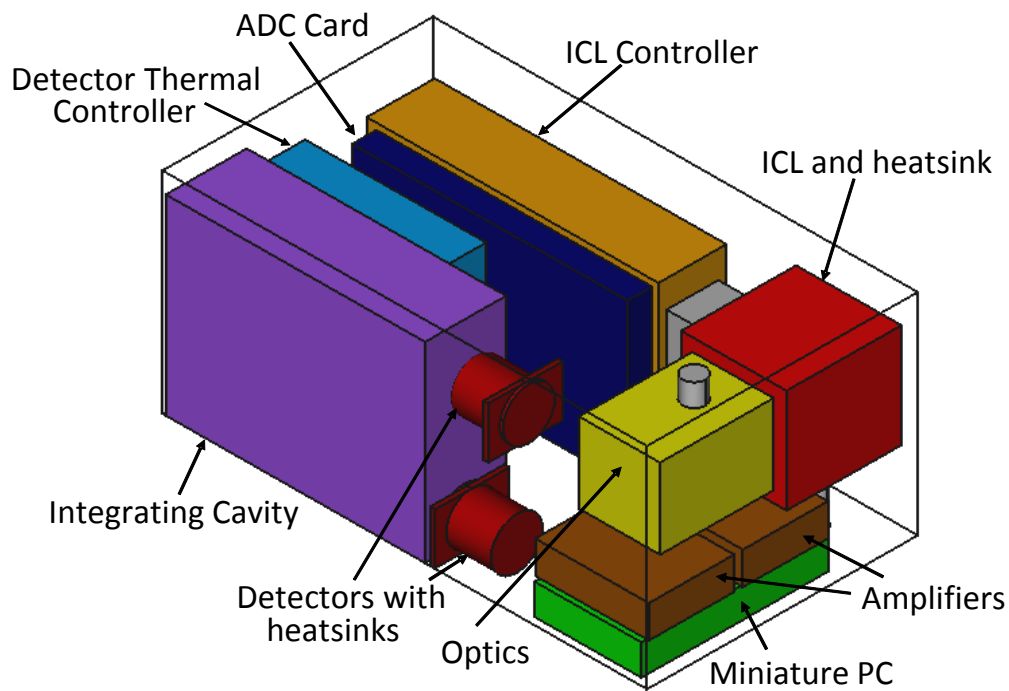
Figure 6.3: *Initial 3D block diagram of instrument, with blocks representing the main components to be used. The dimensions of this design are 299X167X132mm.*
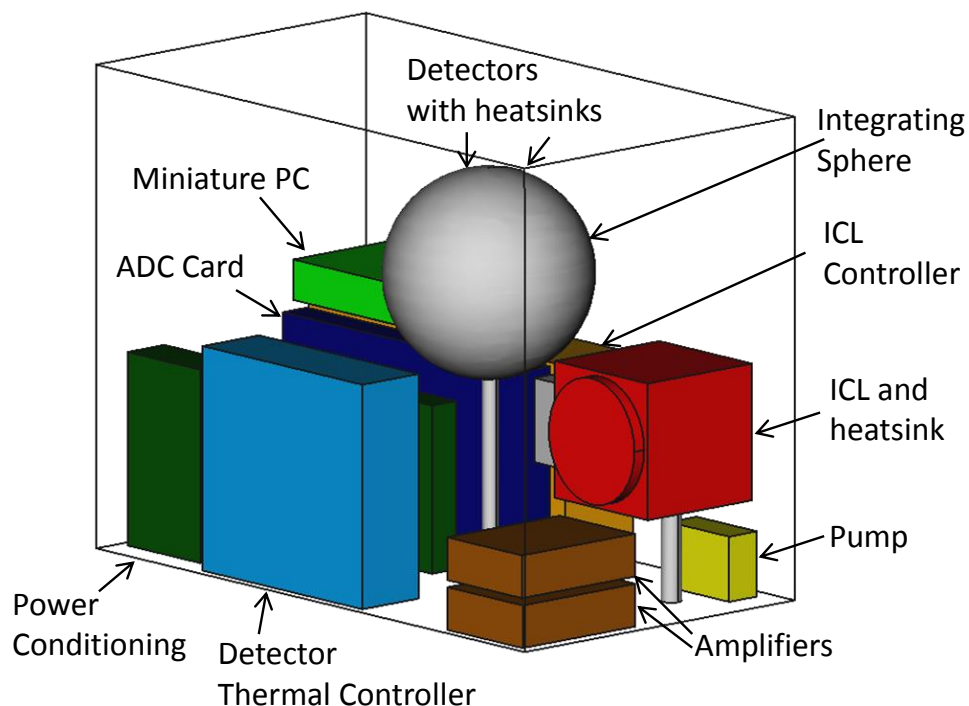
Figure 6.4: *Evolution of initial 3D block diagram, now including all components with close approximations to positioning inside instrument. Dimensions of this design are 299X167X230mm.*

Figure 6.4 displays an evolution of the initial design, including all the components

that were omitted previously whilst also arranging them slightly differently to make more efficient use of the space available. The cubic integrating cavity has also now been replaced by an integrating sphere.

During the initial design process, it was thought that additional optics would be required to direct light from the laser to the sphere, including both collimating optics and optical fibre. This is displayed clearly in Figure 6.3 and, although this is not shown in Figure 6.4, it was still expected to be the case at this stage. The additional optics were thought to be needed as a result of previous experience of other researchers in the laboratory. When using near infrared DFB lasers, optical feedback from an integrating sphere caused large noise in the laser output if the laser was butt-coupled to the sphere. These designs were produced before it was found that this feedback was not an issue with this configuration.
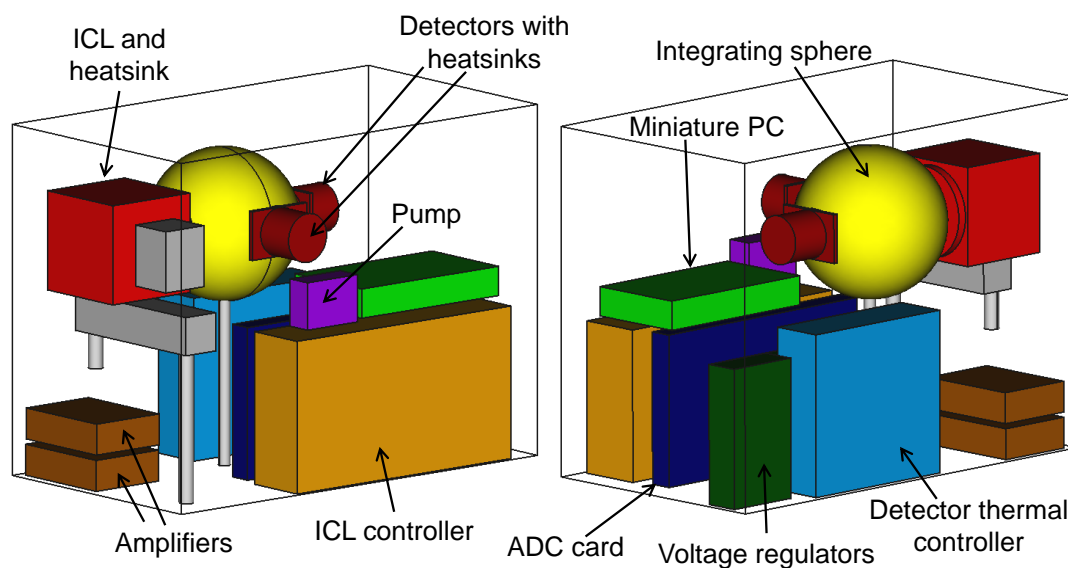
Figure 6.5: *3D CAD block drawing (left and right views) of the internal components of the instrument in its final form. Dimensions of this design are 295X165X250mm.*

Where the changes between the first and second designs were quite significant, the final design of the instrument (Figure 6.5) can be seen as more of an evolution on the previous design, with only a few subtle alterations. The ICL has been positioned so that it emits directly into the integrating sphere, rather than relying on bulk optics

previously. This would allow the light intensity in the sphere to be higher due to no losses being incurred through coupling to the fibre. The positions of the other components, especially the laser controller and ADC card, have also shifted slightly to allow more room for mounting (discussed in section 6.3.2) and for any connections needed.

6.3.2   Assembly of instrumentation

To contain the selected components, an aluminium base "tray" and lid were fabricated, with the lid to be connected to the tray by four support struts, one in each corner (see Figure 6.7 later). To secure the individual components to the base tray, a 3D printer (Ultimaker 2+) was used to create bespoke fixtures made from polylactic acid (PLA) that could be bolted to both the components and the base plate. An example of one of the 3D printed mounts can be seen in Figure 6.6, this one used to secure the detector thermal controller. A portfolio of 3D CAD diagrams and photographs of all of the mounts used is available in Appendix C.
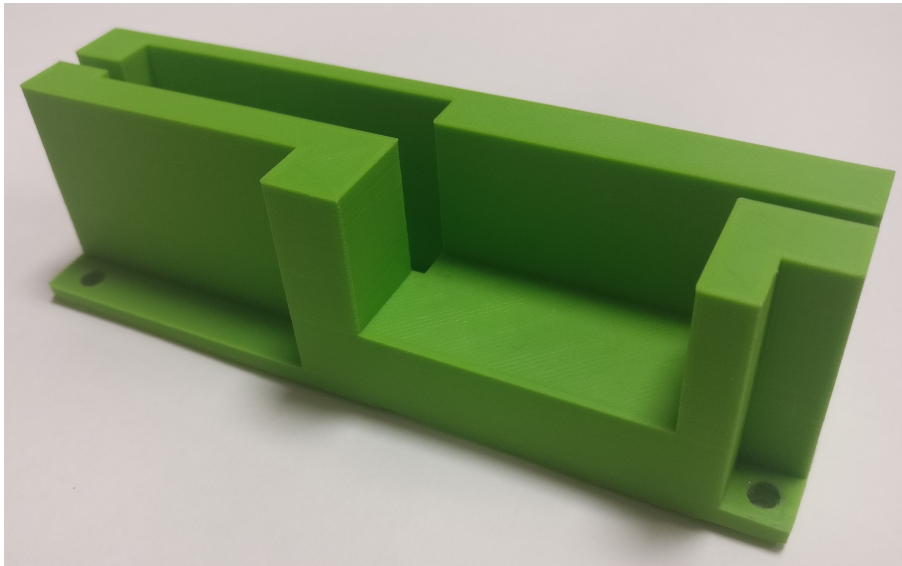
Figure 6.6: *Example of mounting used to secure components to the base tray. This example was used to mount the detector thermal controller.*

Individual mounts were created for the detector thermal controller (as seen) along with the 5V voltage regulator. Both amplifiers shared a single frame, whilst the laser controller, ADC card and 12V voltage regulators shared a mount, with the miniature

PC and pump attached to a lid that provided additional support to the three boards. The ICL and detectors used 3D printed adaptors to be secured to the integrating sphere ports.

Each mount was designed using 3D CAD software, with multiple versions of each mount required in order to fine tune how each component was to be secured. This was a time consuming process, with each version potentially taking multiple hours to be developed. A list of all the mounts produced can be seen in Table 6.3, with the times needed to print each of them displayed alongside. It can be seen that for the majority of the prints, a significant amount of time was required for them to be completed. This meant that, with multiple versions of each mount, a period of several weeks was needed solely to finalise how to secure the components.

Table 6.3: *List of 3D printed component mounts and respective print times.*

3D printed mount	Print time
ICL controller, ADC/DAC card, & 12V voltage regulator mount	35 Hours 29 minutes
Lid for ICL controller, ADC/DAC card, & 12V voltage regulator	21 Hours 23 minutes
Amplifier mount	13 Hours 1 minute
Detector thermal controller mount	7 Hours 59 minutes
5V voltage regulator mount	5 Hours 6 minutes
ICL mount bar	3 Hours 54 minutes
ICL sphere port adaptor	3 Hours 44 minutes
Detector sphere port adaptor	2 Hours 8 minutes
PC power button holder	48 minutes

With all the mount designs finalised and printed, the components and their mounts were arranged on the tray so that they matched the design seen in Figure 6.5. Pictures of the final internal arrangement can be seen in Figure 6.7.

(1st) Detector with heatsink

ICL and heatsink

Miniature PC

ICL controller

Amplifiers

Pump

(2nd) Detector with heatsink

Integrating sphere

ADC card

Detector thermal controller

Voltage regulator
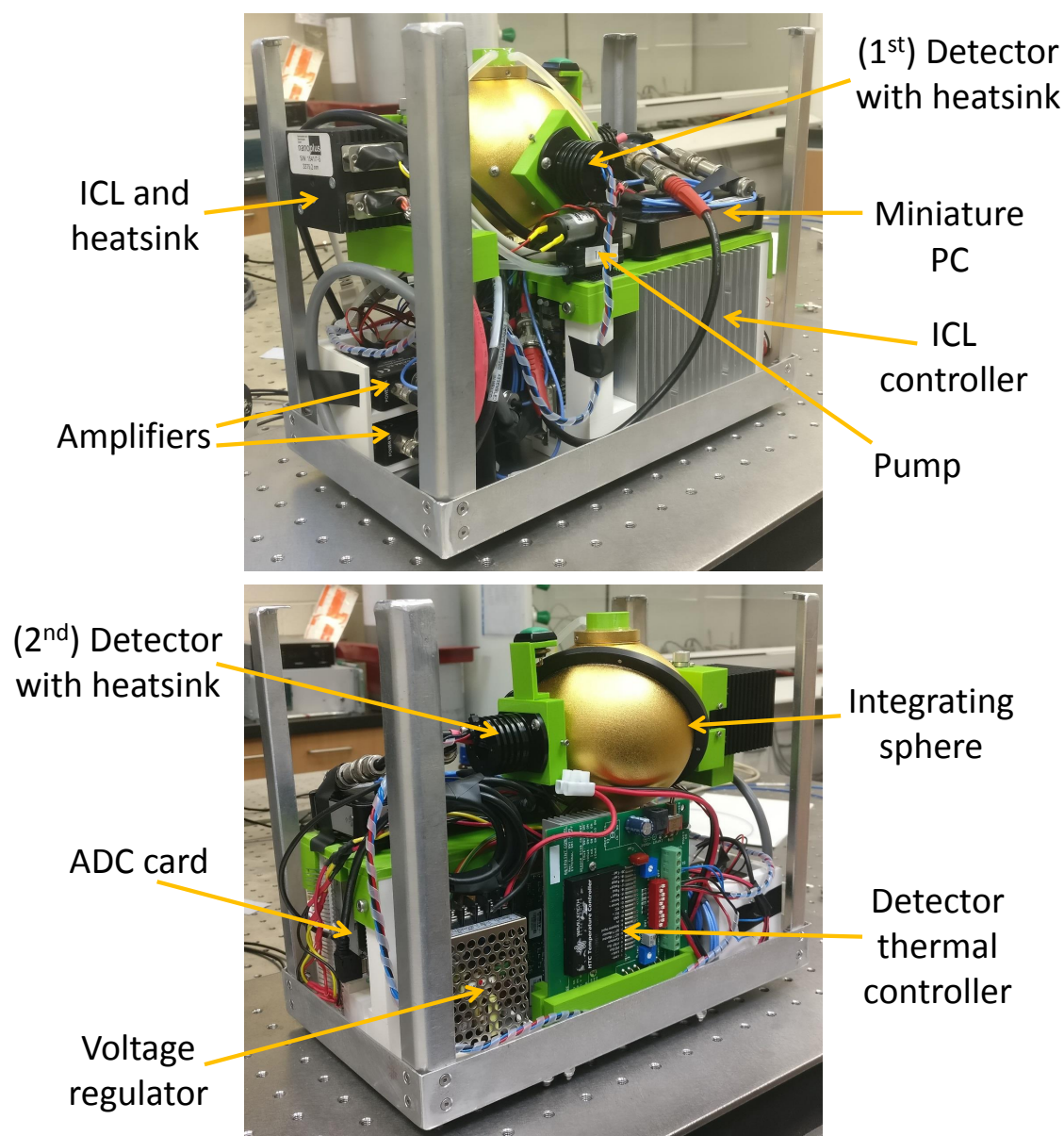
Figure 6.7: *Photographs (front and rear view) of components assembled inside instrument according to 3D model.*

To provide air to the pump from outside the instrument, an elbow gas fitting (Swagelok SS-400-9) was attached to the lid, with a length of flexible tubing running from this to the pump. In a similar manner, to control the acquisition software on the miniature PC, HDMI and USB ports were attached to the top of the lid with short leads inside the instrument connecting them to the PC. These would allow a small touchsreen (Waveshare 7 Inch HDMI LCD (C)) to be connected to the instrument to control the software in-flight. Finally, to help with cooling inside the instrument,

a vent (taking the form of a grid of small holes) was drilled into the centre of the lid, positioned so that it lined up with a vent of the same form in the mounting box in the aircraft. The exhaust air from the sphere was also directed over the internal components to assist with thermal management, removing the requirement for an additional fan. A picture of the completed instrument can be observed in Figure 6.8, with a list of its specifications in Table 6.4.

Table 6.4: *Specifications of completed instrument.*

Parameter	Constraint	Implementation
Size (mm)	300x167x270	295x165x250
Max rated power (Watts)	140	90
Weight (kg)	5	4.7
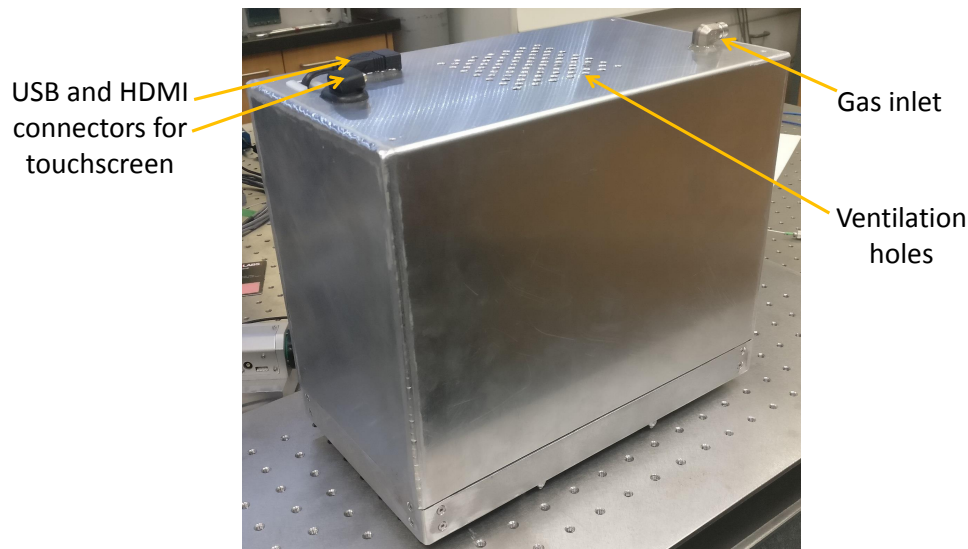
Figure 6.8: *Photograph of completed enclosed instrument.*

6.4　Laboratory Testing

To determine how the instrument performed relative to the experimental set-up used in the previous chapter, noise measurements alongside some basic methane readings were performed. When setting the temperature of the detector, it was noted that it would not stabilise at the same value previously used (-20°C). This is likely

due to the enclosed nature of the instrument putting slightly more strain on the detector heatsink. As such, a higher temperature of -15°C would need to be utilised. Based on the manufacturers datasheet for this detector, the theoretical minimum noise level at this temperature for this wavelength would be approximately $1\text{x}10^{-7}$ VHz$^{-1/2}$, providing an noise equivalent absorbance of $7.1\text{x}10^{-5}$ AU. The rest of the components, however, seemed to be operating in a similar manner to the previous benchtop set-up. Measurements of the background, detector, and laser noise of the instrument were then taken using a network signal analyser (SRS SR780) using the same process undertaken in Chapter 5. A list of the resultant measurements, alongside measurements made of the set-up used in Chapter 5, can be observed in Table 6.5. Following the same procedure used in Chapter 5 Section 5.3, these were converted into AU by multiplying by the square root of the NEBW and dividing through by the signal strength.

Table 6.5: *Individual noise values for components in the instrument compared with values of laboratory set-up in Chapter 5.*

Noise Source	Level	Equivalent level in AU	Comparison with lab instrument (Table 5.2)
Laser on	$3.3\text{x}10^{-6}$ VHz$^{-1/2}$	$2.3\text{x}10^{-3}$ AU	$1.5\text{x}10^{-3}$ AU
Detector only	$2.4\text{x}10^{-6}$ VHz$^{-1/2}$	$1.7\text{x}10^{-3}$ AU	$1.3\text{x}10^{-3}$ AU
Background	$8.7\text{x}10^{-9}$ VHz$^{-1/2}$	$6.2\text{x}10^{-6}$ AU	$6.0\text{x}10^{-6}$ AU

The noise measurements seen are slightly higher than those made of the laboratory set-up previously used. It was thought this could be attributed to a combination of the higher detector temperatures, new laser controller, and new amplifiers. To ascertain how this might affect the performance of the instrument in regards to any atmospheric measurements made in the aircraft, a measurement of a known methane concentration was performed. Gas from a synthetic air cylinder was pumped into the instrument with a measurement made, before the same was done with a 50ppm in air cylinder. Figure 6.9(a) shows the calculated absorbance made from the two measurements. It shows that, although the peak position and form of the graph

follows what has previously been observed (Figure 6.9(b)), the peaks are much less well defined.
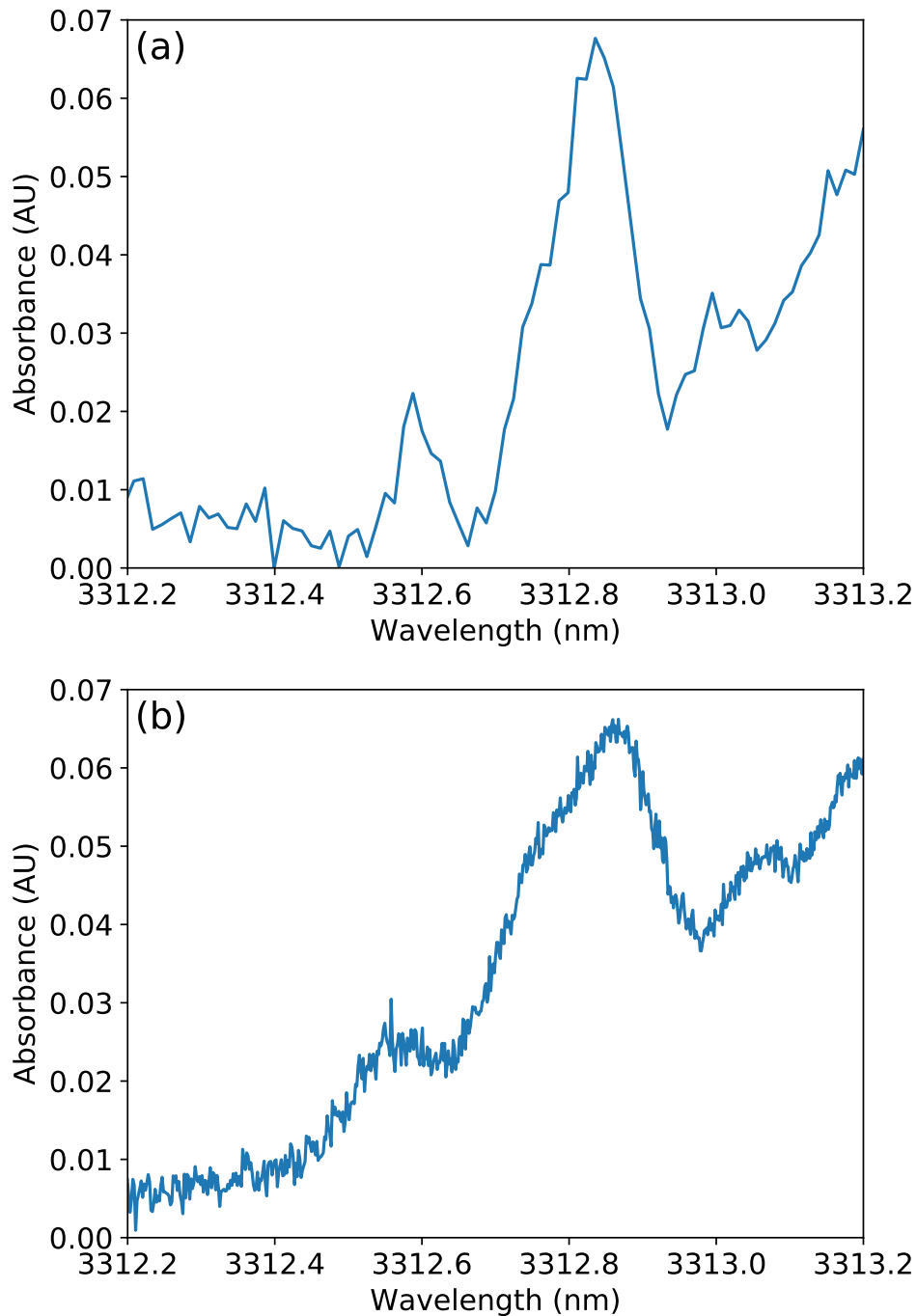
Figure 6.9: *(a) Example of 50ppm methane measurement taken using instrument. (b) Example of 50ppm methane measurement taken using setup utilised in Chapter 5.*

A calculation of the NEA was performed from two measurements of synthetic air, resulting in a standard deviation of $2.5\mathrm{x}10^{-3}$ AU. From this, a single point limit of detection of 1.6ppm could be calculated by comparing it against the absorbance strength seen with the 50ppm measurement. This LOD is higher than the single-point LOD seen with the laboratory experimental set-up (1.0ppm), matching the increased noise measurements.

The decreased definition in the peak structure and increased noise levels could likely be attributed to a combination of different sources: the different amplifiers now used, the higher temperature of the detector and interference from the close proximity of the other components. It is expected that the LOD will see an improvement through the use of averaging and line-fitting techniques, as seen in the previous chapter, where and improvement of more than 3X was seen in the limit of detection.

6.5 Flight Testing

6.5.1 Installation of instrument

Before installation of the instrument commenced, the components inside the device were swapped for operational but out-of-spec, like-for-like replacements. The components swapped were the detectors, laser, and detector thermal controller. This would allow testing of the instrumentation to occur without potentially damaging crucial components, such as the laser.

To secure the instrument to the mounting holes in the aircraft, an adaptor plate was used as the position of the components inside the instrument prevented it from being attached directly. This plate connected to the original mounting holes and had small threaded posts that were positioned so that the instrument could be bolted to them. The installation of the plate in the aircraft had to be performed by an approved organisation, with all of the components having to be traceable and logged.

6.5.2 Aircraft modification and certification

To allow the instrument to sample air in-flight, further modifications would need to be made to the aircraft. The first modification required was the introduction of an inlet plate on the outside of the aircraft (shown in Figure 6.11). This was a modification of an existing plate that would allow air to be channelled from outside to the instrument. Following this, tubing (FEP, 1/4" internal diameter) was required to be run from this plate, along the inside of the aircraft to the mounting box. Finally, a small notch made in the lid of the mounting box was made to allow the tubing to be fastened to the elbow gas fitting on the instrument. A diagram showing the layout of the aircraft with these modifications can be observed in Figure 6.10.

For the instrument to be granted permission to be flown, the size, weight, power and centre of gravity specifications of the instrument needed to be signed off and certified. An EMC check of the instrument running in the aircraft on the ground was also performed, to ensure that it would not interfere with the operation of the plane.
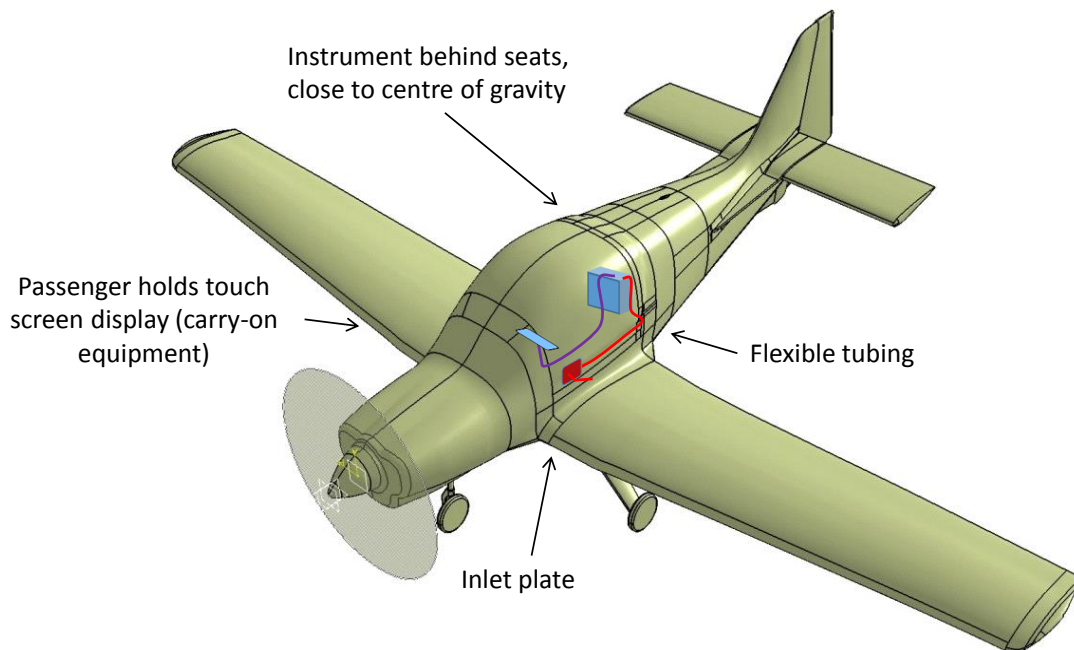
Figure 6.10: *Diagram of Bulldog aircraft showing locations of instrument, inlet plate, and tubing (taken from [9]).*
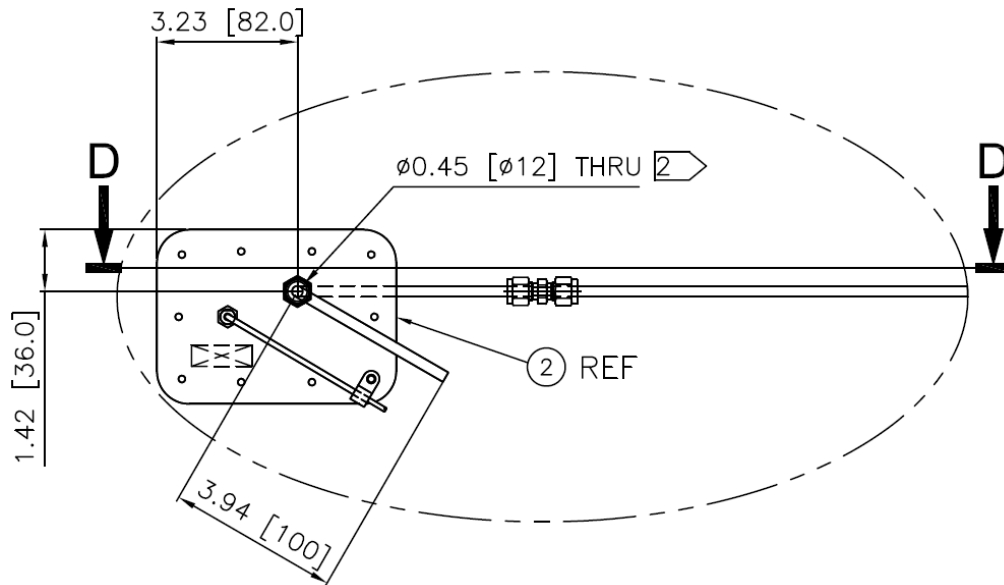
Figure 6.11: *Schematic drawing of the inlet plate on the Bulldog.*

The process of certifying the modifications and instrument was lengthy, with the first meeting with the certification company (STC Twenty One Limited) to start the process occurring in December 2015, before the modifications were finally signed off for flight testing by a Civil Aviation Authority (CAA) approved organisation (Airworthiness Assured Limited) in August 2017. The airworthiness checks tested a number of different factors to determine that the instrument posed no risk to either the aircraft or pilot. The first test was fire safety. The second check was of mechanical safety, making sure no part would come loose during flight. The final check was of the avionics, ensuring the device does not draw too much power (even accidentally) causing the aircraft to stop operating, and that it does not interfere with the communications. A portfolio of key certification documents can be found in Appendix D.

6.5.3   Flight campaign

Once installation of the instrument in the aircraft had been completed and certified, a plan for the flight testing was assembled. An initial shakedown flight of approximately 10 minutes was scheduled to check if any part of the instrument would break during take-off, landing or in-flight. The out-of-spec components were then planned to be

replaced by their fully functioning counterparts ready for the main test flights.

Two main flights were scheduled. The first involved filling the integrating sphere with a fixed gas concentration and sealing all the ports. The instrument would then be flown in this configuration to produce an Allan deviation plot to determine if any additional noise sources will impact on the limit of detection of the system. Once complete, the sphere would then be flushed out with air in preparation for the second flight. This flight would be to allow an attempt at detection of the background atmospheric methane concentration level to take place.

With the flight plan in place, the first shakedown flight went ahead as planned. The instrument was then removed from the aircraft and taken to the laboratory for assessment and component replacement. Upon inspection of the instrument components, an obvious failure had occurred. As shown in Figure 6.12, a capacitor on the ADC card had been dislodged. Although a minor fault, this forced the flight plan to be postponed slightly whilst the card was repaired.
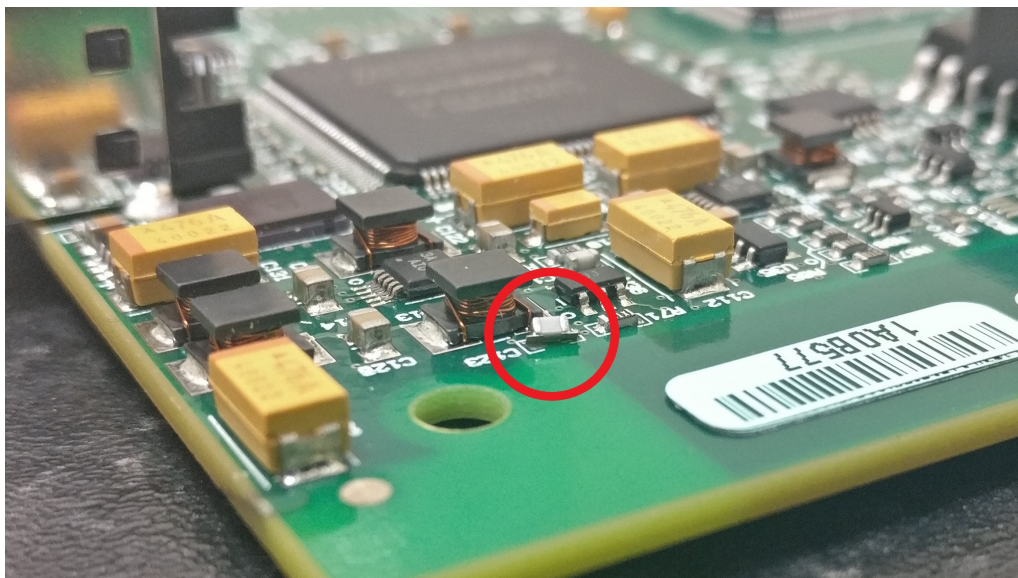
Figure 6.12: *Photograph of ADC card after shakedown flight. The red circle indicates the capacitor that became dislodged.*

This failure was attributed to the ADC card rocking slightly in its mounting, causing the capacitor to be knocked off. To combat this, small silicon pads were placed on

the corners of the card to prevent it from moving in its mounting and to help absorb any vibrations from the aircraft. These pads were also placed on the other cards to prevent the same issue occurring with them.

Further to this failure, it was noted that several of the PLA component mounts had warped during testing. The mounts were still securing the individual components as required, however they were misshapen in non-structural locations. It is thought that this deformation can either be attributed to the heat generated by the components, to moisture being drawn in from outside the aircraft, or to a combination of the two.

Once the ADC card had been repaired, and with no other serious physical damage evident in the rest of the instrument, the components were then checked to see if they were still performing correctly. It was then observed that there was an issue with the output of the laser controller. The current output of the controller was not increasing above approximately 2mA, whereas normally around 40mA would be expected. With no physical damage to the device evident, it is as yet unclear as to why this controller is not operating correctly, however it was thought that one of the mechanical trim pots on the board had failed. Although likely that the cause of the malfunction was some physical damage to the controller, it was decided that until a definitive solution to this problem could be found, the rest of the flight campaign should be postponed.

Despite the fact that the instrument stopped operating due to some minor damage to some of the electronic components, the remaining components, including the optics and laser, performed well in the shakedown test, with no further damage having been caused. This demonstrated that, once the issues with the laser controller are corrected, the instrument should function as intended.

6.6　Conclusions

In this chapter, the design and development of instrumentation to detect atmospheric methane on a light aircraft was demonstrated. The restrictions on the design were covered before the reasoning behind the choice of individual components was discussed, with a list provided. The evolution of the instrument design was then shown through the use of 3D block diagrams. The process of assembling the instrument was described along with how the components were to be mounted and secured within the enclosed instrument.

Basic laboratory testing of the instrument was performed in the form of a noise analysis and 50ppm methane concentration detection. It was found that the noise levels were slightly higher than those experienced in the laboratory set-up used in the previous chapter, with a maximum noise level of $2.3\mathrm{x}10^{-3}$ AU recorded for the laser noise, compared to $1.5\mathrm{x}10^{-3}$ AU for the laboratory instrumentation. A single-point limit of detection of 1.6ppm was estimated compared with 1.0ppm seen for the laboratory set-up. This increase is of the same proportions as that seen with the change in noise levels. It is thought that this can be attributed to the higher operating temperature of the detector used in the instrumentation coupled with the different amplifiers used and the close proximity to other components. The absorbance graph generated was also of a lower quality than that experienced previously, with the absorption peaks being less well defined.

The process of modifying the aircraft and having it certified, along with the instrument, was discussed. Several modifications to the aircraft were needed in order for the instrument to operate. An inlet plate was attached to the side of the aircraft with flexible tubing running from this plate along the inside of the plane to the instrument. Two modifications were then made to the mounting box inside the aircraft: a notch both in the lid and side of the box, with a raised cover to the notch on the lid added. The certification process was lengthy, taking 20 months to complete between December 2015 and August 2017.

A flight campaign for testing the instrument was devised, with a shakedown flight alongside two measurement flights scheduled. The shakedown flight took place as scheduled, however damage to two of the electronic components was incurred during this flight. The damage incurred to one of the components was obvious and was quickly rectified, however the issue with the second component was less obvious. With the device malfunctioning and no obvious physical damage evident, it was decided to postpone further flight testing until a definitive reason for the problem could be found. The laser, optics and remaining electronic components, however, operated as expected, demonstrating that the instrument should function as intended once the issues with the controller are rectified.

References

[1] Taylor, J. (1976), *Jane's All the World's Aircraft 1976-77*, Franklin Watts Incorporated, New York, USA.

[2] Thorlabs Inc., "ITC102 OEM Laser Diode and Temperature Controller," https://www.thorlabs.com/thorproduct.cfm?partnumber=ITC102, Date Accessed: 08/01/2018.

[3] Thorlabs Inc., "PDA36A-EC - Si Switchable Gain Detector," https://www.thorlabs.com/thorproduct.cfm?partnumber=PDA36A-EC, Date Accessed: 08/01/2018.

[4] National Instruments, "USB-6212 OEM," http://sine.ni.com/nips/cds/view/p/lang/en/nid/204360, Date Accessed: 08/01/2018.

[5] Sensidyne, LP, "AA Series Miniature Diaphragm Air Pump," http://www.sensidyne.com/micro-and-miniature-air-pumps/aa-series-micro-air-pump.php, Date Accessed: 08/01/2018.

[6] RS Components Ltd., "RS Pro Chassis Mount 15W Isolated DC-DC Converter," https://uk.rs-online.com/web/p/isolated-dc-dc-converters/0183792/, Date Accessed: 08/01/2018.

[7] RS Components Ltd., "Murata Power Solutions Through Hole 60W Isolated DC-DC Converter," https://uk.rs-online.com/web/p/isolated-dc-dc-converters/7256415/, Date Accessed: 08/01/2018.

[8] ZOTAC, "ZBOX-PI320-W2," https://www.zotac.com/gb/product/mini_pcs/pi320, Date Accessed: 08/01/2018.

[9] Davis, N., Francis, D., Black, P., Livingstone, B., Staines, S., Hodgkinson, J. and Tatam, R. P. (2017), "New sample cell technologies for mid infra red methane detection," *Proceedings of Industrial Methane Measurement Conference, Antwerp, 29-30 November 2017.*

Chapter 7

Conclusions and Future Work

7.1 Thesis summary and conclusions

The development of instrumentation to acquire measurements of the background atmospheric methane concentration level was presented in this thesis.

An investigation was carried out into the suitability of utilising a new external cavity Bragg-stabilised laser for use in methane detection, with comparisons made between this laser and a fibre-coupled DFB laser, both operating at 1651nm. It was found that, although the ECBSL had a single-point limit of detection for methane similar to that of the DFB laser (both at approximately 8.3ppm), there are a number of drawbacks that limit its potential use. Alignment stability of the laser prevented reliable measurements below a methane concentration level of 100ppm being taken, whilst its tuning range was significantly smaller than that of the DFB. It was concluded that, although the laser showed promise for future use in gas detection, it would not be possible to utilise this laser for the purpose of detecting methane outside the laboratory (especially in a light aircraft) in its current configuration.

Experiments into detecting methane were then carried out using an interband cascade laser in the mid-infrared, centred around an absorption line at 3313nm. A characterisation of the laser and detector were performed, finding that at a modulation frequency of 1kHz was required to reduce a distortion in the detected signal present. Measurements of methane were made using an integrating sphere with

effective pathlength 54.5cm and with a 25cm pathlength single-pass cell. Single-point limit of detections of 2.2ppm and 1.0ppm were measured for the single-pass cell and integrating sphere respectively.

Improvements to the limit of detection were sought through the use of an Allan deviation plot and line-fitting techniques. An optimum averaging time of 25 seconds was found using the Allan deviation, with a line-fit for this period producing a limit of detection of 0.3ppm using the integrating sphere. It was thought that the performance of the integrating sphere is ultimately limited by the reflectivity of the infragold coating, which itself is limited to between 94 and 95% in the mid-infrared.

Chapter 6 details the design and development of the instrumentation produced to detect atmospheric methane on light aircraft. The reasoning behind the selection of the individual components in the instrument was explained, followed by a demonstration of the evolution of the instrument design through the use of 3D block diagrams. The instrument was then assembled following the final design that was produced using 3D printed mounting devices to secure the components to the aluminium base.

Laboratory tests of the instrument found that the noise levels were slightly higher than those seen in the experimental work previously undertaken, as detailed in chapter 5. A single-point limit of detection of 1.6ppm was determined for the instrument, an increase seemingly matching the increased noise levels measured at the detector compared with the previous experimental set-up. The peaks of the detected absorption feature also less well-defined than those observed previously in the laboratory. It was thought that this could be attributed to the higher operating temperature of the detector required in the instrument (-15°C versus -20°C), coupled with the different amplifiers used and the close proximity to other components. The observed peaks, however, were sufficiently distinguishable that reliable measurements could be made.

The aircraft was then modified, with both it and the instrument certified for for flight testing. Several modifications to the aircraft were required, including the installation of an inlet plate and flexible tubing, and cut-outs made on the mounting box for the tubing. The process of certifying the instrument took 20 months to complete between December 2015 and August 2017, limiting the time available for flight testing to take place.

A flight campaign to test the instrument was planned, with a shakedown flight along with two measurement flights scheduled. During the shakedown flight, damage was incurred to two of the components within the instrument. The damage to one component was easily rectified, whilst it is as yet unclear where the issue with the second component resides. It was thought that this problem was likely the result of physical damage caused to the component by vibrations within the instrument. Further work to isolate the instrument was therefore required before any further testing could take place. The flight campaign was therefore postponed until the modifications to the instrument have been made.

7.2   Future Research

The output of the research and work carried out during this thesis indicated a number of areas that could gain from further study. In this section, an outline of the potential areas of future research that builds on the work carried out in this thesis is presented.

Following the issues had with the shakedown flight, adding vibration isolation to the instrument to assist in preventing additional damage would be the first major improvement required going forward. This would also have a potential secondary effect of reducing the background (acoustic) noise level whilst flying. A number of anti-vibration mounts are available that could replace the mounting posts on the adaptor plate. This would ensure that the entire instrument, not just the individual components are isolated from the aircraft.

Several non-essential improvements could also be made to the instrument to potentially improve the limit of detection. Larger heatsinks could be introduced to the detectors, reducing the temperature to which the detectors can be cooled. This will reduce the noise equivalent absorbance of the detectors, thus lowering the limit of detection. Replacing the amplifiers with alternatives that have a lower specified noise equivalent power may also have a positive impact in the same manner. Improvements to the cooling of the device could also be explored. This could be achieved by: introducing a number of small fans within the instrument to increase circulation, upgrading the pump to one with a higher flow rate and directing the air flow over the components, and adding air holes to the 3D printed mounts.

Investigations could be made into utilising alternative gas cells to replace the integrating sphere within the instrument. Custom integrating cavities could be investigated, determining a size and form that would more optimally fit within the confines of the instrument. Due to the inherently rough surface that is produced when 3D-printing objects, an integrating cavity could be designed that utilises this fact. With the rough surface needed for diffuse reflections to occur potentially already being present, the surface would only need to be coated (e.g. in gold) for it to be utilised.

Alternative coatings for the cavities could also be investigated, for example copper or aluminium as investigated by Bane *et al* [1], in an effort to find one that would provide a higher reflectance in the mid-infrared and therefore a longer effective pathlength. Another gas cell to investigate could be one made from hollow core waveguides, as discussed in chapter 2, section 2.6.5. These cells have shown the ability in laboratory conditions to detect methane down to sub-ppm levels [2] with a fast response time (0.8 seconds) and a pathlength of 5 metres. This low volume, long pathlength gas cell could potentially be an ideal replacement for the integrating sphere.

Another avenue could be to design and develop custom electronics to replace some or all of the components in the instrument. Several of the components currently utilised, such as the laser controller, take up a significant proportion of the internal volume whilst having functionality that is not required. Custom electronics would potentially be smaller and more power efficient compared with their off-the-shelf equivalents, however the process of getting these components certified for use in-flight would require additional time and money.

As discussed in Chapter 6, section 6.5.3, a flight plan was established to test the instrument. This included: performing an Allan deviation by sealing the integrating sphere with a known methane concentration inside; flushing the sphere out with air so an attempt at detecting background methane concentrations could be made; performing ground tests of the noise levels of the instrument whilst running off the aircraft power supply. As these tests were unable to be completed due to the damage sustained, undertaking this flight plan would be an obvious choice for any future work undertaken with the instrument.

Finally, investigations into alternative wavelengths and target gas species could be performed. Currently, the instrument is set up to only take measurements of methane, however there are a number of alternative gas species that have strong absorption lines in the mid-infrared that could be targeted. This is potentially a relatively simple change, as all that would need to be done is to replace the current laser with one of the same model that operates at an alternative wavelength. A second ICL has already been purchased with this intent. This ICL has a typical wavelength of 3335nm which will allow it to measure both an ethane absorption line and weaker methane absorption line simultaneously. A plot of these lines can be seen in Figure 7.1.
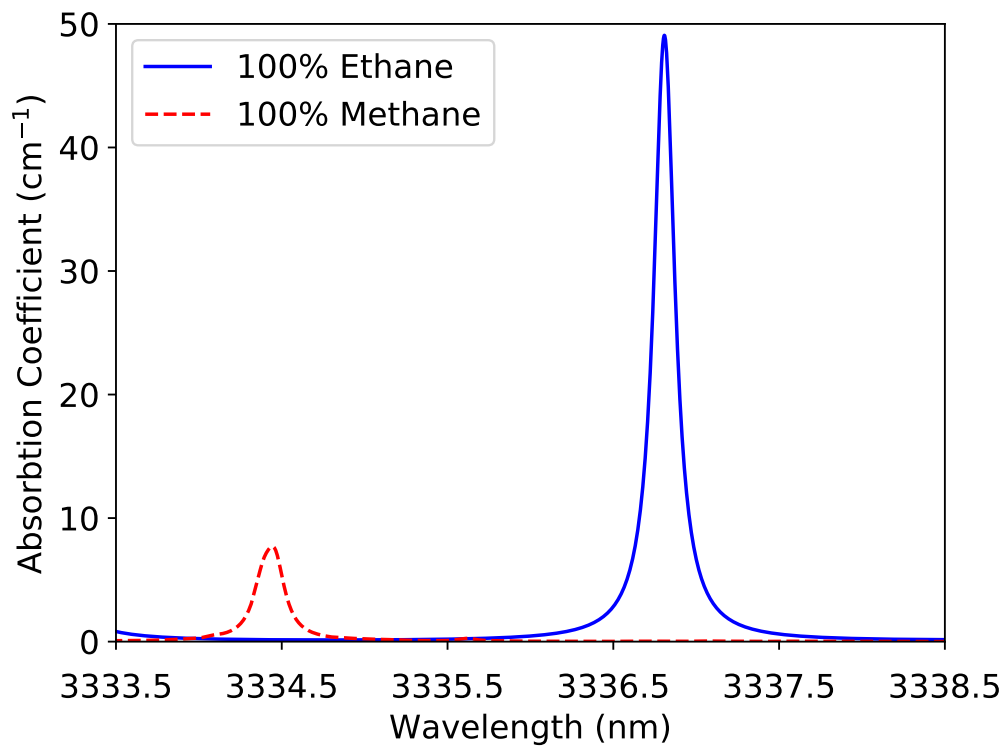
Figure 7.1: *Comparison between absorption lines for ethane and methane, centred around 3335nm (taken from HITRAN database [3]).*

References

[1] Bane, K. L. F., Stupakov, G. and Tu, J. J. (2006), "Reflectivity Measurements for Copper and Aluminum in the Far Infrared and the Resistive Wall Impedance in the LCLS Undulator," in: "Proceedings of the European Particle Accelerator Conference," pp. 2955–2957.

[2] Francis, D., Hodgkinson, J., Livingstone, B., Black, P. and Tatam, R. P. (2016), "Low-volume, fast response-time hollow silica waveguide gas cells for mid-IR spectroscopy," *Applied Optics*, vol. 55, no. 25, pp. 6797–6806.

[3] Rothman, L., Gordon, I., Babikov, Y., Barbe, A., Chris Benner, D., Bernath, P., Birk, M., Bizzocchi, L., Boudon, V., Brown, L., Campargue, A., Chance, K., Cohen, E., Coudert, L., Devi, V., Drouin, B., Fayt, A., Flaud, J.-M., Gamache, R., Harrison, J., Hartmann, J.-M., Hill, C., Hodges, J., Jacquemart, D., Jolly, A., Lamouroux, J., Le Roy, R., Li, G., Long, D., Lyulin, O., Mackie, C., Massie, S., Mikhailenko, S., Müller, H., Naumenko, O., Nikitin, A., Orphal, J., Perevalov, V., Perrin, A., Polovtseva, E., Richard, C., Smith, M., Starikova, E., Sung, K., Tashkun, S., Tennyson, J., Toon, G., Tyuterev, V. and Wagner, G. (2013), "The HITRAN2012 molecular spectroscopic database," *Journal of Quantitative Spectroscopy and Radiative Transfer*, vol. 130, pp. 4–50.

List of Publications

The following publications and outcomes have resulted from the work presented in this thesis:

Conference Papers

- Davis, N. M., Hodgkinson, J., Francis, D., Tatam, R. P. (2016), "Sensitive detection of methane at 3.3μm using an integrating sphere and interband cascade laser," *Proceedings of SPIE - Optical Sensing and Detection IV*, vol. 9899, pp. 98990M.

- Davis, N. M., Francis, D., Black, P., Livingstone, B., Staines, S., Hodgkinson, J., Tatam, R. P. (2017), "New sample cell technologies for mid infra red methane detection," *Proceedings of Industrial Methane Measurement Conference, Antwerp, 29-30 November 2017.*

Further conference participation

- Davis, N. M., Hodgkinson, J., Tatam, R. P., "Detection of atmospheric methane using an Interband Cascade Laser," Poster presentation at Analytical Research Forum 2015, London, 3 July 2015.

- Davis, N. M., Hodgkinson, J., Tatam, R. P., "Detection of atmospheric methane using an Interband Cascade Laser," Poster presentation at GASG 64th Colloquium, Cranfield University, 21 April 2016 (received best poster presentation prize).

- Davis, N. M., Hodgkinson, J., Francis, D., Tatam, R. P., "Detection of methane at 3.3μm using an integrating sphere and Interband Cascade Laser for

environmental applications," Poster presentation at FLAIR 2016, Aix-les-Bains, 12-16 September 2016.

- Davis, N. M., Lynch S. G., Gates J. C., Hodgkinson, J., Smith, P. G. R., Tatam, R. P., "Methane detection using an external cavity Bragg grating stabilised laser at 1651nm," Poster presentation at FLAIR 2016, Aix-les-Bains, 12-16 September 2016.

Planned journal papers

- Davis, N. M., Hodgkinson, J., Francis, D., Tatam, R. P., Working title: "Development and laboratory testing of robust instrumentation to detect atmospheric methane."

- Davis, N. M., Hodgkinson, J., Francis, D., Tatam, R. P., Working title: "Robust instrumentation to perform in-flight measurements of atmospheric methane."

- Davis, N. M., Francis, D., Hodgkinson, J., Tatam, R. P., Working title: "Analysis of line fitting parameters for 3313nm methane absorption line."

- Davis, N. M., Lynch S. G., Gates J. C., Hodgkinson, J., Smith, P. G. R., Tatam, R. P., Working title: "Methane detection using an external cavity Bragg grating stabilised laser at 1651nm."

- Davis, N. M., Francis, D., Hodgkinson, J., Tatam, R. P., Working title: "Comparison of available gas cells for methane detection in the mid-infrared."
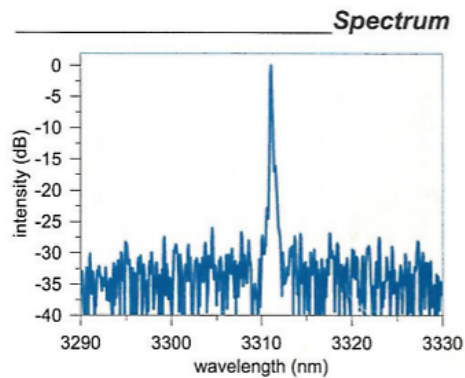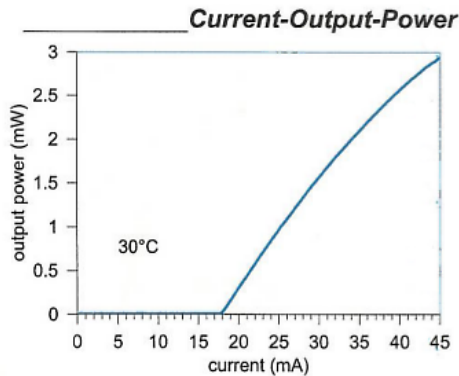
Appendix A

ICL datasheets

S/N: 1418/19-31

Nanosystems and
Technologies
GmbH

nanoplus

Datasheet for 3311nm DFB Laser

Current-Output-Power

Spectrum

The laser is mounted on: TO66 with TEC and cap. Electrical connection as shown:

Bottom View

Pin	Function
1	Peltier (+)
2	Thermistor
3	Thermistor
4	N/C
5	N/C
6	N/C
7	LD (+)
8	LD (-)
9	Peltier (-)

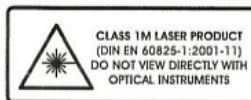| Parameter	Symbol	Value	Unit
Max. temperature diff.	ΔT_{max}	67	K
Max. current	I_{max}	1.4	A
Max. voltage	U_{max}	3.8	V
Max. power	Q_{max}	3.0	W
Thermistor R_0 @ 25°C	R_0	10000	Ω
Thermistor b	b	3930	
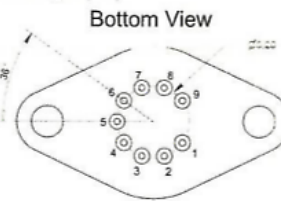
Caution: Before operating the cooler: TO66 has to be connected to a heat sink. **Characteristics**

Parameter	Symbol	Unit	min	typical	max
Operation voltage	U	V			6.0
Max. Current	I_{max}	mA			45
Threshold current	I_{th}	mA		18	
Slope efficiency	e	mW/mA		0.17	

Operation conditions

Parameter	Symbol	Unit	min	typical	max
Operation temperature	T	°C	25	30	35
Wavelength	λ	nm		3311.3	
Operation current	I	mA		37	45
Output power	P_{opt}	mW		2.3	

Device protected by US patent no. 6,671,306; 6,846,689

S/N: 1418/19-31

Nanosystems and
Technologies
GmbH

nanoplus

Package option: TO66 with collimating lens

_____handling instructions

Nanoplus cube with X-Y collimator

↕

Polarization direction of
electric field (transverse electric - TE)

Do not touch the screws! Turning or touching
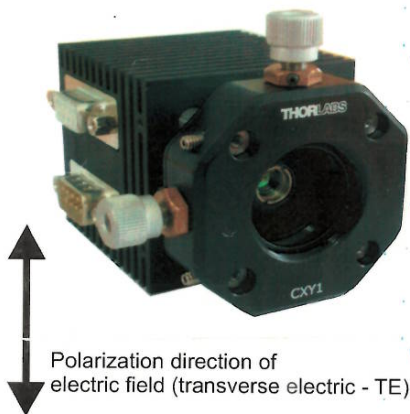of the screws will harm the beam collimation.

Apply protective cap when laser is not in use
to avoid dust deposition on lens.

Note: The collimation may reduce the laser output power by up to 20%.

_____beam profile

Thermal image of the collimated laser beam
at 3.0 m distance from the laser facet.

6.4 mm
5.3 mm
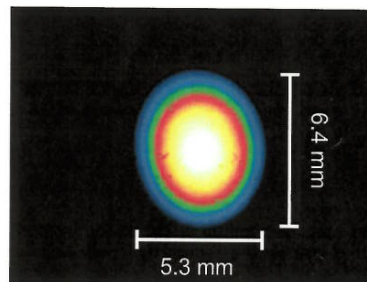
Laser temperature: 30°C
Laser current: 37 mA

CLASS 3B LASER PRODUCT
(DIN EN 60825-1:2001-11)
AVOID EXPOSURE TO BEAM

Caution:
High voltage, high temperature, and mechanical forces may cause
irreversible damage to the laser. When handling the laser diode
proper ESD (electrostatic discharge) precautions are recommended
to avoid performance degradation or loss of functionality.
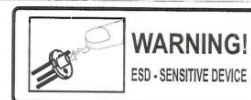
WARNING!
ESD - SENSITIVE DEVICE

Appendix B

Labview data acquisition code

C:\DATA_inst

Name of Instrument
instrument_

Location
cranfield-university

_%Y%m%d%H%M%S

\

.csv

Path

Conventions,G,BADC-CSV,1

title,G,My Data File

creator,G,N Davis,Cranfield University

long_name,time,time

long_name,cell,reading from cell detector

long_name,reference,reading from reference detector

long_name,modulation,laser modulation value

coordinate_variable,1,X

location_name,G,Cranfield University

metadata

data

Appendix C

3D printed mounting designs
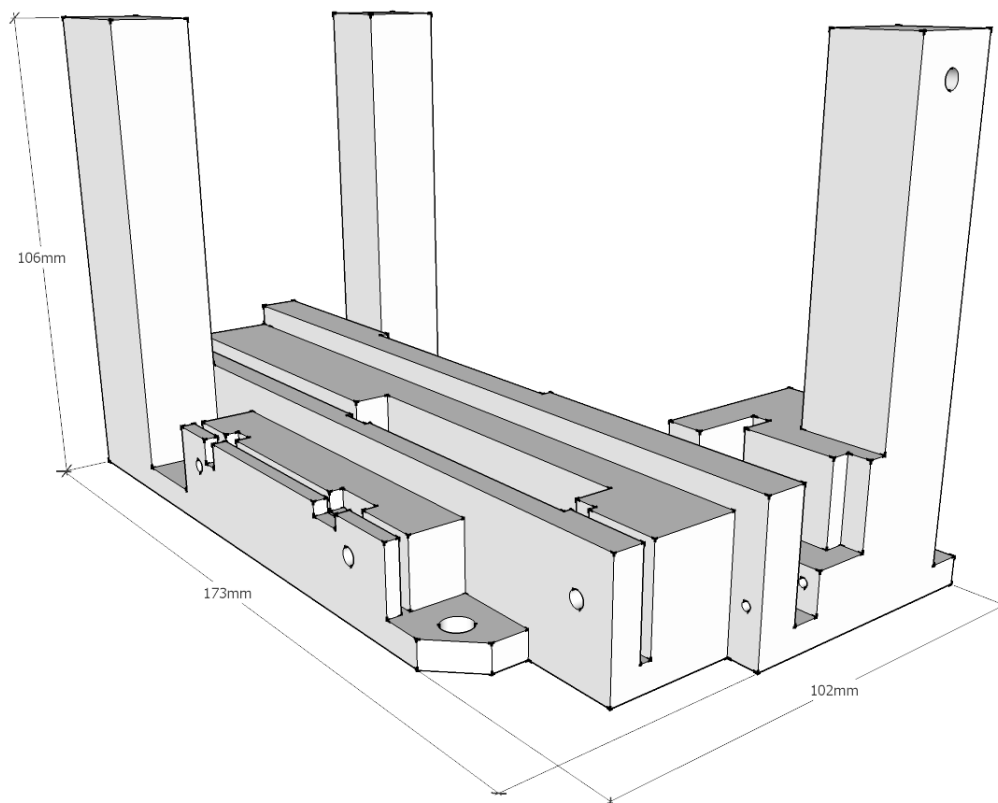
Figure C.1: *Mount for laser controller, ADC board and 12V voltage regulators.*
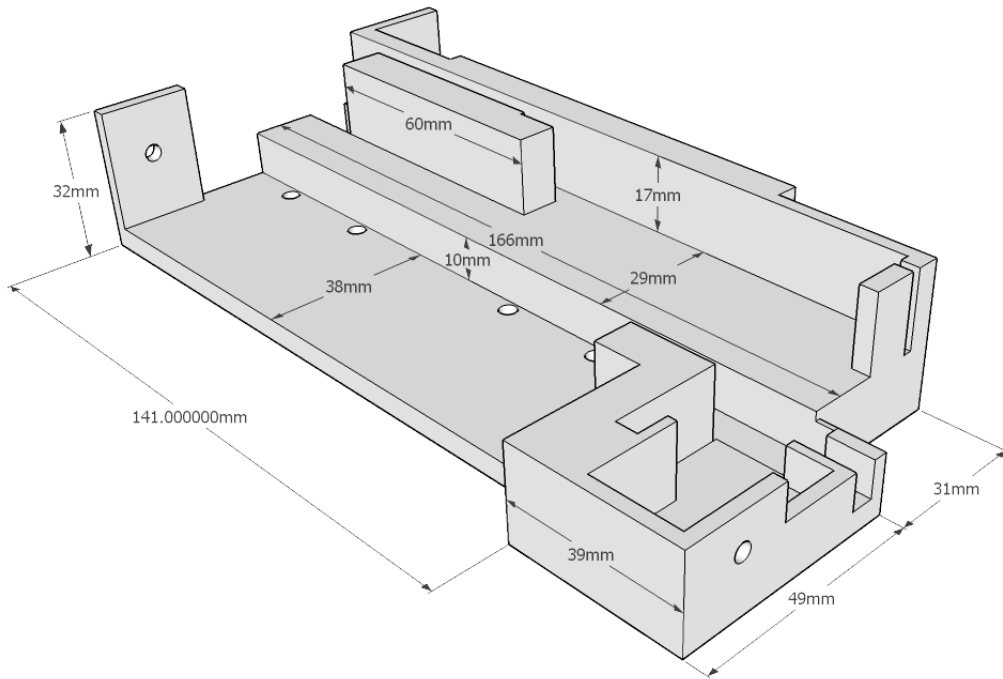
Figure C.2: *"Lid" mount for laser controller, ADC board and 12V voltage regulators.*
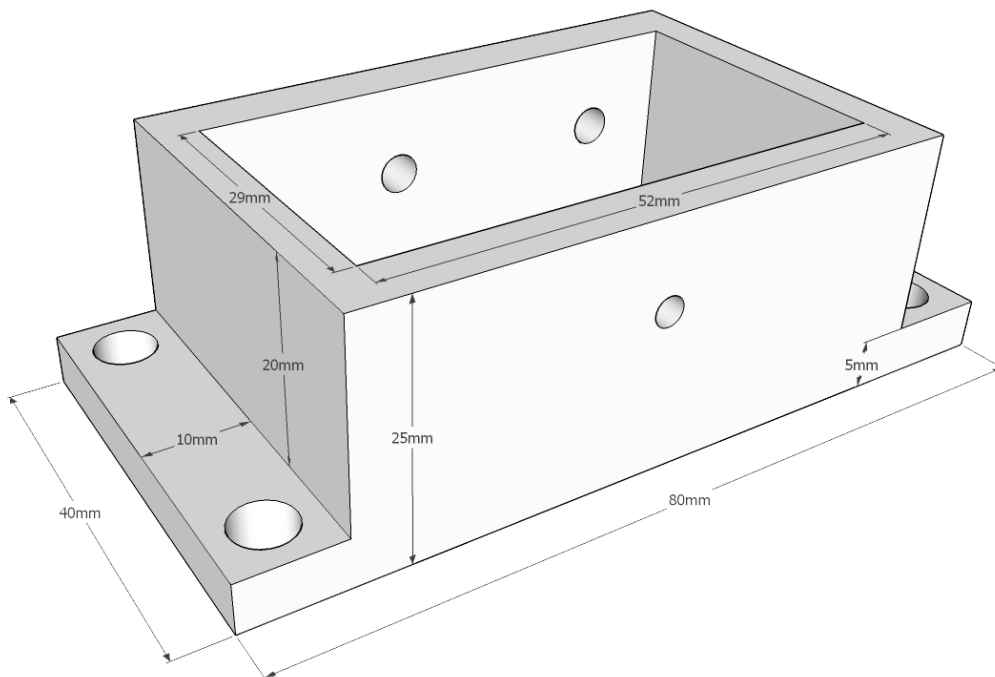
Figure C.3: *Mount for 5V voltage regulator.*

151
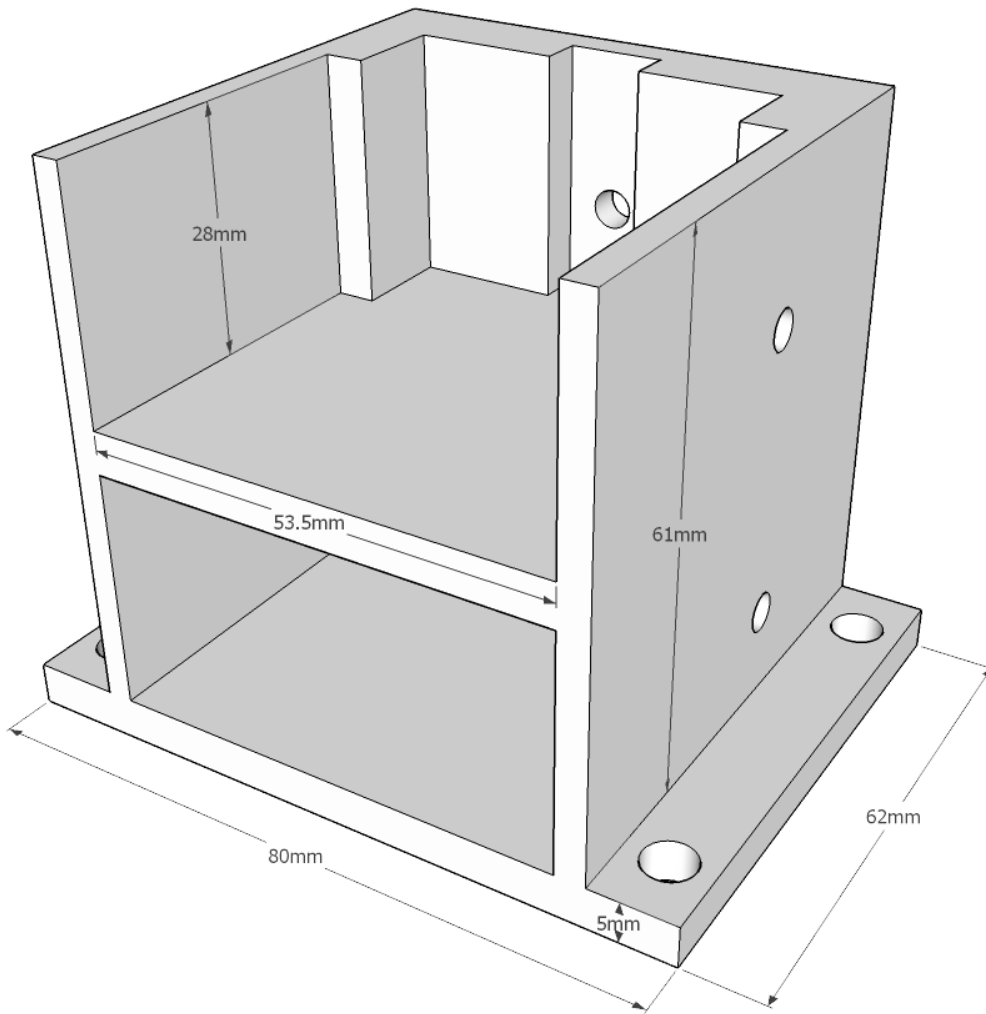
Figure C.4: *Mount for detector amplifiers.*
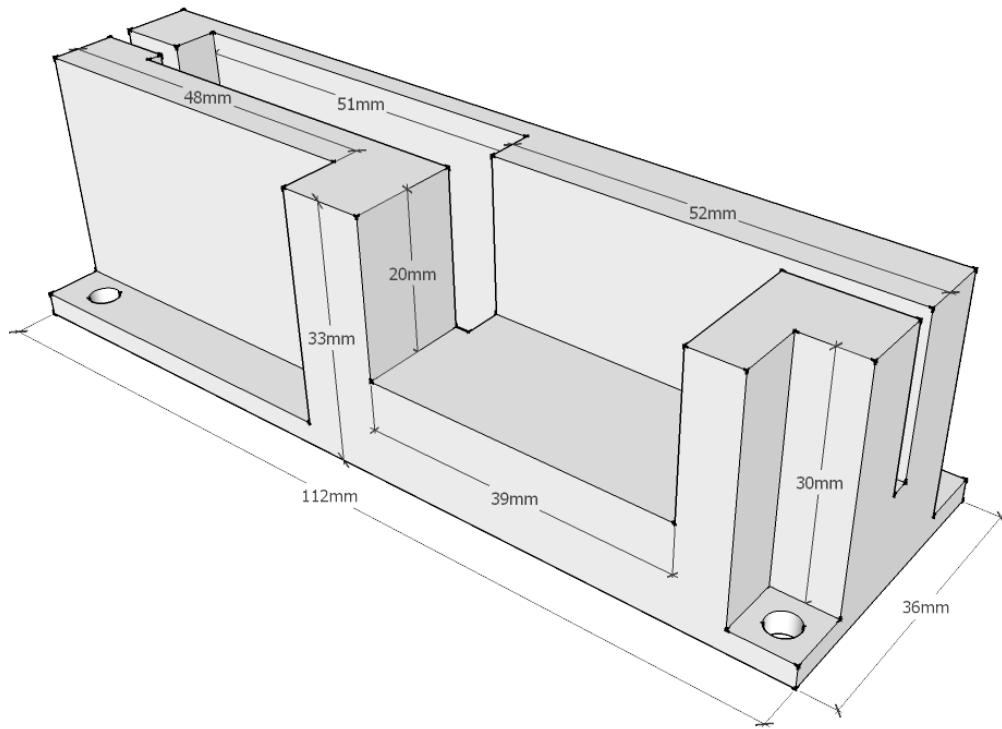
Figure C.5: *Mount for detector thermal controller.*
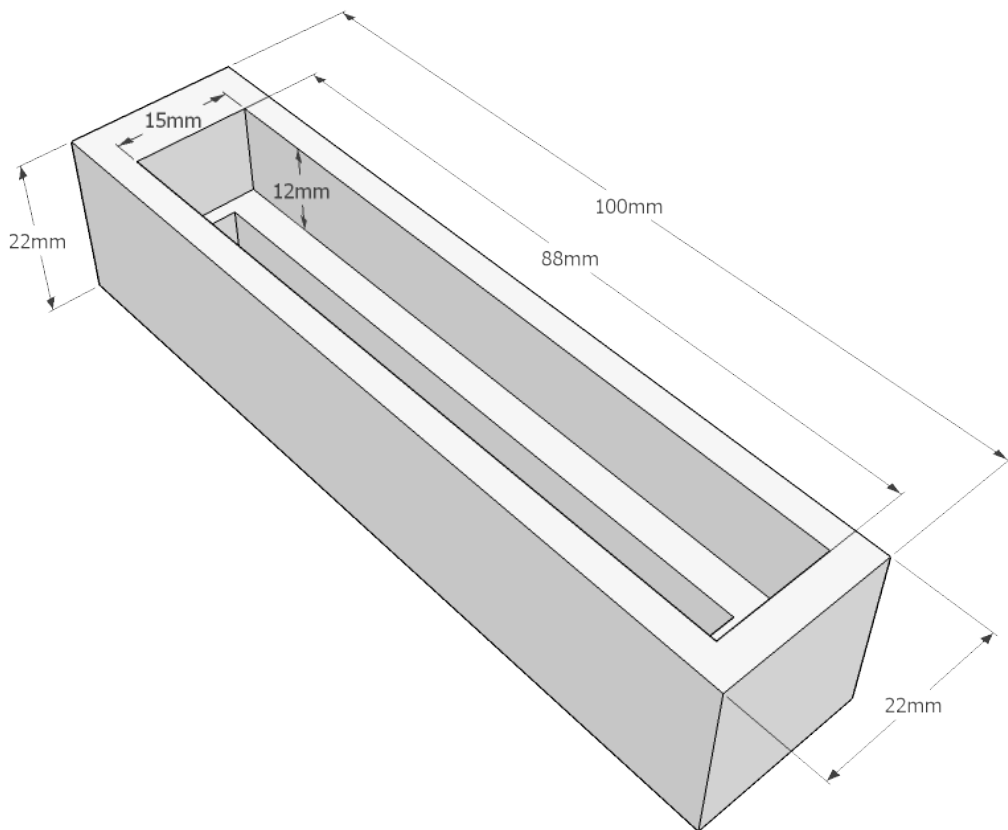
Figure C.6: *Bar to support and position Laser.*
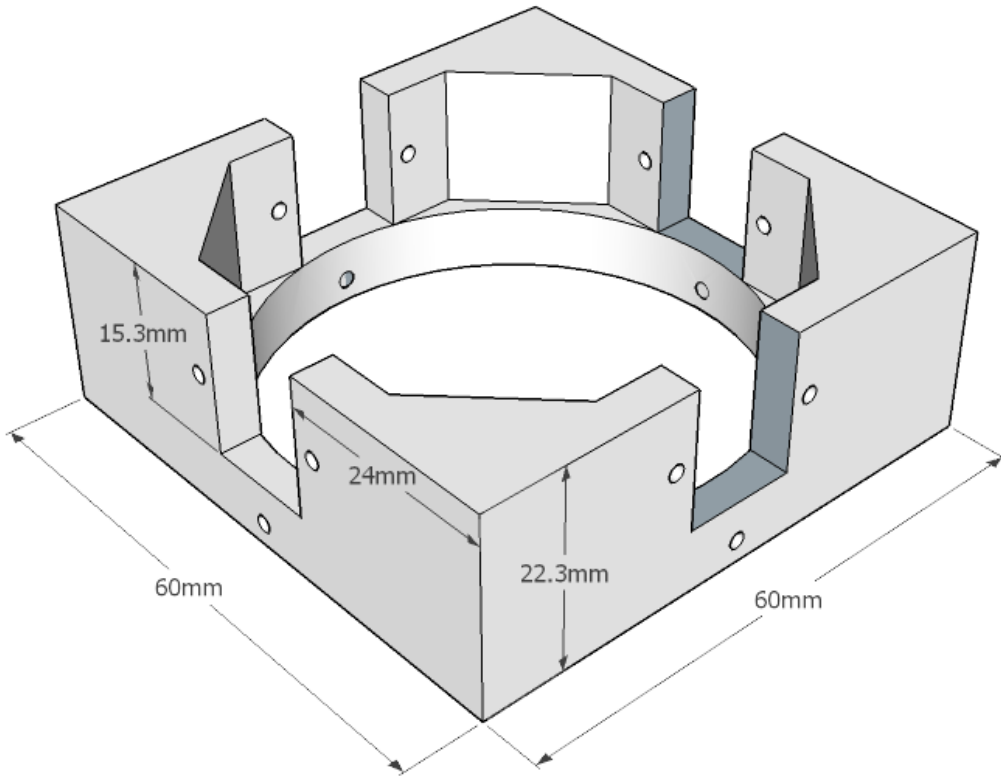
Figure C.7: *Adaptor to attach laser to the integrating sphere.*
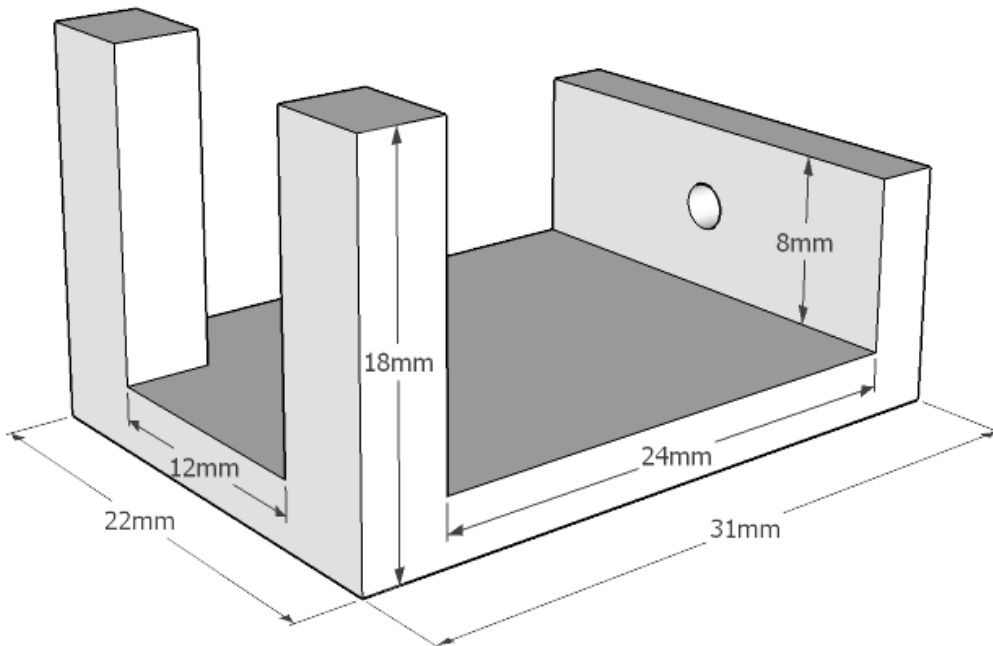
Figure C.8: *Mount for PC power button*

154
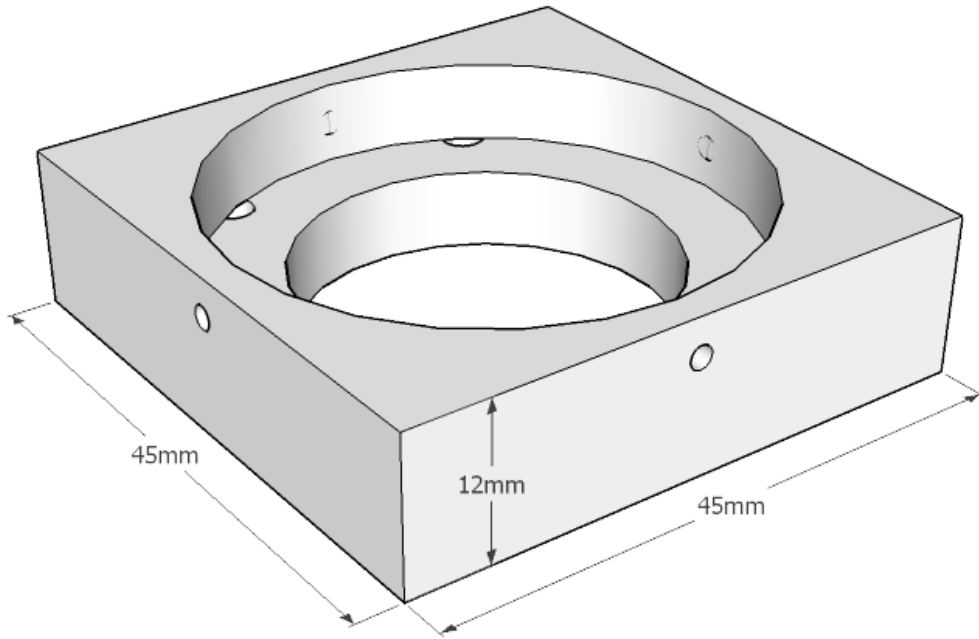
Figure C.9: *Adaptor to attach detectors to integrating sphere.*

Appendix D

Aeroplane modification and certification documents

SUPPLEMENT MANUAL AAL.TEC-0003
Bulldog Series 120 Model 122

INTRODUCTION OF A STAND ALONE ATMOSPHERIC SENSING DEVICE

Airworthiness Assured Limited Design Change
Reference Number AAL.25-116-0003

Issue 1									
Document Compiled By:		M. Hubbard		**Date:**		21/08/17			
CVE Name:		**Signature:**		**Category(s)**					
				A = Document Check		B = Document Approval		C = Compliance Verification	
A. Pimblott				A	3,5	B	3,5	C	3,5
P. Gaughan				A	1,2	B	1,2	C	1,2
Categories Key									
1 Avionic Systems	2 Electrical Systems	3 Hydro/Mechanical Systems	4 Interiors	5 Structures	6 Performance / Handling	7 Aerodynamics	8 Environmental		

The technical content of this document is approved under the authority of CAA Approval No. DAI/9952/12					
Head of Design	Name:	J. Dent	Signature:		Date: 21/08/17

Revisions to this manual will be made as a complete new issue and recorded in the record of re-issues. Revisions or amendments by other approved organisations must be separately certified and recorded on separate record sheets.

SECTION VIEW ON ARROW A-A SHOWING

-1 GENERAL ARRANGEMENT FOR INTRODUCTION OF STAND ALONE
ATMOSPHERIC SENSING DEVICE

NOTES;

1. REFER TO BORDER FOR GENERAL NOTES
2. LOCALLY ROUTE WIRE HARNESS FROM THE ATMOSPHERIC SENSING DEVICE TO THE PLUG
   LOCATED ON THE INSTRUMENTATION BOX. IT IS ACCEPTABLE TO TY-WRAP THE WIRE
   HARNESS TO THE TUBING FROM THE ATMOSPHERIC SENSING DEVICE.
3. FONT TO BE ARIAL AND FONT SIZE TO BE 0.1 INCHES HIGH, WHITE TEXT ON BLACK
   BACKGROUND

SCALE N.T.S   DO NOT SCALE DRAWING   IF IN DOUBT ASK

NOTES;

1. REFER TO BORDER FOR GENERAL NOTES

2. DRILL HOLE THRU EXISTING DOUBLER P/N: 31-116-10072-1 TO SUIT ITEM 13.
   RE PART MARK RE WORKED DOUBLER TO P/N: 25-116-10002-2.

3. ROUTE AND SECURE TUBING ITEM 26 FROM ITEM 14 TO ITEM 15 ALONG THE
   PORT SIDE WALL PANEL WITH TY-WRAPS.

4. INSTALL ITEM 26 TO THE 90° TUBE UNION THAT IS PART OF ITEM I5.

5. DRILL VENTILATION HOLES IN EXISTING INSTRUMENTATION BOX LID P/N:
   31-116-10061-20 SAME AS EXISTING PATTERN IN EXISTING POWER SUPPLY BOX
   LID.

6. CUTOUT EXISTING INSTRUMENTATION BOX LID P/N: 31-116-10061-20, ENSURE
   THERE IS SUFFICIENT CLEARANCE WITH UNION PROTRUDING FROM ITEM 15. RE
   PART MARK RE WORKED INSTRUMENTATION BOX LID TO P/N: 25-116-10002-3.

7. DRILL THRU FROM ITEM 17 TO EXISTING INSTRUMENTATION BOX LID

8. INSTALL ITEM 17 TO EXISTING INSTRUMENTATION BOX LID USING ITEMS 27, 28
   AND 29.

9. ALODINE AND EPOXY PRIME ALL BARE METAL — FINISH BLUE TO MATCH AIRCRAFT
   LIVERY.

-1 STAND ALONE ATMOSPHERIC SENSING DEVICE INSTALLATION

DETAIL B

DETAIL C

FRA 54.55

FRA 64.00

SCALE N.T.S   DO NOT SCALE DRAWING   IF IN DOUBT ASK

DESCRIPTION
STAND ALONE ATMOSPHERIC
SENSING DEVICE INSTALLATION

DRAWING NUMBER
25-116-10002

SHEET   OF   SHEETS
19   4   20

AIRWORTHINESS ASSURED LIMITED,
THE WALDORF CENTRE, 120 LONDON ROAD,
ALVASTON, DERBY, DE24 8QP, ENGLAND

ISSUE | DESCRIPTION | DATE | DRAWN | CHECK | STRESS | APP.
A | FIRST ISSUE | AUG 2017 | M.H. | J.D. | | J.D.

ISSUE / ALTERATIONS

NOTES;

1. REFER TO BORDER FOR GENERAL NOTES.
2. DEGREASE AND TREAT USING ALODINE 1200 AND PR143 EPOXY PRIMER.
3. FINISH – TO SUIT AIRCRAFT INTERIOR

−1 MOUNTING PLATE

Ø0.12 [Ø3.05] THRU, 4 POS.

Ø0.20 [Ø5.08] THRU, 4 POS.

R0.20 [R5.08] TYP

11.50 [292.10]
11.15 [283.21]
8.20 [208.28]
6.05
1.20

0.75 [19.05]
0.45 [11.43]
1.00 [25.40]
1.20 [30.48]
2.00
3.00
5.40 [137.16]
6.35 [161.29]
7.00 [177.80]

SCALE N.T.S
DO NOT SCALE DRAWING   IF IN DOUBT ASK

GENERAL NOTES :-
DIMENSIONS IN INCHES
ALL ITEMS TO BE PART MARKED USING INDELIBLE INK
AT EACH LOCATION MARKED
REMOVE BURRS AND BREAK SHARP CORNERS AS FOLLOWS
0.004" TO 0.02" UNLESS OTHERWISE STATED
DRAWING INTERPRETATION TO BS 8888

GENERAL TOLERANCES U.O.S.
MACHINED PARTS   ±0.01
SHEET METAL PARTS
FLAT   ±0.01
FORMED   ±0.02
COMPOSITE MATERIAL PARTS
FORMED   ±0.01
FLAT   ±0.02
ANGLES TOLERANCE   ±2°

THIS DRAWING IS APPROVED AS PART OF A AIRWORTHINESS
ASSURED LIMITED DESIGN CHANGE(S) AND EFFECTIVE FOR
AIRCRAFT STATED ON APPLICABLE STATEMENTS OF
APPROVED DESIGN

© THE COPYRIGHT OF THIS DRAWING IS RESERVED BY
AIRWORTHINESS ASSURED LIMITED. IT IS ISSUED ON THE
CONDITION THAT IT IS NOT COPIED, REPRODUCED, OR DISCLOSED
TO A THIRD PARTY EITHER WHOLLY OR IN PART WITHOUT THE
CONSENT IN WRITING OF AIRWORTHINESS ASSURED LIMITED.

AIRWORTHINESS ASSURED LIMITED,
THE WALDORF CENTRE, 1200 LONDON ROAD,
ALVASTON, DERBY, DE24 8QP, ENGLAND

DESCRIPTION
MANUFACTURE – STAND ALONE
ATMOSPHERIC SENSING DEVICE
PART DETAILS

DRAWING NUMBER
25-116-10004

SHEET 3 OF 20 SHEETS

ISSUE/ALTERATIONS

ISSUE	DESCRIPTION	DATE	DRAWN	CHECK	STRESS	APP.
A	FIRST ISSUE	AUG 2017	M.H.	J.D.		J.D.

R0.25 TYP

HOLE Ø0.17 4 POS

R0.15 TYP

1.75
2.25
0.25
1.25
1.75
0.25

1.00
0.63
0.63

—2 TOP HAT SECTION

REFER TO SHEET ONE FOR NOTES

SCALE N.T.S.

DO NOT SCALE DRAWING   IF IN DOUBT ASK